

Towards cavity quantum electrodynamics and coherent control with single InGaN/GaN quantum dots



Benjamin P. L. Reid
Wadham College
Department of Condensed Matter Physics

*Thesis submitted for the degree of
Doctor of Philosophy*

Trinity Term 2013

**Towards cavity quantum electrodynamics and coherent control with single
InGaN quantum dots**

Benjamin P. L. Reid

Wadham College

Thesis submitted for the degree of Doctor of Philosophy

Trinity Term 2013 **Abstract**

Experimental investigations of the optical properties of InGaN/GaN quantum dots are presented. A pulsed laser is used to perform time-integrated and time-resolved microphotoluminescence, photoluminescence excitation, and polarisation-resolved spectroscopy of single InGaN quantum dots under a non-linear excitation regime.

The first micro-photoluminescence results from InGaN/GaN quantum dots grown on a non-polar crystal plane ($11\bar{2}0$) are presented. Time-resolved studies reveal an order of magnitude increase in the oscillator strength of the exciton transition when compared to InGaN quantum dots grown on the polar (0001) plane, suggesting a significantly reduced internal electric field in non-polar InGaN quantum dots.

Polarisation resolved spectroscopy of non-polar InGaN quantum dots reveals 100% linearly polarised emission for many quantum dots. For quantum dot emissions with a polarisation degree less than unity, a fine structure splitting between two orthogonal polarisation axes can be resolved in an optical setup with a simple top-down excitation geometry.

A statistical investigation into the origins of spectral diffusion in polar InGaN quantum dots is presented, and spectral diffusion is attributed to charge carriers trapped at threading dislocations, and itinerant and trapped carriers in the underlying quantum well layer which forms during the growth procedure. Incorporating quantum dots into the intrinsic region of a p-i-n diode structure and applying a reverse bias is suggested as a method to reduce spectral diffusion.

Coherent control of the excited state exciton in a non-polar InGaN quantum dot is experimentally demonstrated by observation of Rabi rotation between the excited state exciton and the crystal ground state. The exciton ground state photoluminescence is used as an indirect measurement of the excited state population.

Publications

- *Origins of spectral diffusion in the micro-photoluminescence of single InGaN quantum dots*
B.P.L. Reid, T. Zhu, T.J. Puchtler, L.J. Fletcher, C.C.S. Chan, R.A. Oliver, and R.A. Taylor, Japanese Journal of Applied Physics **52**, 08JE01 (2013).
- *Confocal microphotoluminescence mapping of coupled and detuned states in photonic molecules*
F.S.F. Brossard, B.P.L. Reid, C.C.S. Chan, X.L. Xu, J.P. Griffiths, D.A. Williams, R. Murray, and R.A. Taylor, Optics Express **21**, 16934 (2013).
- *Optical studies of the surface effects from the luminescence of single GaN/InGaN nanorod LEDs fabricated on a wafer scale*
C.C.S. Chan, B.P.L. Reid, R.A. Taylor, Y. Zhuang, P.A. Shields, D.W.E. Allsopp, W. Jia, Applied Physics Letters **102**, 111906 (2013).
- *Non-polar (11-20) InGaN quantum dots with short exciton lifetimes grown by metal-organic vapor phase epitaxy*
T. Zhu, F. Oehler, B.P.L. Reid, R.M. Emery, R.A. Taylor, M.J. Kappers, and R.A. Oliver, Applied Physics Letters **102**, 251905 (2013).
- *Photoluminescence of Single GaN/InGaN Nanorod Light Emitting Diode Fabricated on a Wafer Scale*
C.C.S. Chan, Y. Zhuang, B.P.L. Reid, W. Jia, M.J. Holmes, J.A. Alexander-Webber, S. Nakazawa, P.A. Shields, D.W.E. Allsopp, and R.A. Taylor, Japanese Journal of Applied Physics **52**, 08JE20 (2013).
- *Growth and optical characterisation of multilayers of InGaN quantum dots*
T. Zhu, H.A.R. El-Ella, B. Reid, M.J. Holmes, R.A. Taylor, M.J. Kappers, and R.A. Oliver, Journal of Crystal Growth **338**, 262 (2012).
- *Design and fabrication of optical filters with very large stopband (~ 500 nm) and small passband (1 nm) in silicon-on-insulator*

W. Jia, J. Deng, B.P.L. Reid, X. Wang, C.C.S. Chan, H. Wua, X. Li, R.A. Taylor, and A.J. Danner, *Photonics and Nanostructures - Fundamentals and Applications* **10**, 447 (2012).

- *Optical studies of GaN nanocolumns containing InGaN quantum disks and the effect of strain relaxation on the carrier distribution*

M.J. Holmes, Y.S. Park, X. Wang, C.C.S. Chan, B.P.L. Reid, H.D. Kim, J. Luo, J.H. Warner, and R.A. Taylor, *Physica Status Solidi (c)* **9**, 712 (2012).

- *Optical studies of Quantum Dot-like Emission from Localisation Centres in InGaN/GaN Nanorod Array LEDs*

C.C.S. Chan, P.A. Shields, M.J. Holmes, Y. Zhuang, B.P.L. Reid, H.D. Kim, D.W.E Allsop, and R.A. Taylor, *Physica Status Solidi (c)* **9**, 635 (2012).

- *Optical studies on a single GaN nanocolumn containing a single $In_xGa_{1-x}N$ quantum disk*

M.J. Holmes, Y.S. Park, X. Wang, C.C.S. Chan, B.P.L. Reid, H.D. Kim, R.A. Taylor, J.H. Warner and J. Luo, *Applied Physics Letters* **98**, 251908 (2011).

- *Growth of InGaN Quantum Dots with AlGaN barrier layers via modified droplet epitaxy*

R.A. Oliver, H.A.R. El-Ella, D.P. Collins, B. Reid, Y. Zhuang, F. Christie, M.J. Kappers, and R.A. Taylor, submitted to *Journal of Applied Physics* (2013).

- *High temperature stability in non-polar InGaN quantum dots: Exciton and biexciton dynamics*

B.P.L. Reid, T. Zhu, F. Oehler, C.C.S. Chan, C. Kocher, M.J. Kappers, R.A. Oliver, and R.A. Taylor, to be submitted to *Physica Status Solidi (c)* (2013).

- *Coherent Control of the excited state exciton in a non-polar InGaN quantum dot*

B.P.L. Reid, C. Kocher, T. Zhu, F. Oehler, C.C.S. Chan, R.A. Oliver, and R.A. Taylor, in preparation (2013).

- *Linearly polarised single photon emission from a non-polar InGaN quantum dot*

B.P.L. Reid, C. Kocher, T. Zhu, F. Oehler, C.C.S. Chan, T.J. Puchtler, R.M. Emery, R.A. Oliver, and R.A. Taylor, in preparation (2013).

- *Dynamics of Excitonic Emissions of GaN Nanotubes*

Y.S. Park, M.J. Holmes, B.P.L. Reid, R.A. Taylor, K.S. Kim, and H. Im, in preparation (2013).

-
- *Optical anisotropy and bandgap renormalization in valleytronics materials of single and bi-layer MoS₂*
Y.S. Park, S.W. Han, C.C.S. Chan, B.P.L. Reid, R.A. Taylor, S.H. Kim, K.S. Kim, M.G. Park, S. Ryu, and H. Im, in preparation (2013).
 - *Quantum dot-like excitonic behavior in individual single walled-carbon nanotubes*
X. Wang, J.A. Alexander-Webber, W. Jia, M.J. Holmes, C.C.S. Chan, B.P.L. Reid, R.J. Nicholas, C. Deng, and R.A. Taylor, in preparation (2013).

Contents

Contents	6
1 Introduction	9
1.1 Quantum Confined Structures	9
1.2 III-Nitride based structures	10
1.3 Thesis Layout	12
2 Properties of III-N Semiconductors and InGaN Quantum Dots	15
2.1 Crystal Structure & Polarisation	15
2.1.1 Piezoelectricity	17
2.2 Quantum confined Stark Effect	18
2.2.1 Reduction of oscillator strength: Simple example of <i>c</i> -plane QW . . .	19
2.2.2 Electric field in a non-polar InGaN QD	19
2.3 Optical Transitions	21
2.3.1 Nitride band structure	21
2.3.2 Fine structure splitting	22
2.4 Exciton Complexes	24
2.5 Growth of InGaN QDs by modified droplet epitaxy	25
2.5.1 Defects and dislocations	26
2.5.2 Epitaxial layer overgrowth for <i>a</i> -plane InGaN QDs	27
3 Experimental Techniques	28
3.1 Introduction	28
3.2 Excitation Sources	29
3.2.1 Ti:Al ₂ O ₃ Laser	29

3.2.2	UV and Blue excitation	31
3.3	Time Integrated Micro-Photoluminescence	32
3.3.1	Two-photon excitation	34
3.4	Time resolved Micro-Photoluminescence	35
3.4.1	Time correlated single photon counting	35
3.5	Single QD spectroscopy	37
3.5.1	Electron beam lithography	38
3.5.2	Photoluminescence excitation spectroscopy	39
3.5.3	Polarisation-resolved spectroscopy	40
4	Polarisation-resolved spectroscopy of <i>a</i>-plane InGaN QDs	41
4.1	Introduction	41
4.2	Sample growth and spatial localisation of quantum dots	42
4.2.1	Spatial localisation of QDs by Cathodoluminescence	43
4.3	Initial micro-photoluminescence results	44
4.3.1	Exciton and Biexciton dynamics	44
4.3.2	Internal field reduction	47
4.3.3	Thermal stability of QD luminescence	48
4.4	Polarisation-resolved spectroscopy	48
4.4.1	Linearly polarised emission	48
4.4.2	Fine Structure Splitting	53
4.5	Chapter summary	54
5	Origins of spectral diffusion in InGaN QDs	57
5.1	Introduction	57
5.2	Effects of dislocation density on spectral diffusion	58
5.2.1	Sample growth and preparation	58
5.3	Estimation of QD density	59
5.4	Temporal variation in QD luminescence	60
5.4.1	Fast time-scale spectral diffusion	66
5.4.2	Slow time-scale spectral diffusion	67
5.4.3	Effect of electrically active impurities on spectral diffusion	68

5.5	Energy-linewidth relationship in spectral diffusion	70
5.6	Spectral diffusion in <i>a</i> -plane InGaN quantum dots	72
5.6.1	Lower bound for internal field in <i>a</i> -plane InGaN quantum dots	73
5.7	Effect of an external field on spectral diffusion	76
5.7.1	Sample growth	76
5.7.2	Sample fabrication	76
5.7.3	Spectral tuning and narrowing of linewidth of QD luminescence	77
5.8	Chapter summary	78
6	A coherent control scheme for excitons in <i>a</i>-plane InGaN QDs	80
6.1	Rabi Rotations	81
6.2	Photoluminescence Excitation spectroscopy on <i>a</i> -plane InGaN quantum dots	86
6.3	Observation of Rabi Oscillations	88
6.4	Decoherence and the damping of exciton Rabi oscillations	91
6.5	Chapter Summary	93
7	Conclusion	98
	Bibliography	101

1

Introduction

1.1 Quantum Confined Structures

Bloch's theorem [1] motivates a description of charge carrier energy in a solid as a multi-valued function of momentum, the resulting continuous energy bands and gaps a consequence of the de-localisation of the carrier wavefunction over the entire crystal lattice. With the advent of molecular beam epitaxy and metal organic vapour deposition as techniques for the growth of semiconductors, artificial structures that can confine charge carriers in one [2], two [3, 4, 5] or three [6, 7, 8] dimensions have been realised. These structures therefore provide a solid-state route to phenomena associated with energy quantisation previously thought to be restricted to atomic physics. In order to achieve such a confinement, carrier motion should be restricted to distances comparable to the de Broglie wavelength. The de Broglie wavelength has a typical size of order ~ 10 nm for semiconductors, opening up the possibility of engineering control of quantum properties.

Carrier localisation in all three dimensions, as is the case in a quantum dot (QD), leads to a complete breakdown of the classical model of continuous energy dispersion, and the resulting discrete energy levels and delta function-like density of states are analogous to that of a single atom. Photon anti-bunching [9, 10, 11, 12, 13] is an interesting consequence of the quantum-character of quantum dot systems, with exciting applications given the development of all-optical quantum logic algorithms [14]. A key requirement of such proposed systems is that the photons are indistinguishable, meaning each photon has the

same frequency, bandwidth, temporal pulse width and polarization state, as well as the same spatial electric field intensity profile.

Furthermore, quantum interference between two photons requires spatial and temporal overlap of each photon wave packet. To achieve temporal overlap, the time uncertainty in emission should be minimised, meaning a fast spontaneous decay rate of the emitter is desirable. This can be achieved by embedding a quantum dot in an optical cavity [15, 16, 17]. With a sufficiently high cavity quality factor and low mode volume, the strong coupling regime between light and matter can be reached [18, 19, 20, 21, 22]. This means that the strength of light-matter coupling exceeds the decoherence rates of the quantum dot and the cavity mode allowing a reversible transfer of energy and the formation of a new quantum state, as first observed using single atoms in cavities [23, 24]. Such a system would not only provide a test-bed for quantum computation techniques, but also has been used to achieve ultra-low threshold lasing [25, 26, 27].

As well as control of the polarization state of emitted light, on-demand creation of entangled photon pairs would be highly desirable, providing a basis for an efficient quantum cryptography scheme [28]. The biexciton cascade emission from a single quantum dot has been demonstrated as a source of polarization-entangled photons [29, 30, 31, 32, 33, 34].

The deviations of quantum dots from an ideal two level system, namely ability to accommodate several excitations, possible energetic vicinity to continuum states in the surrounding material, Coulomb scattering, and interaction with phonons, can prove a nuisance for the generation of indistinguishable single photons, entangled photon pairs, and attaining the strong coupling regime.

1.2 III-Nitride based structures

III-Nitride semiconductors shot to prominence in the optoelectronics industry with the successful development of blue light-emitting diodes (LEDs) [35] and the blue-violet laser diodes [36] in the 1990s. The wide variation of bandgaps, ranging from between 0.7 eV and 0.9 eV for InN [37][38][39][40], to 3.4 eV for GaN [41], and 6.1 eV [42] for AlN, gives access to the entire visible spectrum through growth of ternary and quaternary alloys.

Compared to a more mature semiconductor system like the III-Arsenides, the fundamental properties of the nitrides are relatively poorly understood. In particular, the development of high-brightness LEDs was at odds with the poor crystalline quality that could be achieved in the nitrides, with the high densities of threading dislocations expected to have an adverse effect [43] on device performance by acting as centres for non-radiative recombination of charge carriers. One postulated reason for the success of InGaN-based LEDs is the formation of quantum dot-like 3D localisation centres within an InGaN quantum well (QW) due to local variations in In content [44]. Indeed, masking an InGaN quantum well with small enough apertures can pick out local In-rich regions and reveal a clear signature of quantum dot emission [45].

Intentionally grown InGaN QDs [46] have become an area of intense study, not only to inform the development of InGaN quantum well based devices, but also due to the blue emission from InGaN quantum dots matching the operation ranges of the best commercially available single photon detectors. Early successes include the observation of single photon emission [47] and spectral tuning of QD emission [48]. The latter case takes advantage of the built-in piezoelectric field in InGaN quantum dots (see chapter 2), the existence of which provides one of the main contrasts to a III-Arsenide based quantum dot. This internal field is also expected to enhanced the suitability of these QDs for applications in quantum information processing [49]. It should be commented however, that the piezoelectric field can also be somewhat of a nuisance, reducing the oscillator strength of the exciton transition [50]. Furthermore, the wide band gap offsets achievable in the III-Nitride semiconductor family can be used to achieve strong confinement in QDs, providing potential for room temperature operation of devices not available to III-Arsenide based systems. As a testament to this, both GaN QDs in an AlGaIn matrix [51] and InGaIn QDs in an AlGaIn nanowire [52] have shown single photon emission up to 200K.

In order to demonstrate cavity quantum electrodynamical effects with InGaIn quantum dots, two main problems must be overcome. The first is achieving a spatial resonance between cavity and quantum dot. The QD formation process described in [46] relies on GaIn capping to take place, meaning identifying the spatial position of a QD is difficult. The second is that of achieving a spectral resonance between cavity and emitter, despite

the demonstration of spectral tuning in [48] the problem of spectral diffusion (spectral shifts of luminescence over time) still remains.

1.3 Thesis Layout

In this thesis, optical techniques are used to investigate fundamental properties of both traditional *c*-plane InGaN quantum dots, as well as newly-developed *a*-plane QDs [53] to reveal both their potential and limitations for use in the applications described above.

In chapter 2, InGaN quantum dots are discussed in the context of the intrinsic properties of the III-Nitrides. The crystal structure of III-Nitrides and the emergence of both spontaneous and piezoelectric polarizations will be introduced, as well as their effect on the QD exciton oscillator strength through the quantum confined stark effect. A simple model of predicted optical transitions will be presented, together with the effect of symmetry of both quantum dot shape and indium content on the associated energy levels. An introduction to different QD growth geometries will also be presented.

Chapter 3 will provide a summary of experimental techniques used, include time-integrated and time-resolved microphotoluminescence, two photon excitation spectroscopy, and the use of electron beam lithography to enable isolation of single quantum dots.

In Chapter 4, the optical properties of InGaN quantum dots grown on a non-polar plane (the *a*-plane) [53] are compared with their polar plane (*c*-plane) counterparts. In particular, the observation of an order of magnitude reduction in the exciton lifetime leads us to deduce a reduction of the internal electric field for *a*-plane quantum dots. In addition, a high thermal stability of both the excitonic emission linewidth and the exciton transition lifetime points to a reduced phonon coupling strength when compared with traditional *c*-plane QDs, suggesting suitability for high temperature applications. Most significantly, the first report of a degree of linear polarization of exactly one for quantum dot emission is presented, and provides a possible route to indistinguishable single photons which is so far unavailable to III-Arsenide or II-VI based QDs. Polarisation-resolved spectroscopy is used to determine the exciton fine structure splitting for several *a*-plane InGaN quantum dots. Spatial mapping of *a*-plane quantum dot wafers using cathodoluminescence reveals

a method of determining the spatial position of a quantum dot using scanning electron microscopy, an important step towards realising the spatial resonance required to achieve cavity quantum electrodynamics with InGaN QDs.

In Chapter 5, I investigate the role of threading dislocations in both the formation of InGaN quantum dots, and the phenomenon of spectral diffusion [54], where the QD emission energy and linewidth change as a function of time. The trend of increase in magnitude of spectral diffusion with sample dislocation density allow the measured spectral diffusion to be attributed to fluctuating electric fields caused by charge carriers becoming trapped at and released from dislocation sites. Further investigations into spectral diffusion in InGaN QDs, support a hypothesis of itinerant carriers in the underlying quantum well layer, or carriers trapped at local maxima in the quantum well potential as a second mechanism for spectral diffusion. This process occurs over much faster time-scales and therefore can partially explain the inhomogeneously broadened lineshape observed as characteristic for both InGaN QD geometries. Quantum dot density as estimated from micro-photoluminescence performed on masked samples shows a trend of increasing quantum dot density with dislocation density, suggesting threading dislocations play a significant role in the formation of InGaN QDs. Analysis of spectral diffusion data for *a*-plane QDs suggests that some internal field still remains in the *a*-plane geometry QDs, which would not preclude the possibility of spectral tuning of luminescence. A possible method for the reduction/elimination of spectral diffusion in *c*-plane InGaN QDs is also presented. A sample with InGaN QDs as the intrinsic layer in a p-i-n structure allows the application of a reverse bias voltage vertically across the QD layer. The resulting external electric field can therefore partially screen the internal field, resulting in a spectral shift of the QD luminescence, and an increase in the oscillator strength as in [48]. In addition to the ability to spectrally tune the QD emission energy, the application of the external field is could reduce spectral diffusion as a consequence of discharging the carriers trapped at dislocations and at local maxima in the quantum well potential. This is shown by a reduction in the QD linewidth with reverse bias applied, suggesting at least the fast timescale spectral diffusion can be “cured” somewhat using this method. This methods make achieving a spectral resonance between an InGaN QD and microcavity a distinct possibility.

In Chapter 6, a coherent control scheme implemented on an excitonic transition in an a -plane quantum dot is demonstrated. Identification of excited state resonances using photoluminescence excitation spectroscopy allows direct excitation of a quantum into a single excited state. Variation of the excitation power under direct excitation into this state is seen to drive Rabi oscillations between the excited exciton state $|1\rangle$ and the crystal ground state of no exciton $|0\rangle$ by observing photoluminescence from the exciton ground state $|s\rangle$. I observe a population transfer of $\sim 57\%$. The dephasing induced by the environment of the quantum dot could be reduced with the inclusion of the QD in a microcavity.

A short summary and conclusion will be presented in chapter 7.

2

Properties of III-N Semiconductors and InGaN Quantum Dots

In this chapter, some general properties of III-N semiconductors, and their application to the specific case of InGaN QDs will be presented.

2.1 Crystal Structure & Polarisation

InN, GaN and AlN can all form in both the wurtzite (space group $P6_3mc$) and zinc blende (space group $F\bar{4}3m$) crystal structures. Zinc blende III-N compounds are unstable under ambient conditions [55], and as such I consider only wurtzite material in this thesis. The wurtzite crystal structure for GaN is shown in figure 2.1. The positions of the two cations and the two anions in the unit cell define a unique polar axis (the c -axis) as there is a vertical separation between the cationic and anionic charge barycentres. This asymmetry gives rise to a permanent electric dipole across the unit cell. The high electronegativity of N, and deviations from an ideal wurtzite crystal structure (one for which $c/a = 3/8$ also contribute to this spontaneous polarisation. Since the crystal directions $[0001]$ and $[000\bar{1}]$ are not equivalent, we can define a particular crystal to be Ga-polar (electric dipole along $[0001]$) or N-polar (electric dipole along $[000\bar{1}]$). Whilst in this work I consider Ga-polar materials, the structure shown in figure 2.1 is N-polar as an aesthetic choice.

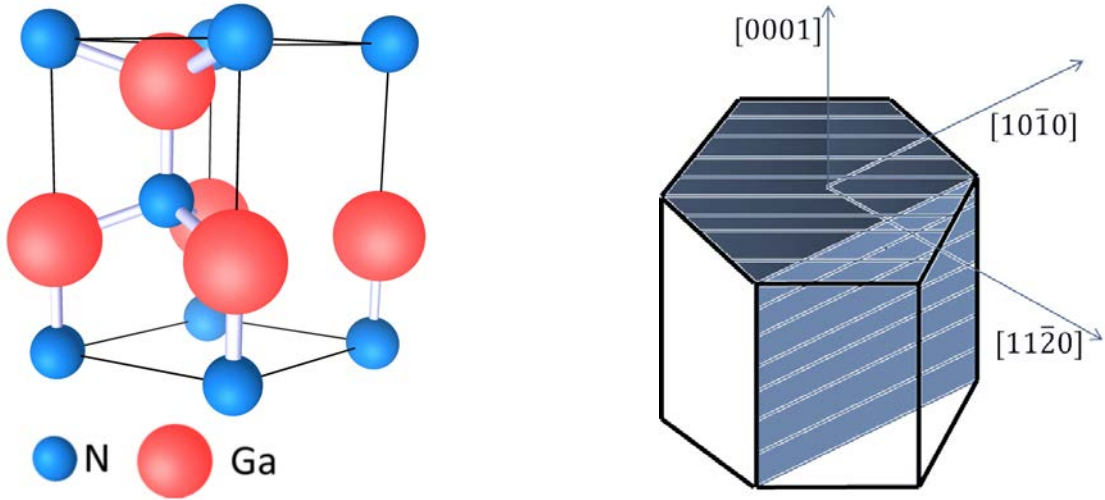


Figure 2.1: Left: Schematic of the wurtzite unit cell for Nitrogen polar GaN. The partial ionic nature of the crystal means there is a mismatch between the anion and cation charge barycentres in the $[0001]$ direction. Right: The hexagonal crystal symmetry means Miller-Bravais indices are preferred to describe crystal planes. Three orthogonal crystal axes, $[0001]$, $[10\bar{1}0]$, and $[11\bar{2}0]$ are shown. The c -plane (0001) is shaded in dark blue. The a -plane $(11\bar{2}0)$ is shaded in light blue.

The lattice parameters for InN and GaN are summarized in table 2.1. For $\text{In}_x\text{Ga}_{1-x}\text{N}$ the lattice parameters will vary with the In composition x according to Vegard's law [56]:

$$a_{\text{InGaN}} = (1 - x)a_{\text{GaN}} + xa_{\text{InN}}. \quad (2.1)$$

In the case of an InGaN quantum dot, we can see that there will be a mismatch between the QD and barrier material lattice parameters. This mismatch causes the quantum dot material to be strained. Indeed, the existence of such a strain is one of the driving mechanisms for quantum dot formation. As mentioned in the introduction one property of InGaN QDs is the internal electric field. The existence of the spontaneous polarisation outlined above has only a small contribution to this field, since the spontaneous polarisation between InGaN and GaN will be similar, meaning only a small discontinuity in polarisation at the edges of the QD. The main contribution to the internal field is the piezoelectric polarisation.

2.1. CRYSTAL STRUCTURE & POLARISATION

	GaN	InN
a (Å)	3.1893	5.1852
c (Å)	3.5365	5.7039

Table 2.1: Typical experimentally determined lattice parameters for InN and GaN taken from [57] and [58]. In both compounds, the ratio c/a deviates slight from the value of 3/8 expected for an ideal wurtzite crystal.

2.1.1 Piezoelectricity

A non-centrosymmetric crystal structure such as wurtzite can exhibit the piezoelectric effect, whereby an external stress can induce a polarisation field. As discussed in the previous section, a lattice mismatch between InGaN and GaN will induce a strain. For a small displacement vector \vec{u} of a cation/anion from it's unstrained position \vec{x} , the strain tensor can be expressed by

$$\epsilon_{ij} = \frac{1}{2} \left(\frac{\partial u_i}{\partial x_j} + \frac{\partial u_j}{\partial x_i} \right). \quad (2.2)$$

The stress tensor is related to the strain tensor according to Hooke's law by $\sigma_{ij} = C_{ijkl}\epsilon_{kl}$ where C is the rank 4 compliance tensor. In the absence of torque, the stress and strain tensors are symmetric, leaving 6 independent components for each. Hooke's law can now be expressed in terms of Voigt notation, the stress and strain tensors become pseudovectors and the Compliance tensor becomes a pseudotensor of rank 2:

$$\begin{pmatrix} \sigma_{xx} \\ \sigma_{yy} \\ \sigma_{zz} \\ \sigma_{yz} \\ \sigma_{xz} \\ \sigma_{xy} \end{pmatrix} = \begin{pmatrix} C_{11} & C_{12} & C_{13} & 0 & 0 & 0 \\ C_{12} & C_{11} & C_{13} & 0 & 0 & 0 \\ C_{13} & C_{13} & C_{33} & 0 & 0 & 0 \\ 0 & 0 & 0 & C_{44} & 0 & 0 \\ 0 & 0 & 0 & 0 & C_{44} & 0 \\ 0 & 0 & 0 & 0 & 0 & \frac{1}{2}(C_{11} + C_{22}) \end{pmatrix} \begin{pmatrix} \epsilon_{xx} \\ \epsilon_{yy} \\ \epsilon_{zz} \\ \epsilon_{yz} \\ \epsilon_{xz} \\ \epsilon_{xy} \end{pmatrix}. \quad (2.3)$$

The compliance tensor is reduced to 5 independent elements by careful consideration of the wurtzite symmetry [59]. We can relate the piezoelectric polarisation to the strain tensor by a tensor of piezoelectric constants $P_i = e_{ijk}\epsilon_{jk}$. For the wurtzite structure there are only 3 independent piezoelectric constants [60] leaving a simple relationship between P and the strain which is best expressed in Voigt notation:

$$\begin{pmatrix} P_x^{\text{PZ}} \\ P_y^{\text{PZ}} \\ P_z^{\text{PZ}} \end{pmatrix} = \begin{pmatrix} e_{15}\varepsilon_{xz} \\ e_{15}\varepsilon_{yz} \\ e_{31}(\varepsilon_{xx} + \varepsilon_{yy}) + e_{33}\varepsilon_{zz} \end{pmatrix}. \quad (2.4)$$

Typical values of the piezoelectric components e_{15} , e_{33} , and e_{31} can be found in [60]. In the case of a perfectly symmetry InGaN QD (both in terms of shape and indium distribution), we can expect an isotropic strain, a reasonable approximation since the lattice mismatch is similar for both the c and a parameters. It is clear then from equation 2.4 that there will exist a polarisation in the c direction [0001]. The discontinuity in polarisation at the base of the quantum dot will therefore cause an internal electric field in the [0001] direction reinforcing the electric field due to the spontaneous polarisation. Of course, it is clear from equation 2.4 that other polarisation directions can exist, but the magnitude of this is thought to be small [61] due to small shear strains (perpendicular to growth direction). In fact, polarisation in a quantum well can be completely eliminated for certain growth geometries [59].

2.2 Quantum confined Stark Effect

The internal field in nitride structures causes a reduction in oscillator strength and a red shift in the emission energy [48]. If we consider the field as a small perturbation $h = -\vec{\mu} \cdot \vec{F}$ to the QD Hamiltonian (where $\vec{\mu}$ is the dipole moment in the QD and \vec{F} is the internal field), then we can extract the first and second order shifts in the QD energy levels from basic perturbation theory:

$$\Delta E_n = \langle n|h|n \rangle + \sum_{k \neq n} \frac{\langle n|h|k \rangle \langle k|h|n \rangle}{E_n - E_k}. \quad (2.5)$$

We can define the polarisability as the constant of proportionality between the second order shift and the square of the field. The linear shift is simply $-\vec{\mu} \cdot \vec{F}$. Considering the first QD energy level ($n = 1$) we can see that the polarisability will be negative (since $E_1 - E_k$ is negative for all $k \neq 1$). If we define as positive quantities the component of the dipole moment along the field μ , and the component of the polarisability along the field

α then we can express the energy shift for the first QD energy level in terms of the scalar magnitude of the field F :

$$\Delta E = \mu F - \alpha F^2. \quad (2.6)$$

Despite the terms creating opposite energy shifts, experimental and theoretical analyses for both vertical [48, 62] and lateral [63, 64] electric fields reveal the values of μ and α are such that the second term will always dominate causing a red shift in emission energy for the first quantum dot energy level.

2.2.1 Reduction of oscillator strength: Simple example of c -plane QW

The reduction in oscillator strength can be understood by considering the effect of the electric field on the electron and hole wavefunctions. The field will increase the spatial separation between electrons and holes as shown in the simple case of a 1D $\text{In}_{0.2}\text{Ga}_{0.8}\text{N}$ QW in figure 2.2. The probability densities were calculated using the freely available software nextnano [65], which enables a self consistent solution of the Schrödinger and Poisson equations for semiconductor heterostructures. The probability densities assuming no polarisation (solution of the Schrödinger equation only) are shown on the left of figure 2.2, this is essentially a solution of a particle in a box with a finite potential barrier. The centre plot of figure 2.2 then allows for solution of the Poisson equation and so takes into account the spontaneous polarisation discontinuity at the InGaN/GaN barrier. We can see that even though the polarisation discontinuity is expected to be small, nevertheless there is an appreciable reduction in the electron-hole wavefunction overlap even when assuming no strain in the structure. Once the piezoelectric polarisation is taken into account using a strain minimisation algorithm based on equation 2.3, we can see a further increase in the spatial separation between electron and hole. Notably, this effect can clearly result in a poor confinement of the hole.

2.2.2 Electric field in a non-polar InGaN QD

Whilst the spontaneous polarisation associated with the Wurtzite structure exists only along the c -axis, we have seen in equation 2.4 that piezoelectric polarisation components

2.2. QUANTUM CONFINED STARK EFFECT

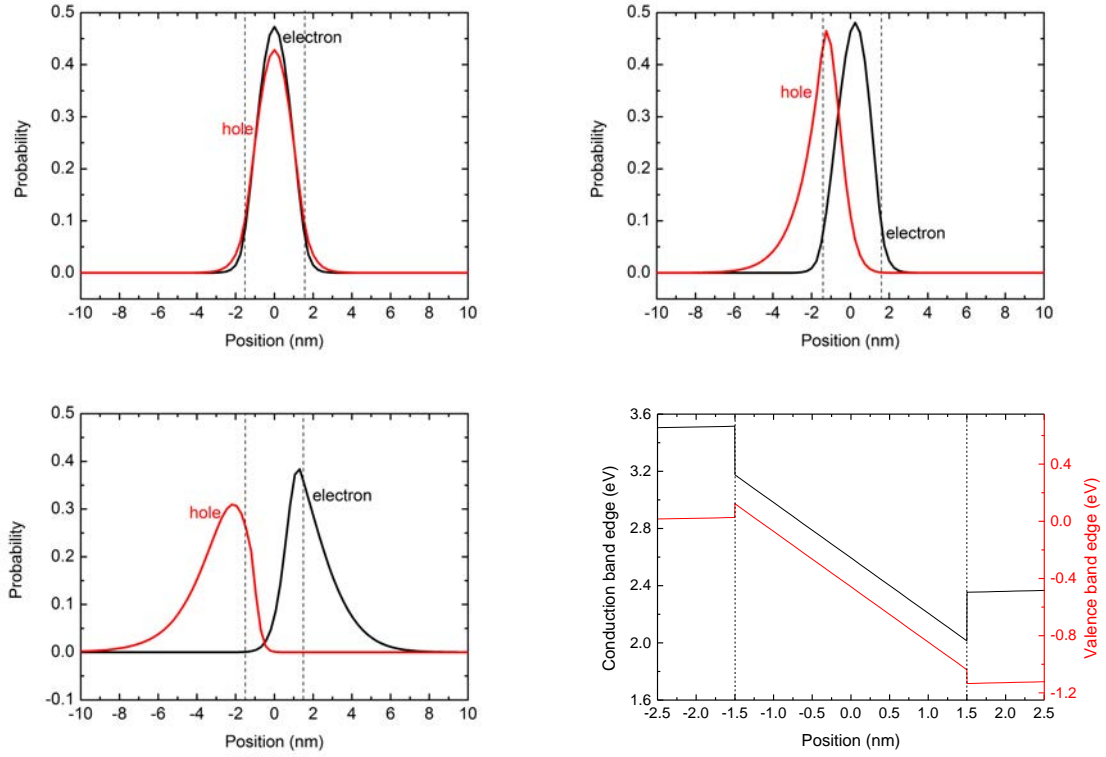


Figure 2.2: Calculated electron (black) and hole (red) probability densities for an $\text{In}_{0.2}\text{Ga}_{0.8}\text{N}$ QW with height 3nm. Top left: Solving Schrödinger equation only. Top right: Self consistent solution of Schrödinger and Poisson equations to take into account the spontaneous polarisation. Bottom left: Self consistent solution of Schrödinger and Poisson equations after minimising the strain energy - thus the piezoelectric and spontaneous polarisations are taken into account. Bottom right: Calculate band structure taking into account the piezoelectric and spontaneous polarisations. The conduction band is shown in black and the valence band in red.

can exist in along all three orthogonal crystal axes. However, the demonstration of field-free *m*-plane (10 $\bar{1}0$) GaN/AlGa \bar{N} QW structures motivates theoretical estimations that the components of the piezoelectric polarisation perpendicular to [0001] should be small [61]. In the case of InGa \bar{N} /Ga \bar{N} , *a*-plane (11 $\bar{2}0$) QWs have been shown to have significantly increased oscillator strengths when compared with their *c*-plane counterparts [66], reinforcing the conclusion that these structures have significant reduced if not eliminated internal fields. It also worth noting that values for the piezoelectric constants vary in the literature, particularly for e_{15} which has been reported as both positive [67, 68] and negative [69].

The case of an *a*-plane InGa \bar{N} QD is not so simple. Even if the basal plane of the QD is parallel to the polarisation in the *c*-direction, the side facets of the QD will still enable a polarisation discontinuity along [0001]. The field created by this polarisation discontinuity is expected to decrease as the angle of the QD side facets increases away from the [0001] direction [70], but with a significant field expected to remain for realistic QD shapes and aspect ratios. We will investigate the predictions of increased oscillator strength but not complete elimination of the internal field in chapters 4 and 5.

2.3 Optical Transitions

In this section, a brief introduction to the optical transitions which can be expected from an InGa \bar{N} QD will be presented.

2.3.1 Nitride band structure

The two tetrahedra in the wurtzite unit cell are formed due to sp^3 hybridization of the atomic orbitals. The symmetry of the states near the conduction band edge of a bulk III-N material is inherited from the *s*-orbitals, and so exhibits spherical symmetry. Correspondingly, the valence band states inherit their symmetry from the *p*-orbitals. The degeneracy between the in plane p_x and p_y states with the out of plane p_z states is lifted by an interaction with the crystal field. The in-plane state degeneracy is lifted by the spin-orbit interaction. The resulting three valence bands are termed A, B, and C for III-Nitrides.

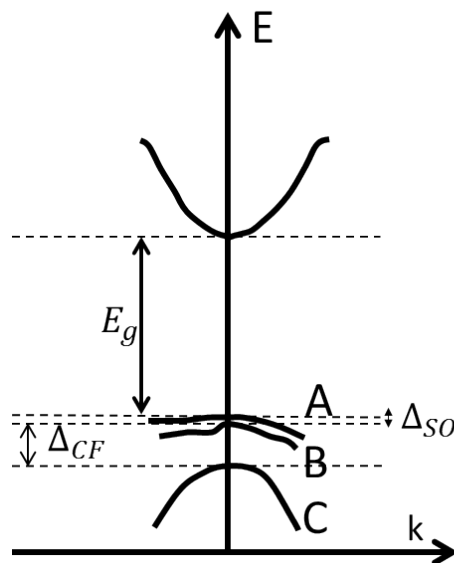


Figure 2.3: GaN band structure near to the Γ point. The conduction band is well approximated by a parabola. The valence band is split into three sub-bands, labelled A, B and C by the spin orbit interaction and an interaction with the crystal field.

Whilst the conduction band is parabolic to a good approximation, the valence bands are highly anharmonic away from the Γ point [71].

2.3.2 Fine structure splitting

For an InGaN QD, the electron states will be quantized, and we can class them by their orbital angular momentum as S , P etc. in analogy with atomic physics. Each of these levels will be doubly degenerate since the electron has spin $\frac{1}{2}$. Each electron energy level as classed by orbital angular momentum will be accompanied by three hole states corresponding to the A, B and C valence bands, which are also doubly degenerate due to spin. An electron-hole pair in a QD is termed an exciton, in analogy with bound electron-hole pairs found in bulk semiconductors.

A perfectly symmetric QD would be expected to have a 4-fold degenerate ground state as outlined in figure 2.4. There are two bright states (electron spin $+\frac{1}{2}$ and hole spin $+\frac{3}{2}$ and electron spin $-\frac{1}{2}$ and hole spin $-\frac{3}{2}$) associated with an angular momentum change of 1. Whilst the two dark transitions (electron spin $-\frac{1}{2}$ and hole spin $+\frac{3}{2}$ and electron spin $+\frac{1}{2}$ and hole spin $-\frac{3}{2}$) associated with an angular momentum change of 2 can be excited by

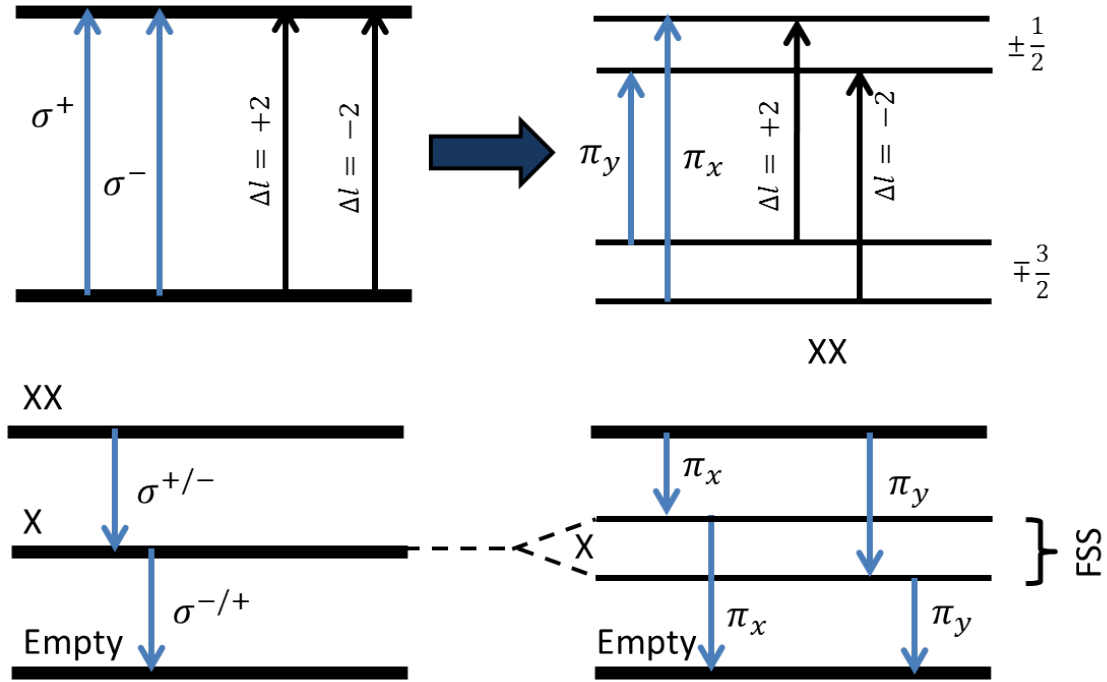


Figure 2.4: Illustration of the fine structure splitting in a quantum dot. Left: The QD ground state of a perfectly symmetric QD with no exchange interaction will have 4 degenerate transitions, two of which are bright (blue) due to the angular momentum change associated with the states being 1, and two dark (black) due to an angular momentum change of two. The bright states are associated with circularly polarised light emission. Right: Exchange interaction and asymmetry in the QD splits the two bright states into two linearly polarised transitions. The energy difference between them is called the fine structure splitting. The cascade decay biexciton-exciton-empty QD is shown for both cases.

two photon absorption, only the bright states will be seen for any form of non-resonant excitation. Any asymmetries in the QD shape or atomistic configuration split the energy of the two bright states. This energy difference is called the fine structure splitting. As well as the energy splitting, asymmetry in the QD changes the nature of the emitted light, with linearly polarised light expected for each of the split energy levels.

In the case of a c -plane QD, any asymmetry in QD shape or atomistic configuration will be random, and as such the polarisation axes of the emitted light will not correspond to any in-plane crystal direction. This makes any measurement of the fine structure splitting difficult, although results have been obtained using unconventional measurement geometries [72].

2.4 Exciton Complexes

For sufficiently high laser excitation power, multiple carriers can become trapped in a QD at the same time, leading to the formation of multi-exciton complexes. Some examples are X^- (two electrons and one hole), X^+ (two holes and one electron) and XX (a biexciton). While a method to identify the presence of charged exciton states has been outlined for GaN QDs [73], the biexciton is rather more simple to identify. If we assume the creation of an exciton in a quantum dot to be a random process, then the number of excitons per pulse the probability P of n excitons per pulse will follow the Poisson distribution:

$$P(n) = \frac{\langle n \rangle^n}{n!} e^{-\langle n \rangle} = \frac{\langle n \rangle^n}{n!} (1 - \langle n \rangle + O(\langle n \rangle^2)), \quad (2.7)$$

where $\langle n \rangle$ is the average number of excitons per pulse. For a single photon excitation, $\langle n \rangle$ is proportional to the excitation power P . Thus, for low excitation powers (small $\langle n \rangle$) the probability associated with at least a single exciton will be given by:

$$1 - P(0) = \langle n \rangle, \quad (2.8)$$

meaning the intensity associated with the single exciton should scale linearly with the power. The probability associated with at least two excitons at low power is:

$$1 - P(0) - P(1) = \langle n \rangle^2, \quad (2.9)$$

corresponding to a quadratic power dependence of the biexciton intensity. For two-photon excitation (see chapter 3), we can invoke Fermi's golden rule for a transition from an initial state 1 to the final state 3 via an intermediate state 2 to give the transition probability for a two photon process T :

$$T_{1 \rightarrow 2 \rightarrow 3} = \left(\frac{2\pi}{\hbar} \right)^2 |\langle 1 | H_{1,2} | 2 \rangle \langle 2 | H_{2,3} | 3 \rangle|^2 \rho_2 \rho_3, \quad (2.10)$$

where ρ_2 and ρ_3 are the intermediate and final density of states respectively. The Hamiltonians $H_{1,2}$ and $H_{2,3}$ associated with the each photon transition will depend linearly on the radiation field \vec{F} , and therefore the square root of the radiation intensity I . Thus,

2.5. GROWTH OF INGAN QDS BY MODIFIED DROPLET EPITAXY

the two photon transition rate given by equation 2.10 depends on the square of the radiation intensity. Therefore, under two photon absorption conditions the average number of excitons $\langle n \rangle$ increases with the square of the excitation power, and equations 2.8 and 2.9 imply that the exciton intensity varies quadratically with the excitation power, whilst the biexciton intensity goes as the fourth power of the excitation power. These dependencies provide a simple method of differentiating between X and XX emission.

2.5 Growth of InGaN QDs by modified droplet epitaxy

All InGaN QDs studied in this thesis were grown using the “modified droplet epitaxy” method [46] at the Cambridge centre for Gallium Nitride (University of Cambridge). Samples are grown by metal organic vapour phase epitaxy (MOVPE) in a 6×2in Thomas Swan close-coupled showerhead reactor. In the case of *c*-plane InGaN QDs, first a GaN buffer layer is grown on a (0001) Al₂O₃ substrate using trimethylgallium and ammonia as precursor gases. This is followed by the growth of an InGaN epilayer using trimethylindium as an indium source. As discussed in the introduction, phase separation causes accumulation of In-rich areas during the epilayer growth. The key step to QD formation is a 30s post-growth anneal in a nitrogen atmosphere (for other growth methods for InGaN QDs, see ref. [74]). An atomic force microscopy image of an uncapped, post anneal InGaN epilayer is shown in figure 2.5.

The low miscibility of InN in GaN gives rise to a spinodal decomposition of the In-rich epilayer regions during the nitrogen anneal, and nanoscale metallic droplets of indium are formed across the epilayer. After the anneal, growth of a GaN capping layer is performed. During the capping layer growth, the In-droplets are thought to re-react with ammonia to form lens shaped InGaN QDs. The areal density of the indium droplets can be estimated as $\sim 10^{10} \text{cm}^{-2}$ from AFM images, but as we shall see in chapter 4, this is far higher than the QD density estimated from microphotoluminescence experiments.

In conventional Stranski-Krastanow QD growth [75], where the strain induced 2D-3D transition that forms QDs also leaves behind a 2D epilayer called the wetting layer. In the modified droplet epitaxy method, the InGaN epilayer is broken up by the formation

2.5. GROWTH OF INGAN QDS BY MODIFIED DROPLET EPITAXY

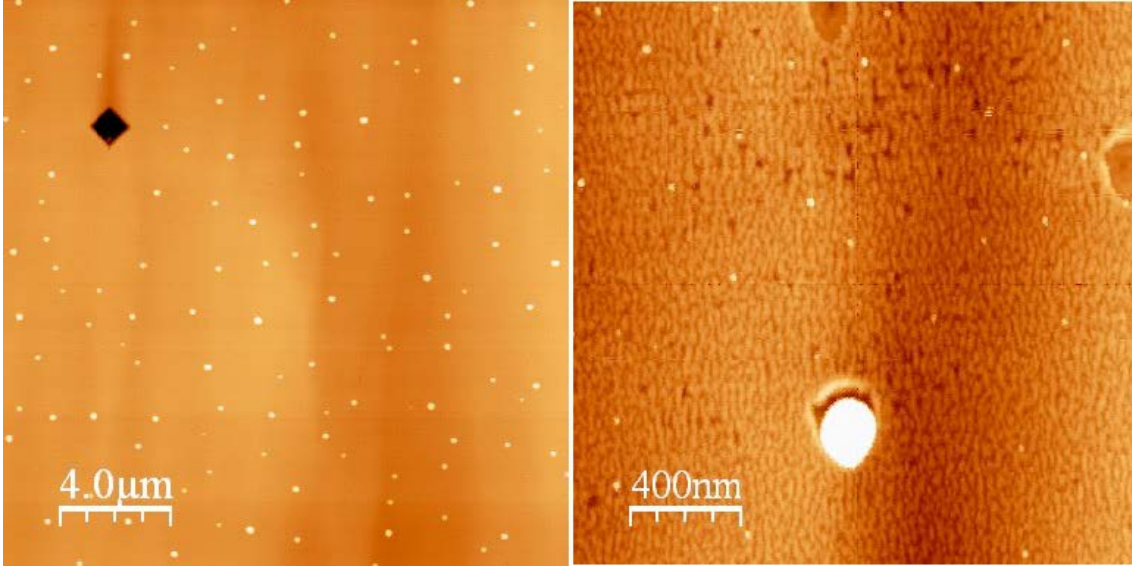


Figure 2.5: AFM images of a nitrogen annealed InGaN epilayer taken at the University of Cambridge by Dr. Tongtong Zhu. The bright spots are metallic droplets of indium which form InGaN QDs during the growth of the capping layer.

of indium droplets, and the remaining damaged quantum well layer sits underneath the quantum dots. This quantum well layer will be subject to considerable thickness and In content variation, meaning a large variation in optical performance over the sample. Two photon excitation, as described in chapter 3, can be used to suppress [76] the QW-like emission in favour of the QD emission lines.

2.5.1 Defects and dislocations

One consequence of the strain in III-Nitride nanostructures is the formation of dislocations. A dislocation occurs when the strain energy is such that it is energetically favourable for an atom to be “dislocated” from the lattice site associated with the values of the lattice parameters a and c in the crystal around it. Such a change can propagate along various crystal axes, termed a threading dislocation. In the case of InGaN QDs, threading dislocations will be present in the InGaN epilayer used to form the QDs both due to the lattice mismatch between InGaN and GaN, and that between the GaN buffer layer and the sapphire substrate. As mentioned in chapter 1, dislocations have a negative impact on device performance by acting as non-radiative recombination centres for charge carriers. In general, the threading dislocation density is found to be similar between an

2.5. GROWTH OF INGAN QDS BY MODIFIED DROPLET EPITAXY

InGaN epilayer and the GaN buffer layer on which it was grown. Dislocation densities can be estimated using AFM and scanning electron microscopy (SEM) imaging [77]. Other defects can involve replacement of Ga/In atom sites with impurities. GaN is thought to be intrinsically n-type due to the presence of nitrogen vacancies [78]. In chapter 4, we will investigate some intentionally Silicon-doped QD samples to model the effect of electrically active impurities.

2.5.2 Epitaxial layer overgrowth for *a*-plane InGaN QDs

InGaN QDs can be grown on the non-polar $11\bar{2}0$ plane by growing a GaN buffer on *r*-plane $1\bar{1}02$ sapphire and using the same modified droplet epitaxy method described above. However, preparation of *a*-plane GaN pseudo-substrates by epitaxial layer overgrowth (ELOG) can provide better sample morphology. After growth of a seed layer of $1\mu\text{m}$ GaN, and a 30nm GaN nucleation layer the sample is removed from the reactor and a 100nm thick SiO_2 layer is deposited using an electron beam evaporator. A wet etch is used to pattern the SiO_2 into $5\mu\text{m}$ wide strips (wings) and $5\mu\text{m}$ wide openings (windows) parallel to $[1\bar{1}00]$, regrowth of $\sim 2\mu\text{m}$ of GaN is performed. The InGaN epilayer and cap are then performed as is the case for *c*-plane InGaN QDs. The so-called “wing” regions of the GaN pseudo substrate can have dislocation densities up to two orders of magnitude lower than for conventional *c*-plane GaN, which should improve the optical properties associated with the QDs.

3

Experimental Techniques

3.1 Introduction

In this chapter I introduce the experimental techniques I exploit to investigate the properties of InGaN QDs. Most of the techniques introduced revolve around optical excitation using an ultrafast pulsed laser. The laser energy must be higher than either the bulk GaN bandgap, the bandgap of the underlying InGaN QW or the lowest exciton state in a QD. When the laser energy is sufficient, the high peak power associated with a laser pulse can create a plasma of charge carriers which quickly relaxes by interaction with the crystal lattice, and the resulting diffusion of carriers enables capture of electrons and holes by individual QDs. Even in cases where less than one electron-hole pair is created per quantum dot, this relaxation and capture process happens on a \sim ps timescale [79]. Excited carriers trapped in a quantum dot will recombine according to a mono-exponential decay law [80], and the resulting photoluminescence can be collected by an objective lens, and dispersed using a diffraction grating to measure the emission spectrum associated with the QD. This is referred to as *time-integrated photoluminescence* and will be discussed in section 2. Typical lifetimes (statistical averages of time taken for the recombination of carriers) for InGaN QDs are much larger than the timescale for carrier relaxation and capture by a QD. This allows measurements of arrival times of emitted photons to be used to infer the lifetime by an indirect measurement of the decay statistics. This method, *time resolved photoluminescence* will be discussed in section 3. Variation of the laser power

(for example, identifying a biexciton as in chapter 2 section 4), wavelength (see section 4.2), and temperature can effect the emission spectrum and thus provide an insight to the fundamental properties of the QDs.

In order to distinguish the optical emission from a single quantum dot, a metal mask patterned with apertures can be fabricated to reduce the observed quantum dot density, and provide a method to return to the same QD for either repeat experiments or further investigation. This method will be discussed in section 4. As well as the possibility of multiple quantum dot emissions in the same measured spectrum, the underlying InGaN quantum well layer left over from the QD growth will provide a broad emission spectrum that will be superimposed on the QD emission. This quantum well background can be reduced using the two-photon excitation technique described in section 3.3.1.

3.2 Excitation Sources

3.2.1 Ti:Al₂O₃ Laser

The development of ultrafast tunable solid-state lasers [81] has had a significant impact on spectroscopic studies across many scientific fields. The main laser used in the studies in this thesis is a *Coherent Mira 900* Ti:Sapphire laser capable of both pulsed and continuous wave operation over a wide range of wavelengths ($\sim 700 - 1000$ nm). The active medium is an Al₂O₃ crystal doped with Ti³⁺ ions. The Ti:Sapphire laser is optically pumped with a *Coherent Verdi V8* diode laser operating at 532 nm. The *Verdi* operates based on generation of the second harmonic (using a lithium triborate crystal) of a 1064 nm Nd:YVO₄ gain crystal which is itself optically pumped by 808 nm fibre coupled laser diodes [82]. The 532 nm *Verdi* beam operates at a power of 8 W, and the Ti:Sapphire output power is typically ~ 1 W.

The broad tunability of the Ti:Sapphire laser is due to the fact that the electronic states of the Ti³⁺ ions couple to the continuum of vibrational states in the Al₂O₃ crystal. The absorption band for the crystal is similarly broad (400 – 600 nm). The Ti:Sapphire crystal is non-centrosymmetric, meaning non linear optical effects can take place. The most useful

of these is Kerr lens modelocking [83, 84]. The dielectric polarization density \vec{P} can be expanded as a power series in the electric field \vec{E} :

$$P_i = \epsilon_0 \left(\chi_{ij}^{(1)} E_j + \chi_{ijk}^{(2)} E_j E_k + \chi_{ijkl}^{(3)} E_j E_k E_l + O(4) \right). \quad (3.1)$$

The symmetry of the Ti:Sapphire crystal means a non-zero $\chi^{(3)}$ [85], and therefore the electric displacement can be expressed:

$$\vec{D} = \epsilon_0 \epsilon_r \vec{E} = \epsilon_0 \left(1 + \chi^{(1)} + \chi^{(3)} |\vec{E}|^2 \right) \vec{E}. \quad (3.2)$$

Assuming the non-linear contribution to the electric displacement is small enough to permit the use of a binomial expansion, then the refractive index $n = \sqrt{\epsilon_r}$ can be expressed:

$$n = n_0 + \frac{1}{2n_0} \chi^{(3)} |\vec{E}|^2 = n_0 + n_2 I, \quad (3.3)$$

where n_0 is the linear part of refractive index and n_2 is the non-linear contribution to the refractive index. The form of equation 3.3 clearly shows that the laser intensity can induce changes in the local refractive index in the Ti:Sapphire crystal.

Assuming a Gaussian intensity profile $I(r) = I(0)e^{-gr^2}$ for the laser beam, with a shape parameter g , we can immediately see that refractive index changes according to equation 3.3 will be larger for smaller r . This leads to a self-focussing effect. At small r linear diffraction of the beam will balance the non-linear self-focussing effect. The higher intensity associated with pulsed modes of the laser cavity means these modes will have a smaller mode volume due to the self-focussing effect. Therefore, positioning a slit in the cavity can exclude continuous wave modes and lock the laser operation to a high peak power pulsed mode.

Using this effect there are two operation modes for this laser, *pico* with a pulse duration of 1 ps, and *femto* with a pulse duration of 100 fs. The repetition rate is ~ 76 MHz which corresponds to a time between pulses of ~ 13 ns. From Heisenberg's uncertainty relation, it is intuitive that the *pico* mode will provide a better energy resolution than the *femto*

mode. In fact, the laser mode can be well approximated by a hyperbolic secant pulse shape in time:

$$I(t) = I(0)\text{sech}^2\left(\frac{t}{\tau}\right), \quad (3.4)$$

where the value of τ corresponds to the quoted pulse durations. The time full width at half maximum (FWHM) can then be calculated to be:

$$\Delta t = \frac{\tau}{2} \ln(3 + \sqrt{8}). \quad (3.5)$$

Considering the Fourier transform of the intensity profile, $F(\nu) \propto \text{sech}^2(\pi\nu)$, the frequency full width half maximum will be:

$$\Delta\nu = \frac{1}{\pi^2\tau} \ln(3 + \sqrt{8}). \quad (3.6)$$

From this we can calculate the time bandwidth product:

$$\Delta\tau\Delta\nu = \frac{(\ln(3 + \sqrt{8}))^2}{\pi^2} = 0.315. \quad (3.7)$$

From this we can extract an energy resolution of $\Delta E = 1.3 \text{ meV}$ for *pico* mode and $\Delta E = 13 \text{ meV}$ for *femto* mode. To achieve this spectral narrowing in *pico* mode, a Gires-Toutnoit interferometer is introduced into the cavity and a three-plate birefringent tuning element is needed. For this reason, *pico* mode is preferred in the optical experiments in this thesis. However, for UV excitation the *femto* mode is required as only the *femto* mode provides sufficiently high peak power to achieve the frequency tripling described in the next section.

3.2.2 UV and Blue excitation

In order to achieve a laser wavelength above the bandgap of the InGaN QDs/QW (blue) or above the bulk GaN bandgap (UV) an *Inrad 5-050* ultrafast harmonic generation system for generation of the second (blue) and third (UV) harmonics of the Ti:Sapphire laser (red-IR) is used. This consists of two non linear crystals. The first crystal (lithium

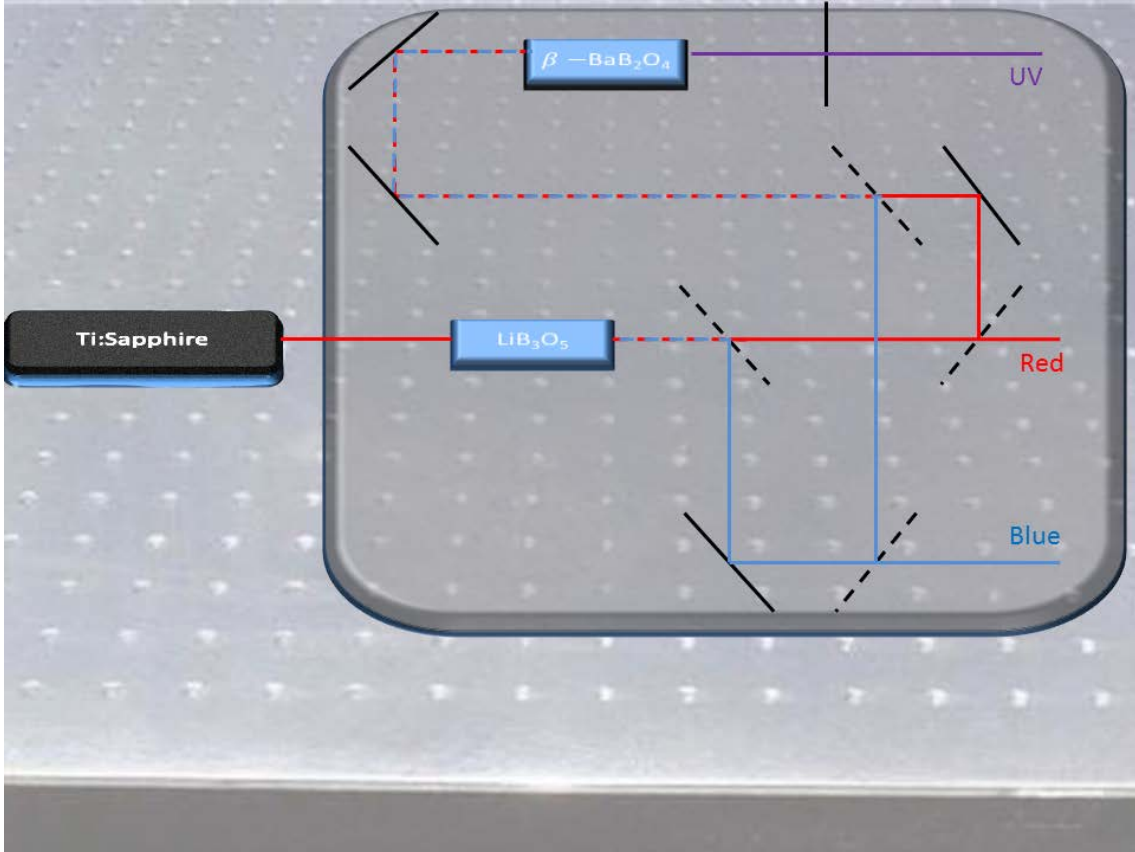


Figure 3.1: Internal setup of the *Inrad 5-050* harmonic generator. Both blue and UV beams can be generated. A component of the original Ti:Sapphire beam can also be extracted from the system to use as a time base for time resolved experiments.

triborate LiB_3O_5) can be positioned such that the phase matching condition can be met for frequency upconversion to take place. For a Ti:Sapphire wavelength of 800 nm, two components, one at 800 nm and one at 400 nm will exit the first crystal. These can be split by a beam-splitter and the 400 nm beam only used as the excitation source for $\mu\text{-PL}$. Alternatively, the 400 nm and 800 nm components can be directed into the second crystal (beta barium borate $\beta\text{-LiBaB}_2\text{O}_4$ to create a third harmonic at 266 nm. The operation of the *Inrad 5-050* is summarised in figure 3.1.

3.3 Time Integrated Micro-Photoluminescence

Other than the excitation system, the major part of the optical setup used to probe the properties of InGaN QDs is a far-field confocal microscope. The micro-photoluminescence setup is summarised in figure 3.2.

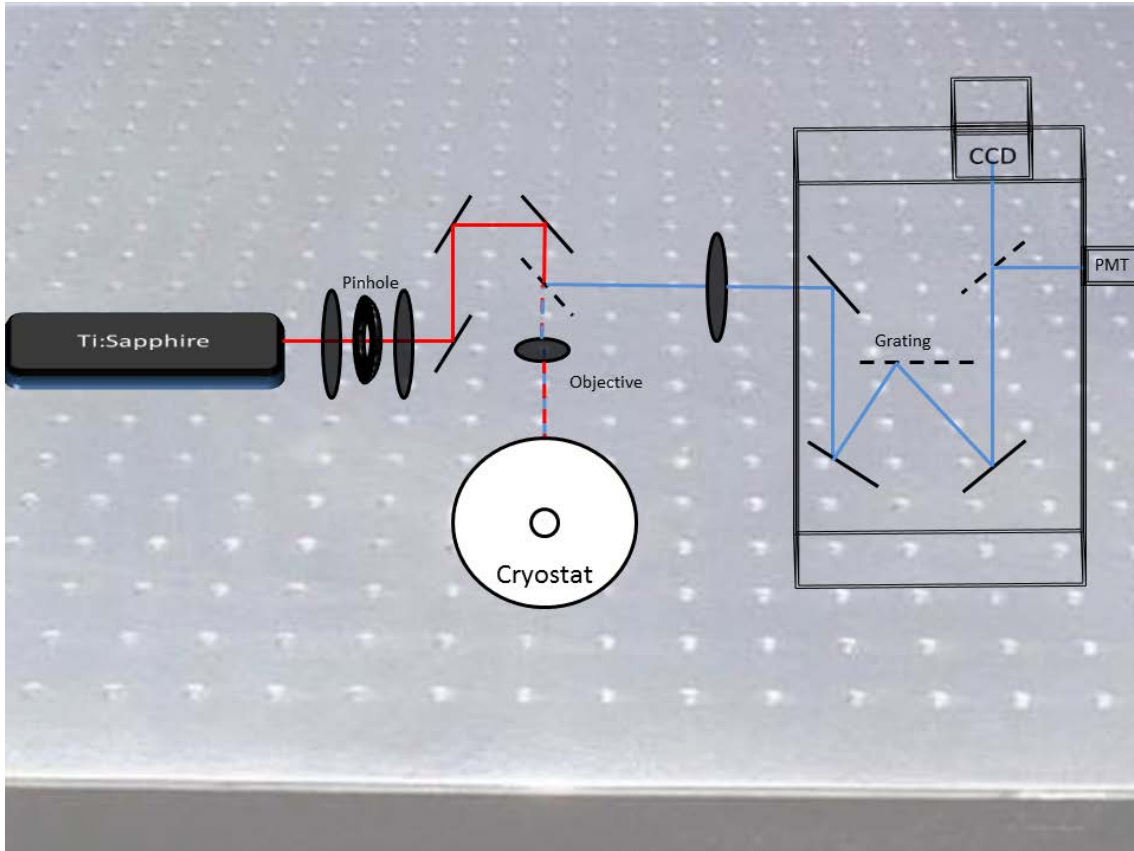


Figure 3.2: Schematic of μ -PL setup for two-photon excitation. The Ti:Sapphire laser beam passes through a spatial filter (pinhole) and a periscope is used to create a top-down excitation geometry. A dichroic mirror is used to separate reflected laser and emitted PL which is directed to the spectrometer. The emitted PL is dispersed off a grating and a simple flip mirror can be used to send the PL to a charged couple device to measure the emission spectrum or a photomultiplier tube to measure the time resolved PL.

The beam from the Ti:Sapphire is first focussed onto the centre of a $50\ \mu\text{m}$ pinhole to act as a spatial filter. The filtered beam is then recollimated by a lens with focal length chosen so that the beam fills the objective lens aperture in order to gain the maximum numerical aperture of the objective lens. A dichroic mirror (*Semrock Brightline*) is used so that close to 100% of the incoming laser beam enters the objective lens, which focusses the laser beam onto the region of interest in the sample.

The sample is held in a continuous flow *Janis ST-500* cryostat equipped with a heating resistance (with a feedback loop) so that the range of accessible temperatures is 4.2–300 K, with a temperature stability $\sim 50\ \text{mK}$. The cryostat has a support structure which exhibits low thermal expansion, and an internal vibration isolation system to reduce any drift of

the sample under excitation.

The emitted photoluminescence is collected by the same objective and the dichroic mirror ensures close to 100% of the emitted PL is directed towards the spectrometer. A *Mitutoyo* 100× achromatic-corrected objective with a numerical aperture of 0.5 is used. The objective is attached to a *Melles Griot Nanomax TS 3-Axis Flexure* nano-positioning stage. This consists of piezoelectric crystals which can be driven with a positional resolution of ~ 10 nm, and controlled by a close feedback loop to ensure positional stability and allow an absolute measurement of position of the objective. The piezo-stage can also be controlled by computer, which gives access to a μ -PL mapping technique which can be used to determine whether lines are from the same or different QDs and to measure the laser spot size ($\sim 1\mu\text{m}$). A program designed to perform raster scans at an arbitrary angle can give information about the positional spread of the quantum dots, as well as more complicated experiments in other material systems [86].

A *Shamrock 303i* 0.303 m spectrometer with three diffraction gratings (300, 600, and 1200 lines/mm) is used to disperse the collected luminescence. The dispersed light is detected using a thermoelectrically cooled, back-illuminated *Andor DU420A-BV* charge coupled device (CCD) with an array of 1024×255 pixels. The pixel size of $26\mu\text{m}$ when used in conjunction with the 1200 lines/mm grating offers an available spectral resolution ranging from $350\mu\text{eV}$ – $500\mu\text{eV}$ in the typical range of QD wavelengths from 500–420 nm. An automated flipper mirror can be used to send a particular wavelength of light to a *Hamamatsu PMH-100* photo-multiplier tube (attached to a stepper motor to ensure good alignment) for time-resolved studies.

The *Andor* CCD software allows a manual wavelength calibration of the offset. In the typical wavelength range for our InGaN QDs, two mercury lines from the room lights can be used for this purpose. They are 404.6565 nm which corresponds to the $7s^1S_0 - > 6p^3P_0$ transition and 435.8335 nm which corresponds to the $7s^1S_0 - > 6p^3P_0$ transition [87].

3.3.1 Two-photon excitation

As well as excitation above the band gap of either bulk GaN, underlying InGaN quantum well or InGaN QD, we have seen in equation 2.10 that two-photon absorption can take

place, with exciton intensity varying as the square of the excitation power. The two-photon absorption cross section has been predicted to increase for structures exhibiting enhanced quantum confinement [88, 89, 90]. Thus, we would expect that our InGaN quantum dots will have a higher two-photon absorption cross section (due to their delta-function-like density of states) than the underlying quantum well layer. Indeed, it has been confirmed experimentally for our InGaN QDs that two-photon excitation increases the QD signal to QW background ratio [76, 91]. It should be noted that this method of excitation is related to two-photon absorption by a virtual intermediate state and not to excitation by the second harmonic generated by the non-centrosymmetric GaN crystal, as confirmed by auto-correlation measurements [92].

3.4 Time resolved Micro-Photoluminescence

As well as measuring the emission spectrum via time-integrated micro-photoluminescence, we are also interested temporal information about the quantum dot emission, in particular the decay statistics of the excited quantum dot levels. We can access this information using a technique called *time correlated single photon counting*.

3.4.1 Time correlated single photon counting

Since the Ti:Sapphire laser excitation is pulsed, the emitted PL signal will be periodic in time, the period corresponding to the repetition rate of the laser (i.e $\sim 13\text{ns}$). By inserting a glass slide into the beam path, a small fraction of the beam can be diverted to a SYNC photodiode which uses the periodic laser signal as a timebase for the detection of the emitted PL. The detection times of individual PL photons are then measured over many laser pulses in order to build up a statistical histogram which will mimic the original PL waveform. This method relies on the probability of detecting a photon at a particular time being much less than unity, meaning the probability of simultaneous arrival of two-photons can be neglected.

For time-resolved PL, a commercial *Becker & Hickl SPC-630* time correlated single photon counting system is used to measure the arrival times of emitted PL photons. It's operation

3.4. TIME RESOLVED MICRO-PHOTOLUMINESCENCE

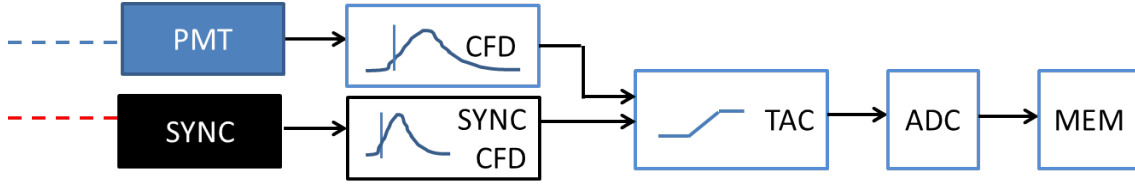


Figure 3.3: Internal working of *Becker & Hickl SPC-630* time correlated single photon counting system. The constant fraction discriminator (CFD) gives a logic pulse which is temporally correlated with the detection of a photon at the photomultiplier tube (PMT). This pulse triggers the time-to-amplitude converter (TAC) which generates a linear voltage ramp stopped by a signal from the SYNC photodiode which takes as its input the periodic laser signal. The analogue-to-digital-converter (ADC) stores the temporal location of each detected PL photon in the memory.

is summarised in figure 3.3. Both the SYNC photodiode and the PMT use a constant fraction discriminator (CFD) to give a logic pulse that is temporally correlated with the photon detection.

The operation of the CFD is summarised in figure 3.4. It uses a pulse shaping network to convert the unipolar detector pulse into a bipolar pulse. The top amplifier in figure 3.4 is a leading edge discriminator. It generates a logic pulse which is time-correlated with the leading edge of any pulse created at the photodiode. The bottom amplifier takes a bipolar input, with a delayed copy of the photodiode pulse as its negative input. The zero-crossing point of the bipolar pulse is used as a time stamp for the arrival of a photon at the photodiode. The leading edge discriminator can be set to a certain threshold below no logic pulse will be created at the output, thus eliminating creation of logic pulses related to any noise in the photodiode.

The logic pulse created by the constant fraction discriminator generates a linear voltage ramp in the time-to-amplitude converter (TAC), which is stopped by the arrival of a logic pulse from the SYNC constant fraction discriminator. This allows the build up of a histogram of arrival times between two subsequent laser pulses. Occasionally, the measured InGaN QDs have a lifetime longer than $\sim 13\text{ns}$, and so we require a reduction of the repetition rate of the laser in order to measure them using time correlated single photon counting. We can achieve this using a pulse picker, *APE PulseSwitch* which relies on the Pockels effect, a non-linear optical effect related to the second order susceptibility (see

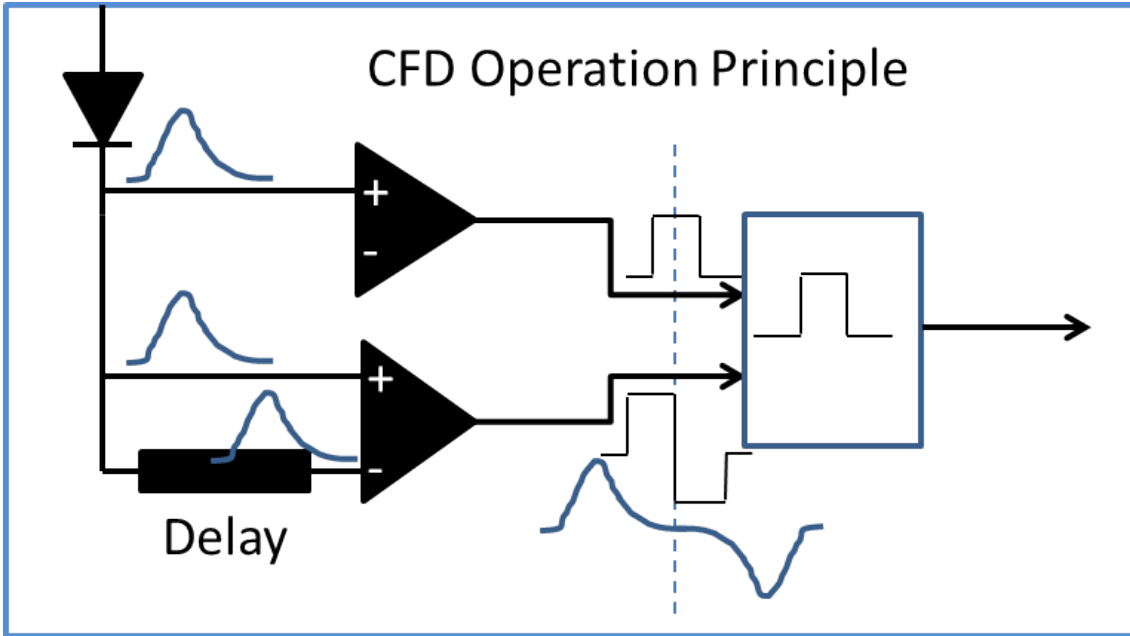


Figure 3.4: Internal working of the constant fraction discriminator (CFD) in the *Becker & Hickl SPC-630* time correlated single photon counting system. The top amplifier is a leading edge discriminator which generates a logic pulse on the leading edge of any optical pulse entering the photodiode. The bottom amplifier takes a bipolar pulse as input and uses the zero crossing point to put a time stamp on the detected photon. If the zero-crossing point as measured for the bipolar pulse corresponds to a threshold intensity measured in the leading edge discriminator then a logic pulse is created which is correlated to the arrival time of the photon at the photodiode.

equation 3.1). A radio-frequency (RF) signal is applied to a fused silica crystal causing a modulation in the refractive index in the crystal. This refractive index modulation causes the crystal to act of a grating to the laser beam which is diffracted into several orders, meaning application of short RF pulses can allow transmission of only certain beam orders, changing the effective repetition rate of the laser. With the pulse picker, we can measure lifetimes as long as $\sim 130\text{ns}$, at the cost of a reduction in the available excitation power but no loss in detected signal, since the dot can only re-emit once it has decayed.

3.5 Single QD spectroscopy

In order to best study the fundamental properties of InGaN QDs, it is important to be able to isolate the photoluminescence from a single InGaN QD. For this purpose, a mask

of apertures is used in order to study and restudy defined areas of InGaN QD wafer. With 500nm to 1 μ m apertures, it is possible to find apertures which contain only one optically active InGaN quantum dot. After coating a wafer piece with metal (Al - 100nm or Au - 65nm), we define this pattern of apertures in a chemical resist by electron beam lithography, the patterned resist is then developed and transferred by wet etch to the metal. Metal-layers are deposited using an *Edwards 306* thermal evaporator.

3.5.1 Electron beam lithography

A *JEOL JBX-5500ZC* electron beam lithography system is used. Its basic components are a sample holder, a ZrO/W electron field emission gun, and focussing optics - the electron optic system (EOS). After laying down the metal mask, the sample is coated in e-beam resist. I use poly(methyl-2-methylpropenoate) (PMMA) in an anisole solvent. A typical recipe uses 950 PMMA A7 (7% PMMA in anisole), which is spin-coated onto the sample at 4500rpm, creating a PMMA coating of thickness 800nm as measured by an ellipsometer. After spinning, the sample is heated to 180° for 90s to evaporate the solvent. The sample is placed into an e-beam cassette and loaded into the sample exchange chamber. After pumping down the chamber to a pressure of $\sim 10^{-5}$ mbar the cassette can be moved into the main e-beam chamber and exposed. The EOS focusses the electron beam to selectively expose a defined pattern on the resist. On collision with the resist, the high energy electrons causes the long PMMA polymer chains to break up into shorter chains. The resist can then be developed (selective removal of exposed resist) using a suitable solvent. In this case methyl-isobutyl-ketone (MIBK) and isopropanol (IPA) is used in the ratio 1 : 3. For a resist thickness of 800nm, 30 – 60s is sufficient for development of the written pattern. The developed pattern can be transferred to the metal layer using a wet chemical etch solution. For aluminium, I use a commercial alkaline soap *Decon 90*. For gold, I use a commercial etching solution which consists of KI:I₂:H₂O in the ratio 1 : 4 : 40 by mass. An example of a pattern of 1 μ m apertures in aluminium can be seen in figure 3.5. It should be noted that this wet etching step sets an effective resolution limit (~ 500 nm) for the pattern features that is far higher than the resolution limit of the e-beam system (~ 7 nm). Further work employing reactive ion etching could decrease mask aperture size

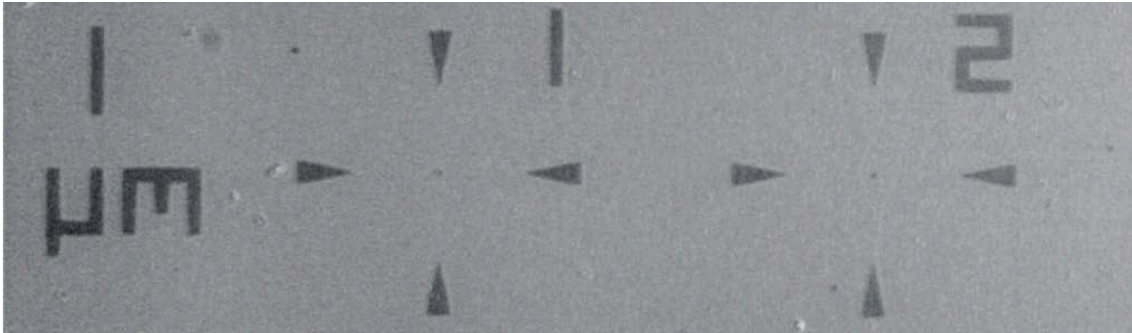


Figure 3.5: Optical microscope image of a InGaN quantum dot sample masked with a pattern of $1\mu\text{m}$ apertures in aluminium.

as in [72]. However, a pattern of 500nm holes is sufficient to optically isolate single InGaN QDs due to the relatively low dot densities present in our samples.

3.5.2 Photoluminescence excitation spectroscopy

One of the great benefits of the Ti:Sapphire laser system is its tunability, and as such we can investigate changes in the optical emission when the excitation energy is changed, this is called photoluminescence excitation spectroscopy (PLE). In the blue spectral range, performing PLE is difficult since a doubled Ti:Sapphire beam is the most common tunable blue laser source. Different Ti:Sapphire wavelengths will generate second harmonics at slightly different angles in the LiB_3O_5 doubling crystal, leading to slight beam misalignment as the laser is tuned, making systematic measurements challenging. No such problem exists using a two-photon excitation scheme, and we can thus perform two-photon PLE measurements. In its most basic form, PLE consists of monitoring the intensity of the optical emission from a quantum dot whilst the excitation wavelength changes, revealing information about resonant absorption in the QD from excited states as well as absorption into continuum states in the underlying quantum well layer. An example spectra is shown in figure 3.6. While the simple model in section 2.4 suggests that one-photon and two-photon transitions will occur at different energies, it should be noted that it is theoretical predicted that a channel of two-photon transitions with the same energies as one-photon transitions exist for $\text{P6}_3\text{mc}$ quantum dots [93]. Indeed, this has been shown to be the case experimentally for wurtzite CdS quantum dots [94].

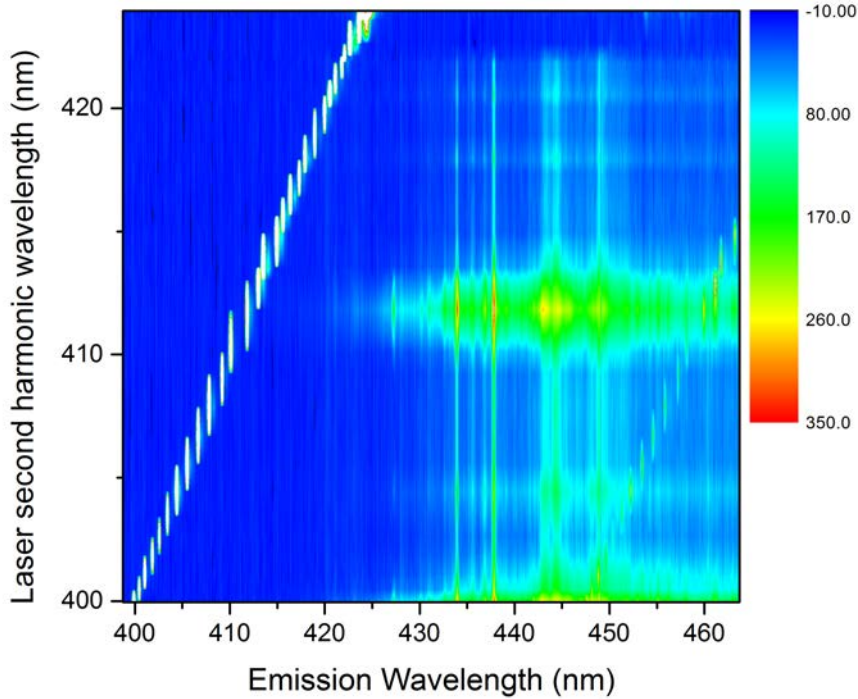


Figure 3.6: Example PLE spectra from an *a*-plane InGaN quantum dot. The PL intensity is shown by the colour scale, and PL wavelength is plotted against the wavelength of the second harmonic, the effective excitation wavelength. Two QD emission lines can be seen at ~ 434 nm and ~ 438 nm, and there are several excited state resonances at lower energy than the quantum well continuum states at ~ 400 nm.

3.5.3 Polarisation-resolved spectroscopy

A Glen-Thompson linear polariser can be used in conjunction with a half-wave retardation plate in the path of the emitted photoluminescence before the spectrometer to select light which is linearly polarised in a certain direction. Due to possible polarisation properties of the spectrometer grating, the half-wave plate should be rotated in order to achieve maximum intensity of a quantum dot emission line, and then rotated by an angle 2θ for every angle θ that the polariser is rotated when analysing polarisation properties of a single quantum dot.

4

Polarisation-resolved spectroscopy of a -plane InGaN QDs

4.1 Introduction

In this chapter we present the first report on μ -PL experiments performed on non-polar InGaN quantum dots. Non-polar growth has been previously attempted on the m -plane ($10\bar{1}0$) [95], and the semi-polar ($11\bar{2}2$) plane, as well as for GaN/AlGaN quantum dots [96] but this work represents the first report of growth of InGaN QDs on the a -plane ($11\bar{2}0$) [53] as well as the first report of μ -PL for InGaN QDs grown on a non-polar plane. Firstly, the sample growth techniques presented in section 2.5.2 will be reviewed, and an overview of results obtained in the university of Cambridge which suggest a possible mechanism for spatial localisation of a -plane InGaN QDs using scanning electron microscopy and cathodoluminescence will be given. In the second section, time-integrated and time-resolved spectra will be presented which show a large reduction in exciton lifetimes when compared to typical exciton lifetimes in polar (c -plane) InGaN quantum dots. This is indicative of a reduced internal electric field and points to the promise of applications of a -plane InGaN quantum dots as single photon sources. To confirm the existence of quantum dot luminescence, the presence of excitons and biexcitons will be confirmed by power-dependent spectroscopy as described in section 2.4. Also, the observation of a better thermal stability of QD emission when compared to c -plane InGaN QDs will be discussed.

The third section turns to the topic of polarisation-resolved spectroscopy of *a*-plane InGaN QDs. Including the demonstration of 100% linearly polarised quantum dot emission from some quantum dot emissions, as well as a measurement of the fine structure splitting for some non-100% linearly polarised transitions.

4.2 Sample growth and spatial localisation of quantum dots

The samples were grown in the university of Cambridge in a Thomas-Swan 6×2 in close-coupled showerhead reactor on *r*-plane ($1\bar{1}02$) substrates with trimethylgallium, trimethylindium and ammonia as precursor gases. *a*-plane GaN pseudo-substrates were prepared by epitaxial layer overgrowth as described in section 2.5.2. The V:III ratio of ~ 740 chosen during regrowth of GaN on top of the SiO_2 layer has been shown to improve luminescence properties of *a*-plane InGaN quantum wells [97]. The ELOG method for the preparation of GaN psuedo substrates has been shown by transmission electron microscopy measurements [98, 99] to significantly reduce dislocation density in the “wing” regions of the substrate. The ELOG growth technique is known to cause basal stacking faults (BSFs) [100], a one or two layer interruption in the stacking sequence from the ABAB expected for wurtzite to the ABCABC stacking expected in a zinc-blende structure. In the wing region, the majority of the BSFs are found near to the coalescence boundary between wing and window. The $+c$ -wing exhibits a threading dislocation density of $< 1 \times 10^6 \text{ cm}^{-2}$ and a BSF density $2 \pm 0.7 \times 10^5 \text{ cm}^{-1}$ compared to a threading dislocation density $(1.0 \pm 0.06) \times 10^{10} \text{ cm}^{-2}$ and BSF density $2.6 \pm 10^5 \text{ cm}^{-1}$ in the window region. An AFM image of the wing and window regions is shown in figure 4.1. The bright spots indicate the presence of droplets of metallic indium characteristic of the pre-anneal step InGaN epilayer in a modified droplet epitaxy growth scheme. The dark spots are the surface terminations of threading dislocations and a clear reduction in dislocation density for the wing region can be seen. This reduction in dislocation density could be responsible for the encouraging results on spectral diffusion in *a*-plane InGaN quantum dots presented in chapter 5. However, it should be noted that the formation of the indium droplets as can be seen in figure 4.1 appears to be uniform over both wing and window regions.

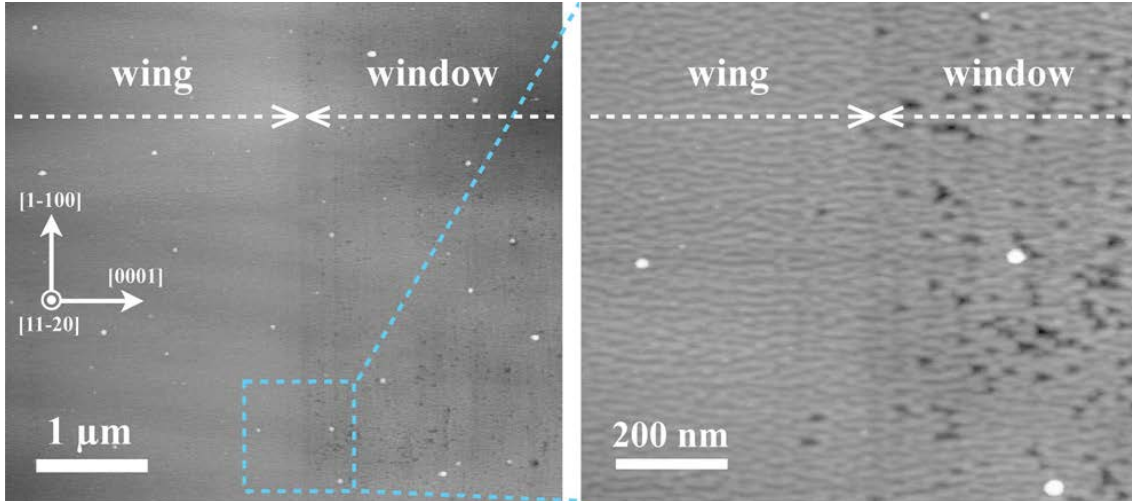


Figure 4.1: AFM image taken at the university of Cambridge of pre-anneal step InGaN epilayer prepared using an ELOG a -plane GaN pseudo-substrate. The bright spots are the indium droplets characteristic of the modified droplet epitaxy approach to QD growth. The dark spots are surface pits associated with the termination of threading dislocations, a reduced dislocation density in the wing region is apparent although indium droplets form in wing and window regions.

4.2.1 Spatial localisation of QDs by Cathodoluminescence

A technique to spatially locate quantum dots is especially important to cavity quantum electrodynamic applications, where a spatial resonance between cavity and emitter is required. Currently, no technique exists to locate the quantum dots formed in a modified droplet epitaxy approach due to uncertainties in the role of the capping process in quantum dot formation. In figure 4.2, AFM data taken at the university of Cambridge shows the formation of large indium droplets at surface pits in the InGaN epilayer after the N_2 anneal step. A CL/SEM image overlay shows that these surface pits correspond to bright spots in the CL emission from the sample after GaN capping, indicating a possible mechanism for spatial localisation of QDs.

A zoomed in CL-map of an area including a bright spot, and the emission spectrum corresponding to this spot are shown in figure 4.3. The CL map bright spot shown corresponds to emission including a quantum dot. This confirms the potential of using CL and SEM to spatially locate quantum dots. In order to spatially locate a single quantum dot with high resolution a surface pit could be used as an origin for a co-ordinate system to identify

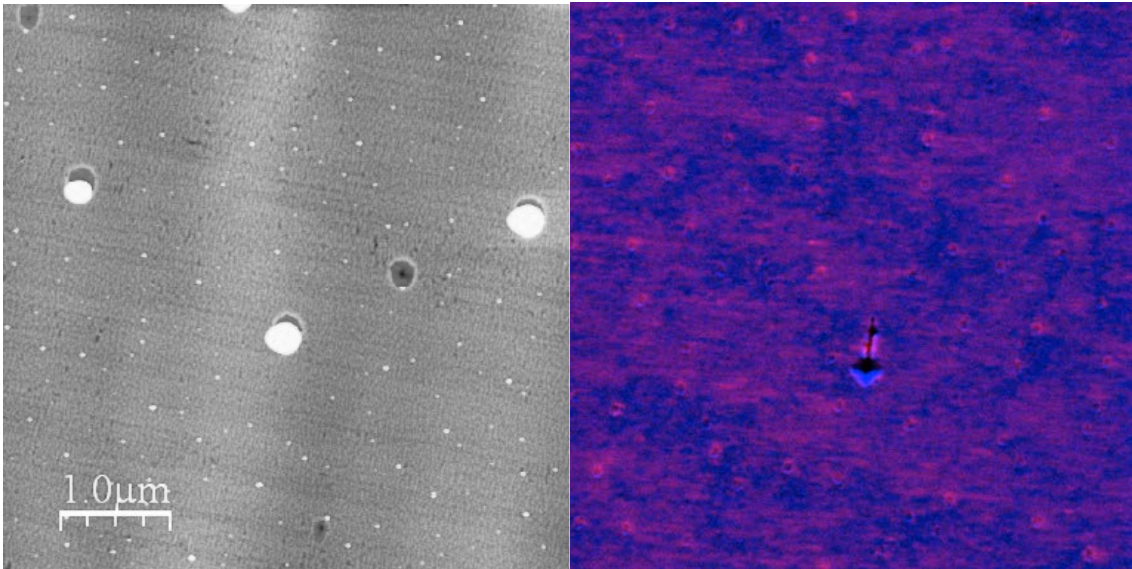


Figure 4.2: Left: AFM image showing formation of large indium droplets at surface pits in the InGaN epilayer after a N_2 anneal. Right: An overlay of an SEM image showing the surface pits with a CL map showing a link between the surface pits and bright spots in the CL.

a nearby quantum dot.

4.3 Initial micro-photoluminescence results

In this section the first μ -PL results on single non-polar InGaN quantum dots are presented. Many ~ 1 meV sharp emission lines characteristic of the exciton transition in a quantum dot can be found in μ -PL.

4.3.1 Exciton and Biexciton dynamics

In figure 4.4 we use the power-dependence of the intensity of two emission lines to identify an exciton-biexciton pair with a binding energy of -36 meV, comparable to values measured for c -plane QDs [72, 101]. The exciton luminescence intensity varies with the power according to $I(P) \propto P^x$ where $x = (1.9 \pm 0.1)$ in good agreement with the expected value $x = 2$ as described in section 2.4. The biexciton luminescence intensity varies with the excitation power as $I(P) \propto P^x$ with $x = (3.8 \pm 0.2)$ in good agreement with the expected

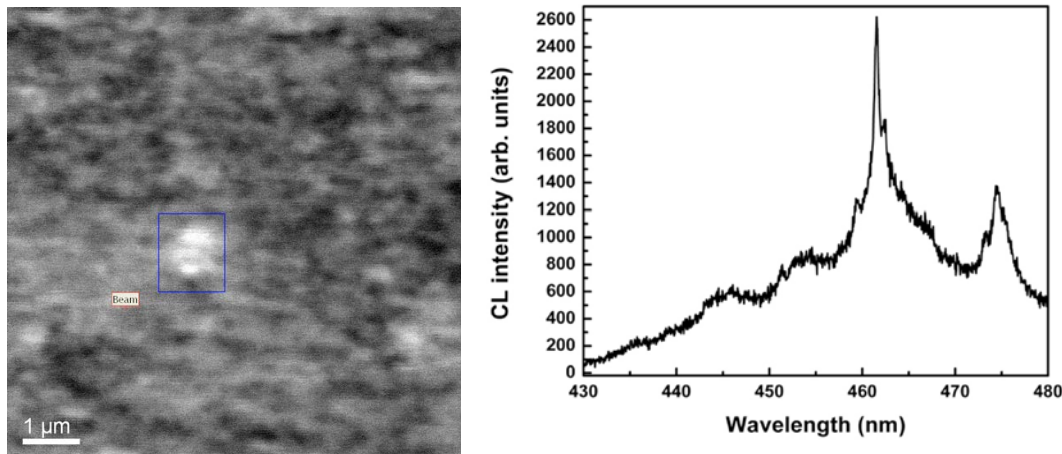


Figure 4.3: Left: High resolution CL-map of an area including a bright spot similar to that shown in figure 4.2. Right: Corresponding emission spectrum showing both quantum dot and quantum well emission.

value $x = 4$. The identification of an exciton-biexciton pair, as well as observation of sub-meV emission lines confirms the presence of quantum dots in the sample.

Time-resolved studies of the identified exciton-biexciton pair are summarised in figure 4.5. The exciton decay can be seen to be delayed slightly between the decay trace taken at 20 mW excitation power (with little to no population of the biexciton state), and the decay trace taken at 30 mW excitation power with a higher population of the biexciton state. The exciton lifetime, τ_x is relatively compared to typical values for these a -plane quantum dots (see section 4.3.2) at 972(3) ps. The biexciton lifetime, τ_{xx} is measured as 699(1) ps, giving a ratio $\frac{\tau_x}{\tau_{xx}} \approx 1.4$. For c -plane quantum dots, values of this ratio of ~ 1.8 [45], ~ 1.0 [102, 103] and ~ 0.7 [104] have been measured. The wide range is reflective of the dependence of this ratio on the quantum dot size and In content [105]. The perhaps intuitively expected ratio $\frac{\tau_x}{\tau_{xx}} = 2$ would be observed only for a quantum dot with both similarly strong vertical and lateral confinement. A value of ~ 1.4 has been estimated for a quantum dot with strong vertical confinement and an aspect ratio ~ 3 according to a simple model [106]. The exciton and biexciton decay dynamics presented here thus confirm the successful growth of non-polar InGaN quantum dots, as well as suggest the size for the particularly quantum dot studied is small, a fact which could contribute to the successful implementation of the coherent control scheme presented in chapter 6.

4.3. INITIAL MICRO-PHOTOLUMINESCENCE RESULTS

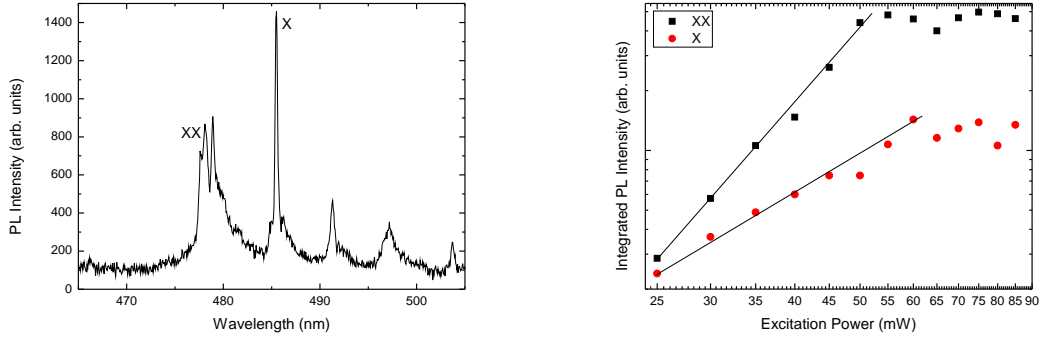


Figure 4.4: Left: Time-integrated micro-photoluminescence spectrum showing quantum dot emission lines - an exciton-biexciton pair is identified by studying their power dependence. A spatial map confirms that the unlabelled lines come from separate quantum dots. Right: Examining the power dependence of the emission lines labelled X and XX identifies the lines as an exciton-biexciton pair, the biexciton with a binding energy -36 meV.

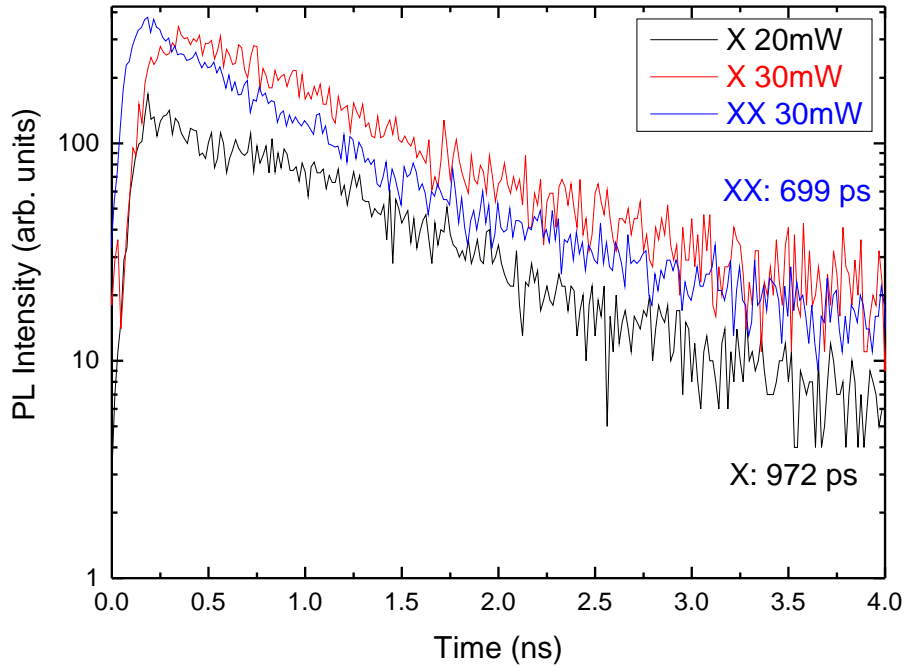


Figure 4.5: Time resolved photoluminescence performed on the exciton (X) and biexciton (XX) lines in figure 4.4. At low power, the exciton line decays with a lifetime of 972 ps. At higher power, a slight roll-off effect is observed as the biexciton state becomes populated. The biexciton lifetime is measured as 699 ps.

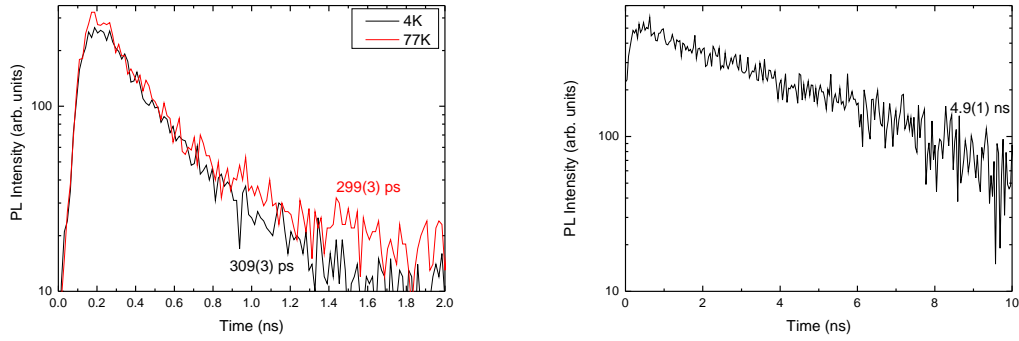


Figure 4.6: Left: Time resolved photoluminescence spectra from a single *a*-plane InGaN quantum dot. The measured lifetime is 309(3) ps at 4 K, and remains almost constant at higher temperatures, with a value of 299(3) ps at 77 K suggesting almost purely radiative decay. Right: Typical time resolved photoluminescence from a single *c*-plane quantum dot. The measured lifetime is 4.9(1) ns indicating a significantly smaller oscillator strength when compared to the measured *a*-plane quantum dot.

4.3.2 Internal field reduction

Although the time resolved photoluminescence presented in the previous section indicated an excitonic lifetime of 972(3) ps for the particular studied quantum dot, typical measured values in *a*-plane QD samples studied varied from 200 – 500 ps, compared with a variation observed in *c*-plane samples of 1 – 30 ns. This order of magnitude reduction in lifetime is indicative of an increased oscillator strength of the exciton transition caused by increased electron-hole overlap and thus a reduced internal field. In figure 4.6, excitonic time-resolved photoluminescence decay traces are presented for both an *a*-plane InGaN quantum dot and a *c*-plane InGaN quantum dot. The *a*-plane quantum dot exhibits a much reduced lifetime of 309(3) ps at a temperature of 4 K when compared with the *c*-plane excitonic lifetime of 4.9(1) ns. Furthermore, the lifetime of the *a*-plane InGaN quantum dot is relatively stable to increases in temperature, with a measured value of 299(3) ps at 77 K indicating the exciton decay at this temperature is almost purely radiative. The temperature dependence of the time-integrated photoluminescence from this quantum dot is examined in the next section.

4.3.3 Thermal stability of QD luminescence

The temperature evolution of an excitonic emission from a single *a*-plane QD is presented in figure 4.7. No significant broadening of the excitonic emission line is present up to 120 K. When the temperature dependence of the linewidth is compared to that of a *c*-plane quantum dot, it is clear that there is a reduction in the acoustic phonon coupling strength for the *a*-plane quantum dot. Given the reduced internal electric field concluded from the results of the previous section, this is perhaps indicative of a significant contribution to the total phonon coupling from the electric dipole in a *c*-plane quantum dot. This suggestion is in good agreement with recent theoretical studies on GaN quantum dots [107] which suggest piezoelectric coupling to transversal phonons provides a considerable contribution to the total acoustic phonon coupling. Previous results on temperature dependence of QD emission lines in *c*-plane InGaN quantum dots support the data presented for the *c*-plane quantum dot in figure 4.7 with significant line broadening observed above ~ 45 K [101, 108, 109].

4.4 Polarisation-resolved spectroscopy

Polarization control of single photons is important for quantum cryptography schemes based on entangled photon pairs [28] or linearly polarised photons [110]. In this section, the polarisation properties of *a*-plane quantum dots are presented, along with a comparison to their *c*-plane counterparts.

4.4.1 Linearly polarised emission

The first observation is that some quantum dot emission lines give 100% linearly polarised emission, as would be expected for the A-exciton (formed from an electron and a hole from the A-valence band) in an InGaN quantum well [111]. An example is given in figure 4.8. The axis of the linear polariser has been set to give the maximum quantum dot intensity at a polariser angle of 0° . With the polarisation axis orthogonal to that which obtains the maximum quantum dot intensity, the QD intensity reduces to zero within the noise measured on the CCD.

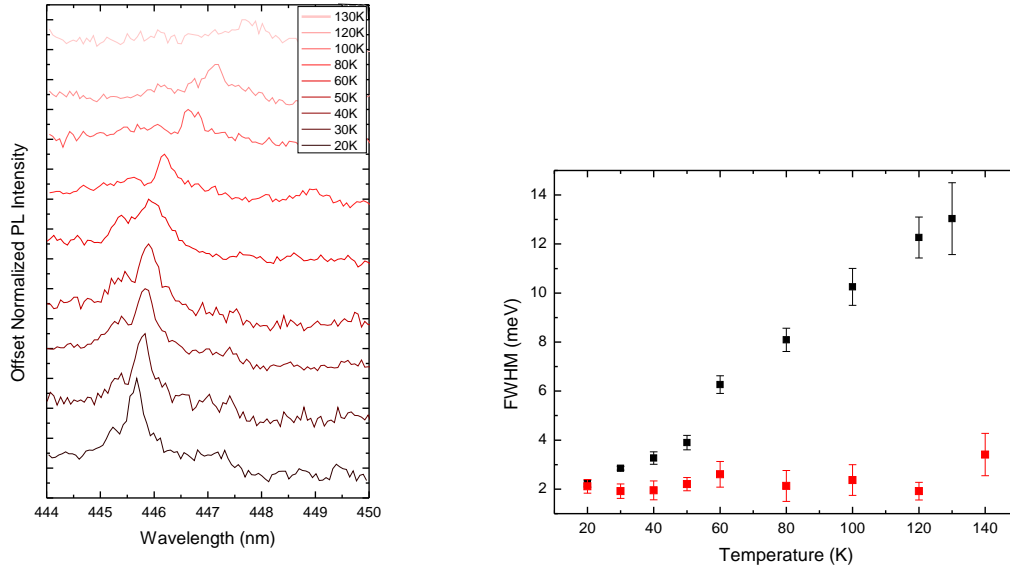


Figure 4.7: Left: Temperature evolution of an excitonic emission from a single a -plane InGaN quantum dot. A significant red-shift of the emission is seen after ~ 80 K but the emission linewidth appears unchanged. Right: Temperature evolution of the linewidth for a single a -plane InGaN QD emission (red) and a single c -plane InGaN QD emission (black). The a -plane QD linewidth stays almost constant while the c -plane QD linewidth increases significantly, suggesting a stronger acoustic phonon coupling in the c -plane case.

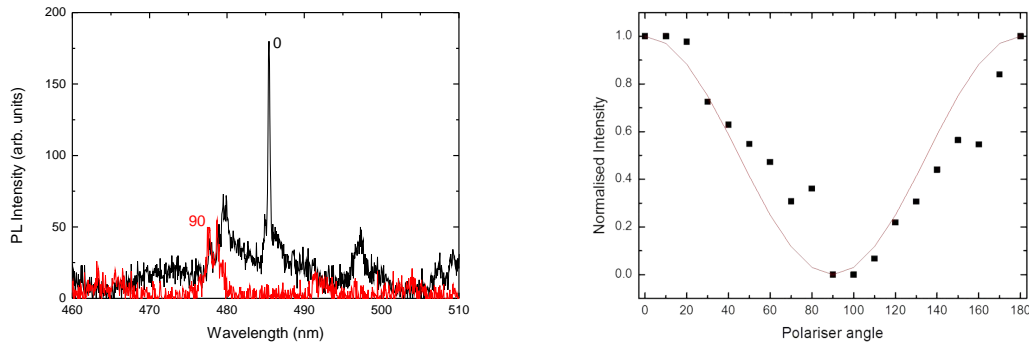


Figure 4.8: Left: Single quantum dot luminescence with two orthogonal polarisations axes selected for a linear polariser and half-wave plate combination in the optical path of the emitted PL. The quantum dot luminescence at ~ 486 nm has a minimum intensity of zero within the noise on the CCD at a polarisation axis 90° to its polarisation axis angle which gives the maximum intensity. Right: Plot of the quantum dot intensity against polariser angle. The measured data are the black points, while the red line corresponds to the expected Malus's law intensity dependence for a 100% linearly polarised emission.

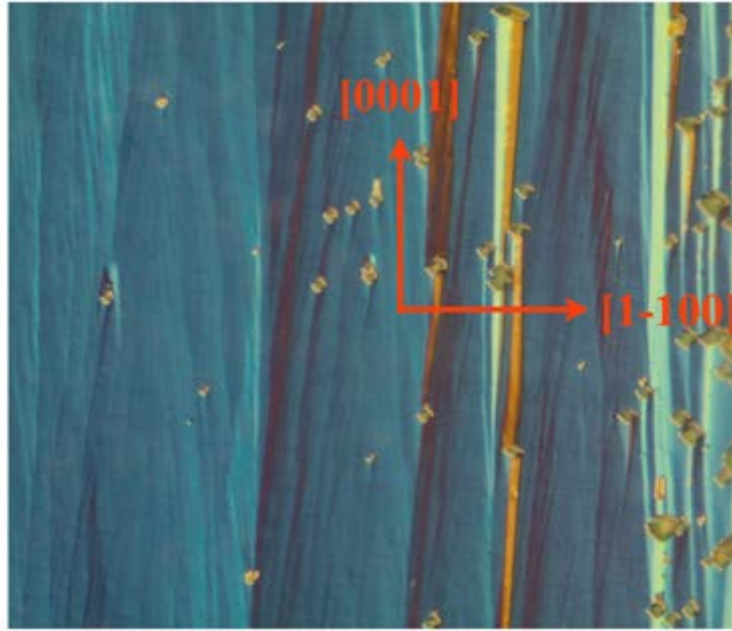


Figure 4.9: SEM image showing the crystallographic orientations of the a -plane InGaN quantum dot sample as measured by the grower. Surface striations pointing along the c -direction are large enough to be identified in the optical microscope which forms part of the μ -PL setup.

Figure 4.9 shows an SEM image of the surface of an a -plane InGaN quantum dot sample with the crystallographic directions as identified by the grower at the university of Cambridge. Large surface striations can be seen which point along or at very small angles to the c -direction. These striations can be identified in the optical microscope of the μ -PL setup, and thus can be used to relate the polarisation axis of the measurements in figure 4.8 to the crystal axes. All 100% linearly polarised quantum dot lines are found to have a polarisation axis pointing along the c -direction using this method.

I interpret the direction of the polarisation axis as follows: The polar nature of the c -direction in InN/GaN means that a quantum dot formed with the c -axis in the basal plane of quantum dot will be strained along that direction, leading to an asymmetry in the shape of the QD between the c - and m - crystal directions. The strain induced elongation along the c -direction means the exciton preferentially oscillates along this direction of so emits luminescence that is linearly polarised along this direction.

Figure 4.10 shows a comparison of the polarisation angles measured in our setup for a -

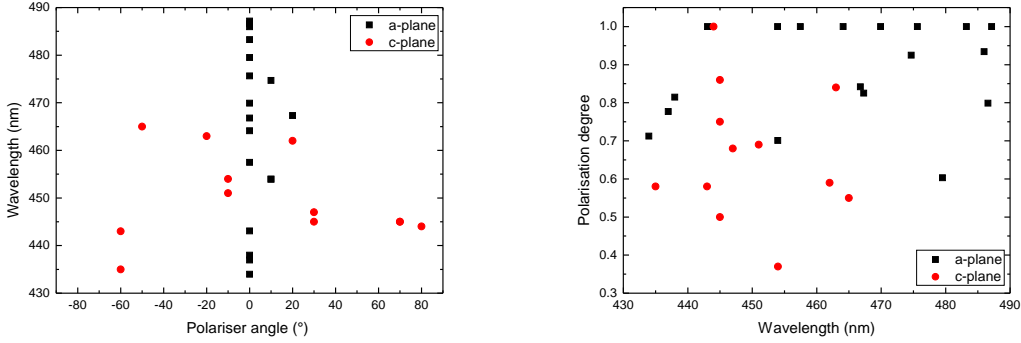


Figure 4.10: Left: Comparison of polariser angle corresponding to maximum intensity for *a*-plane and *c*-plane quantum dot emissions. In the *c*-plane case, a random distribution of angles is observed. The case of the *a*-plane quantum dot lines, are all polarised between 0° and 20° polariser angle. A polariser angle of 0° corresponds to a polarisation axis pointing along the *c*-direction as measured using the surface striations visible in the optical microscope. Right: Comparison of polarisation degree for *a*-plane and *c*-plane quantum dot emissions. No dependence on the wavelength is observed, with *a*-plane quantum dot lines frequently exhibiting a polarisation degree of 1.

plane and *c*-plane quantum dot lines, with the two samples placed side-by-side in the cryostat. For the *a*-plane quantum dot sample, we can use the surface striations shown in figure 4.9 to identify a polariser angle of 0° with a polarisation axis along the *c* crystal direction. The polariser angles for the *c*-plane sample were not related to crystallographic axes since distribution of angles is random. The polarisation degree, P_d is defined by:

$$P_d = \frac{I_{\max} - I_{\min}}{I_{\max} + I_{\min}}, \quad (4.1)$$

where I_{\max} and I_{\min} are the maximum and minimum intensities of quantum dot luminescence as it varies with polariser angle. The distribution of the polarisation degree with wavelength is seen to be random in both the *c*-plane and *a*-plane cases, with a value $P_d = 1$ frequently observed for *a*-plane quantum dot emissions. The *a*-plane results are interpreted as the strain-induced elongation of the quantum dot along the *c*-direction causing a modification in the symmetry of the quantum dot confinement potential.

For the *c*-plane quantum dots, the presence of maxima at certain polarisation angles also indicates a confinement potential which is not spherically symmetric (for which circularly

polarised emission would be expected). In this case, the random distribution of the indium atoms in the quantum dot is responsible for the modification of the confinement potential. This explanation fits well with the observed random distribution of polarisation degrees: Since the measurement geometry of our setup only allows access to polarisation axes corresponding to in-plane crystal directions, only a quantum dot with an in-plane asymmetry in confinement potential will emit linearly polarised light with a polarisation degree of 1. For a quantum dot with an asymmetry in indium content in an out of plane direction, the measured orthogonal polarisations of the emitted light do not correspond to the preferred crystal direction of oscillation for the exciton, but rather the component of this in the surface plane. Therefore, in the c -plane case we can expect a polarisation degree less than unity unless the indium content of the quantum dot happens to be distributed in such a way that the confinement potential has an in-plane asymmetry and very small deviations from spherical symmetry in other directions. We can see that of the 10 measured quantum dot lines for the c -plane quantum dot sample, this was the case for one quantum dot.

Recalling section 2.3.1, we know the expected valence band symmetries for c -plane bulk InN/GaN are p_x - and p_y -like for the A and B bands, and p_z -like for the C-band. It is important to take the symmetries of the quantum dot hole states into account when discussing the effect of strain on the polarisation [112, 113, 114], for m -plane InGaN quantum wells it is found that two orthogonal polarisation axes produces different energy emissions [115, 116] suggesting different excitons have different polarisation degrees. Theoretical calculation predict a switching of the energy order of the valence bands for m -plane InGaN quantum wells [117].

For a -plane InGaN quantum wells it is found both theroretically [118] and experimentally [119] that the ground state A-exciton has a strong linear polarisation, as is the case for a -plane bulk GaN [120]. Therefore, it is possible that the QD lines found with 100% linear polarisation are those formed with A-like holes states, while those lines with a polarisation degree $P_d < 1$ are formed from B-like and C-like hole states. An alternative explanation for the existence of quantum dot lines with $P_d < 1$ in the a -plane quantum dot sample is that they originate from quantum dots whose indium content is distributed in such a way

as to induce an out-of-plane asymmetry in the confinement potential in addition to the in-plane asymmetry associated with the strain along the c -direction.

The results presented here for c -plane InGaN polarisation degree and angle agree with results from GaN quantum dots [73, 121] where random polarisation degrees were observed with polarisation axes which did not necessarily correspond to crystallographic directions. The results for polarisation degree and angle presented here for a -plane quantum dots are much more useful from a quantum cryptography perspective, where total polarisation control of a single photon would be very useful. The presented exciton and biexciton dynamics strongly indicate the formation of a -plane quantum dots, and the polarisation studies reveal lines with a linear polarisation with polarisation degree of unity. However, in order to evaluate the potential of these quantum dots in quantum cryptography, a confirmation of the single photon nature of the emission via a *Hanbury-Brown and Twiss* (HBT) type experiment [122] should be performed. The confirmation of the single photon nature of c -plane InGaN quantum dots via HBT [47] necessitated the use of a distributed Bragg reflector (DBR) cavity to enhance light extraction. Although the luminescence from the a -plane quantum dots is found to be brighter on-average than typical c -plane samples, a DBR cavity structure is still required to perform an HBT experiment, and this will be investigated in the near future. The observation of Rabi rotations in chapter 6 do indicate the discrete nature of the optical transitions in this quantum dots though, so it is reasonable to expect single photon emission would be confirmed by such an experiment. If so, this would represent the first observation of 100% linearly polarised single photon emission from a quantum dot, with previous schemes in c -plane InGaN showing $\sim 90\%$ linear polarisation along the c -direction in a InGaN quantum dot at the apex of a nanopillar grown along the c -direction [123] and $\sim 70\%$ linear polarisation achieved for InGaN quantum dots in an AlGaIn nanowire with the polarisation axis along the nanowire direction [52].

4.4.2 Fine Structure Splitting

In section 2.4, we saw that the doubly-degenerate bright-exciton state in a spherically symmetric quantum dot is split into two states with orthogonal linear polarisations when

asymmetry in shape or indium content in the quantum dot is considered, with the splitting referred to as the fine structure splitting. For the quantum dot lines observed with a linear polarisation with $P_d < 1$ we can expect that this splitting may be resolvable. The resolution of the fine structure splitting is technically difficult in our samples due to the spectral diffusion effect described in the next chapter. However, values for the fine structure splitting can be obtained for quantum dot lines with $P_d < 1$ as seen in figure 4.11. To differentiate any fine structure splitting with spectral drifts over time as described in the next chapter, the fine structure splitting was derived from the average quantum dot energy over 300 s for each of the orthogonal polariser angles. Confirmation that the measured splitting indeed originates from the fine structure and not spectral diffusion comes from the fact that the brighter emission line is always measured to be at a lower energy than the minimum intensity emission line as shown in figure 4.11. Fine structure splittings ranging from 250 – 500 μeV are measured for 5 quantum dot lines. These values are compared to values of the fine structure splitting measured for *c*-plane InGaN quantum dots [124]. Measurement of the *c*-plane InGaN quantum dot fine structure splitting was not possible to resolve in our setup geometry, with both horizontal and vertical excitation required in the *c*-plane case [72] since the polarisation of photons emitted by a quantum dot is not likely to correspond to an in-plane crystal direction. The small values of the fine structure splitting obtained here are perhaps surprising given that they are similar in magnitude to that measured for strained bulk GaN [125, 126] while quantum confinement is predicted to increase the fine structure splitting [127]. The plot of fine structure splitting against wavelength for 5 measured quantum dot emissions in figure 4.11 does not contradict the expected random distribution of the fine structure splitting with quantum dot emission energy due to the effect of both size and indium composition on the exciton fine structure.

4.5 Chapter summary

The first $\mu\text{-PL}$ results from InGaN quantum dots grown on a non-polar plane have been presented. A large increase in the oscillator strength of the ground state exciton transition is observed compared to *c*-plane InGaN quantum dots. An exciton-biexciton pair has been identified by studying the power dependence of the luminescence and the decay dynamics

studied. A strained-induced elongation of the quantum dots along the c -direction of the crystal gives rise to 100% linearly polarised emission from many quantum dots. Some quantum dot emissions have a polarisation degree less than unity, and for these a fine structure splitting between $250 - 500 \mu\text{eV}$ can be resolved.

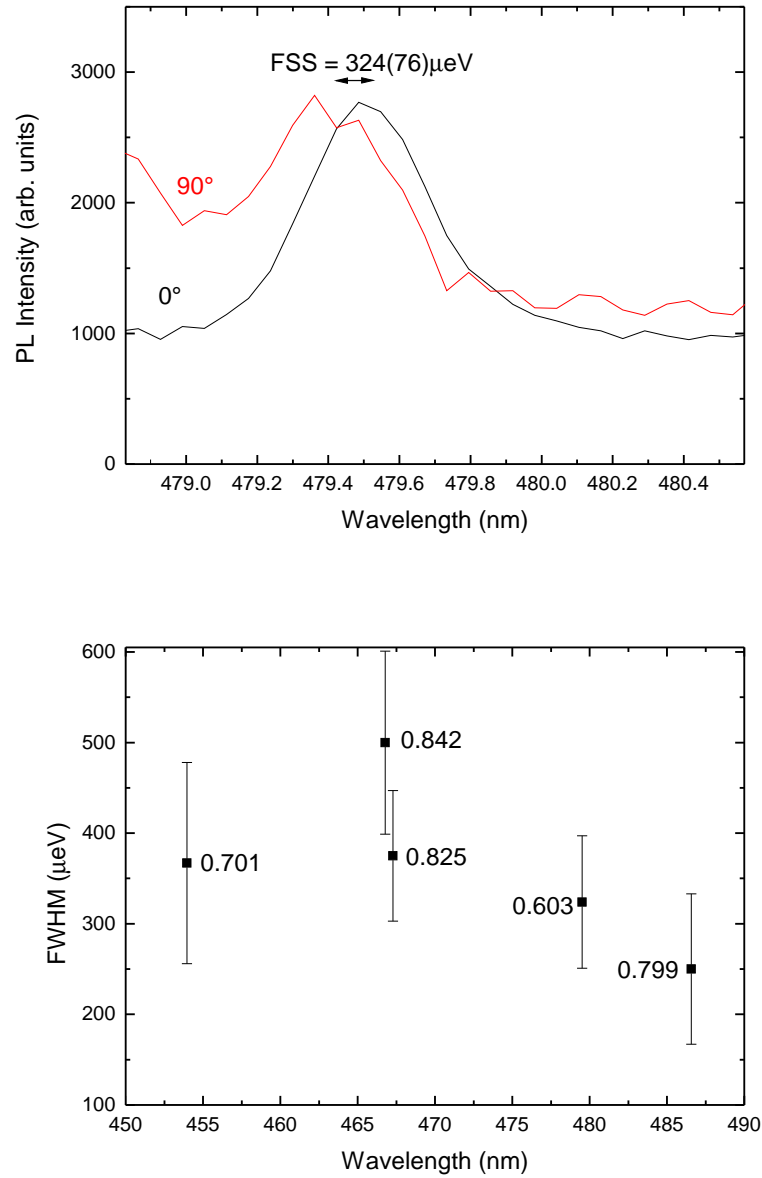


Figure 4.11: Left: Two orthogonal linear polarisations of emitted PL from a single InGaN quantum dot. The fine structure splitting between the two lines is resolvable, in this case with a value $(324 \pm 73) \mu\text{eV}$. The red 90° spectrum is enlarged by a factor of 9. Right: Measured fine structure splittings plotted against wavelength for 5 quantum dot lines. The polarisation degree P_d for each quantum dot line is written next to its data point.

Origins of spectral diffusion in InGaN QDs

5.1 Introduction

The phenomenon of spectral diffusion, small changes in emission energy over time, has been previously observed in InGaN quantum dots [54] as well as other QD types [128, 129] and attributed to fluctuating charges in the local environment of a single quantum dot [130]. The presence of these $\sim 250 - 400 \mu\text{eV}$ [131] shifts in the QD energy is severely detrimental to the possibility of achieving either the Purcell effect or strong coupling between an InGaN quantum dot and an optical microcavity. In this chapter, we attempt to elucidate the origins of spectral diffusion in InGaN quantum dots via a statistical analysis across samples with differing dislocation densities. Furthermore, we investigate the effect of the inclusion of a Si-doped buffer layer adjacent to the InGaN quantum dot layer to model the effect of a general n-type electrically active impurity on spectral diffusion. Finally, we use spectral diffusion measurements on *a*-plane InGaN QDs to motivate an estimate of the internal electric field in *a*-plane InGaN QDs.

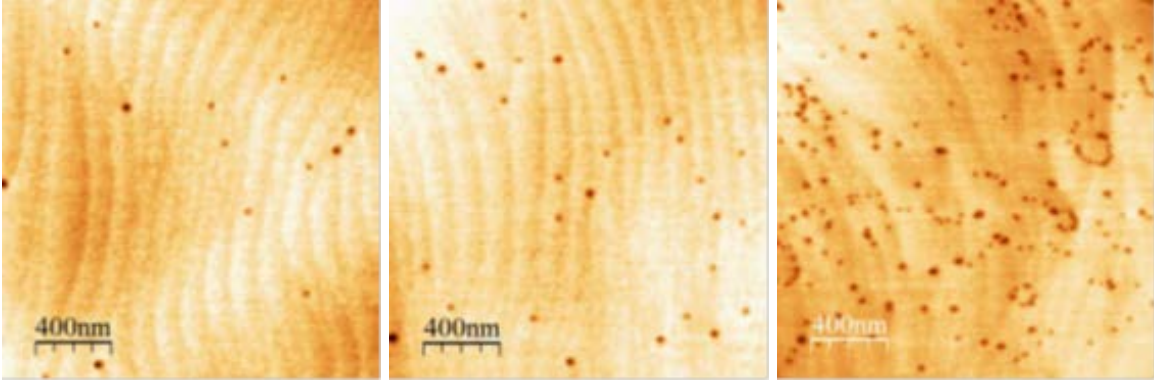


Figure 5.1: AFM images of three GaN epilayers with differing densities of threading dislocations taken at the University of Cambridge. From left to right: Low $(3.08 \pm 0.31) \times 10^8 \text{ cm}^{-2}$, medium $(6.15 \pm 0.47) \times 10^8 \text{ cm}^{-2}$ and high $(5.36 \pm 0.30) \times 10^9 \text{ cm}^{-2}$ dislocation densities. The dark dots are surface pits associated with the formation of edge, screw or mixed dislocation types.

5.2 Effects of dislocation density on spectral diffusion

5.2.1 Sample growth and preparation

Three samples were grown at the University of Cambridge with differing dislocation densities. Firstly, three GaN epilayers with threading dislocation densities were grown in a Thomas Swan close-coupled showerhead reactor on Al_2O_3 (0001) substrates. The first, which we term low dislocation density (LDD) has threading dislocation density $(3.08 \pm 0.31) \times 10^8 \text{ cm}^{-2}$. The second, medium dislocation density (MDD) has a threading dislocation density of $(6.15 \pm 0.47) \times 10^8 \text{ cm}^{-2}$. The third, high dislocation density (HDD) sample has a threading dislocation density of $(5.36 \pm 0.30) \times 10^9 \text{ cm}^{-2}$. These threading dislocation densities were determined by atomic force microscopy (AFM) on epilayers threated with a post-growth SiH_4 flux in the MOCVD growth reactor to increase surface pit sizes associated with edge dislocations, as described in [132]. Example AFMs of the three GaN epilayers are shown in figure 5.1.

The differing dislocation densities were achieving by differing growth methods for GaN, 2D growth resulting in a high dislocation density [77]. Lowering the V:III ratio can produce initial island growth [133], subsequent ramping back up of the V:III ratio causes the islands to coalesce, this 3D-2D growth can produce films with a low dislocation density.

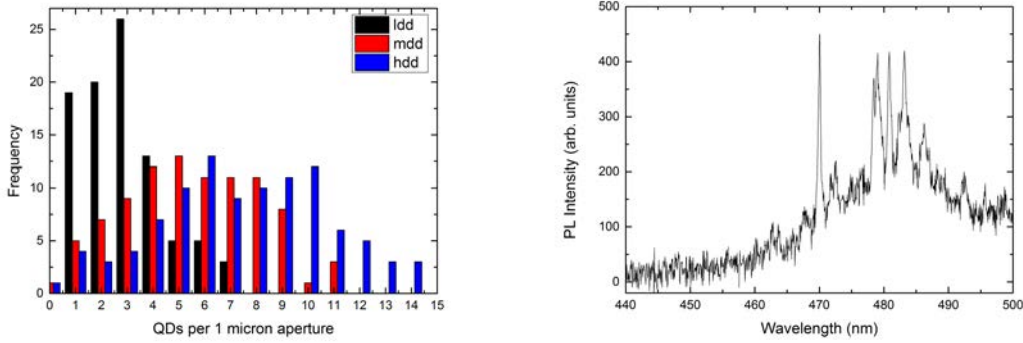


Figure 5.2: Left: Histogram of observed qd emission lines per 1 μm aperture in three InGaN QD samples with differing dislocation densities taken over 100 apertures. Right: Example μ -PL spectrum showing 5 QD emission lines.

Each of the GaN epilayers then acts as a pseudo-substrate for the growth of InGaN epilayers of ~ 2.5 nm thickness. The modified droplet epitaxy approach described in section 2.5 was employed to form InGaN quantum dots.

5.3 Estimation of QD density

In order to assess the effect of dislocation density on the formation of InGaN quantum dots, I performed an estimate of the quantum dot density for each of the samples described in the previous section. Samples were masked in Au with 1 μm apertures defined according to the methods outlined in section 3.5.1. As a rough metric for quantum dot density, I used the number of excitonic lines observed per 1 μm aperture in micro-PL. While it's true that one quantum dot can produce multiple emission lines, this metric is consistent between the three different samples. My findings are summarised in figure 5.2.

We can see that the quantum dot density appears to increase with the dislocation density, suggesting threading dislocations play a role in the formation of InGaN quantum dots by modified droplet epitaxy. For the LDD and MDD samples, the values for the metric for quantum dot density were similar to the dislocation densities, at $3.4 \times 10^8 \text{ cm}^{-2}$ for the LDD sample, and $6.4 \times 10^8 \text{ cm}^{-2}$ for the MDD sample. For the HDD sample the metric was measured at $9.5 \times 10^8 \text{ cm}^{-2}$, lower than but comparable to the threading dislocation density. It should be noted that the atomic force microscopy measurements of uncapped

InGaN epilayers suggest that the number of metallic nanostructures formed by the anneal step in the growth procedure is unaffected by the dislocation density. This does not however, imply that dislocations do not play a role in the quantum dot formation during the GaN capping process.

5.4 Temporal variation in QD luminescence

In order to investigate temporal variations in the QD emission, I collected consecutive 5 s μ -PL spectra from single InGaN QDs over time periods of several hundred seconds. The length of this time-scale was limited by sample drift, typical positional changes for a single QD are of the order of 1 μ m with a period of 10 minutes. For all the measurements presented in this section, I used a constant two photon excitation power density of 1 MWcm⁻². This excitation power was selected to provide an estimated carrier density of one neutral exciton per quantum dot, since biexcitonic emission is typically observed above 3 MWcm⁻² in similiarly grown InGaN QD samples [48]. A constant power was used so to decouple any increase of spectral diffusion with excitation power [134, 135] from our results. Some example repeat 5 s accumulation spectra are shown in figure 5.3.

We can see from figure 5.3 that some spectra show clear shifts in the QD emission energy over time. Some shifts appear to be sudden “hops” in the energy and others more gradual changes. In order to assess whether the origin of these energy shifts is related to threading dislocations, I had to decide on a suitable metric to characterise the magnitude of spectral diffusion over a certain time-scale. Three metrics were proposed, *standard deviation* of quantum dot energy over the measurement time-scale (several hundred seconds), *mean maximal deviation* over 100 s, and “*hops*” per 100 s where a hop was defined as a change of more than 0.25 meV in the quantum dot energy over 5 s. Consecutive 5 s spectra were collected for 10 quantum dots in each of the samples with differing dislocation density.

Firstly, in figure 5.4 we see that the “*hops*” metric and the *mean maximal deviation* metric both agree well with the *standard deviation* metric. I interpret this to mean each of the three metrics represents a reasonable characterisation of the magnitude of spectral diffusion.

5.4. TEMPORAL VARIATION IN QD LUMINESCENCE

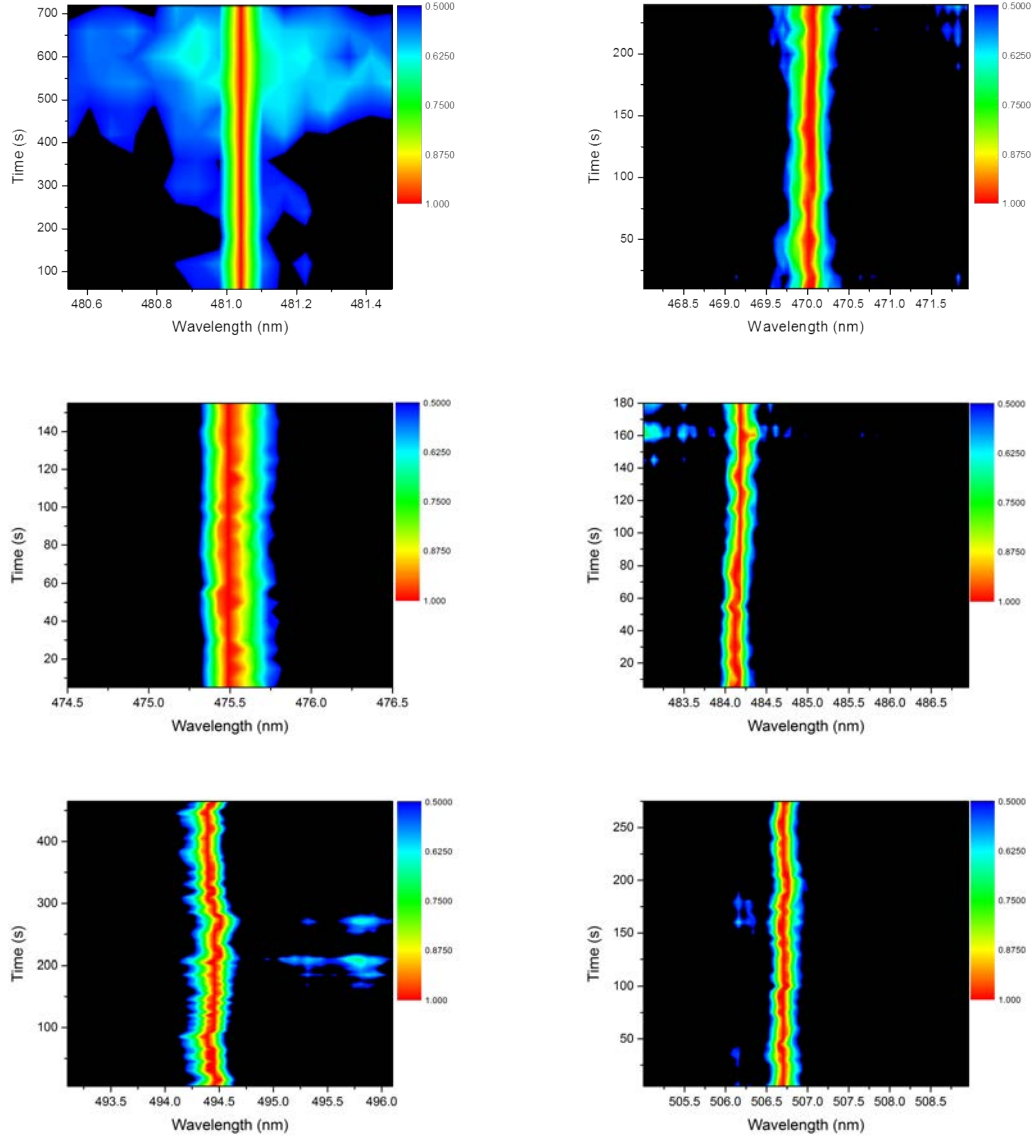


Figure 5.3: Example of repeat 5 s accumulation μ -PL spectra on various InGaN quantum dots. Normalised PL intensity is shown in colour on a scale from 0.5 – 1 so as to track changes in the quantum dot energies and full width half maxima. Top: Two sets of spectra from quantum dots in the LDD sample. Middle: Two sets of spectra from quantum dots in the MDD sample. Bottom: Two sets of spectra from quantum dots in the HDD sample - here we can clearly see large shifts in the quantum dot energy over time.

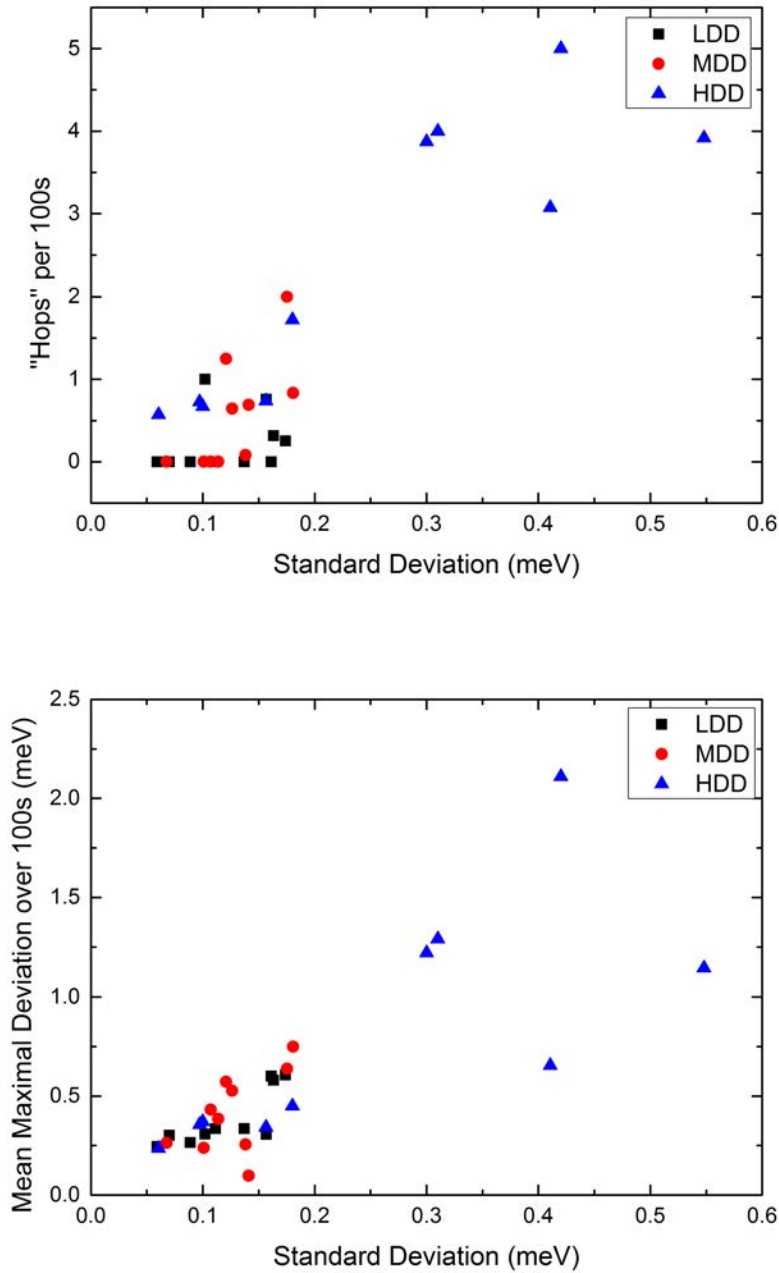


Figure 5.4: Two plots comparing metrics designed to characterise the magnitude of spectral diffusion in InGaN quantum dot samples. Consecutive 5s spectra were collected for several hundred seconds for 10 quantum dots for each of the low, medium and high dislocation density samples. Top: Comparison of “hops” (energy changes > 0.25 meV) metric and standard deviation of quantum dot energy. Bottom: Comparison of mean maximal deviation over 100s metric with standard deviation of quantum dot energy. We can see both the “hops” and mean maximal deviation metrics relate linearly to the standard deviation, suggesting each of the metrics represent a reasonable characterisation of the magnitude of spectral diffusion.

Given the agreement of the three metrics, we will focus on the results of the *standard deviation* metric to interpret the results of the consecutive spectra collected for quantum dots in each sample. Figure 5.5 shows the standard deviation of quantum dot energy plotted against wavelength and linewidth of QD emission. Wavelength and linewidth were determined from fitting the QD emission lines to Lorentzian lineshapes, and extracting the centre wavelength, and full width at half maximum respectively.

The mean value of standard deviation of QD energy for the each of the three samples are as follows, (0.26 ± 0.05) meV for the HDD sample, (0.13 ± 0.01) meV for the MDD sample, and (0.12 ± 0.01) meV for the LDD sample. A student's t-test performed on the data set shows a statistically significant difference in the standard deviations between the HDD and LDD ($p < 0.03$) and between the HDD and MDD ($p < 0.04$) samples. For completeness, the results of the "hops" metric are presented in figure 5.6. The same conclusions as for the standard deviation metric in figure 5.5 can be drawn.

The observed correlation between dislocation density and magnitude of spectral diffusion leads us to suggest that spectral diffusion on a time-scale of seconds is linked to threading dislocations. Since the commonly accepted explanation for spectral diffusion is of fluctuating charges in the vicinity of the quantum dot [54, 135] this can be expected - the dislocation acts as a local trap for a carrier and the electric field created by the trapped carrier changes the total electric field in the quantum dot, and thus the emission energy via the quantum confined stark effect. The observed correlations between quantum dot density and dislocation density, and between spectral diffusion and dislocation density seem at odds with each other, particularly for laser applications. This lead, in collaboration with the University of Cambridge, to investigating other approaches to increase the quantum dot density. Growth of multiple quantum dot layers was successful in increasing dot density without detracting from the quality of the emission lines [136] and indeed these multi-layer structures have found success in lasing applications [137].

The correlation between QD linewidth and spectral diffusion present for the LDD and MDD samples (as seen in figure 5.5) suggests a second mechanism for spectral diffusion which is not linked to dislocations. Since this correlation is not present for the

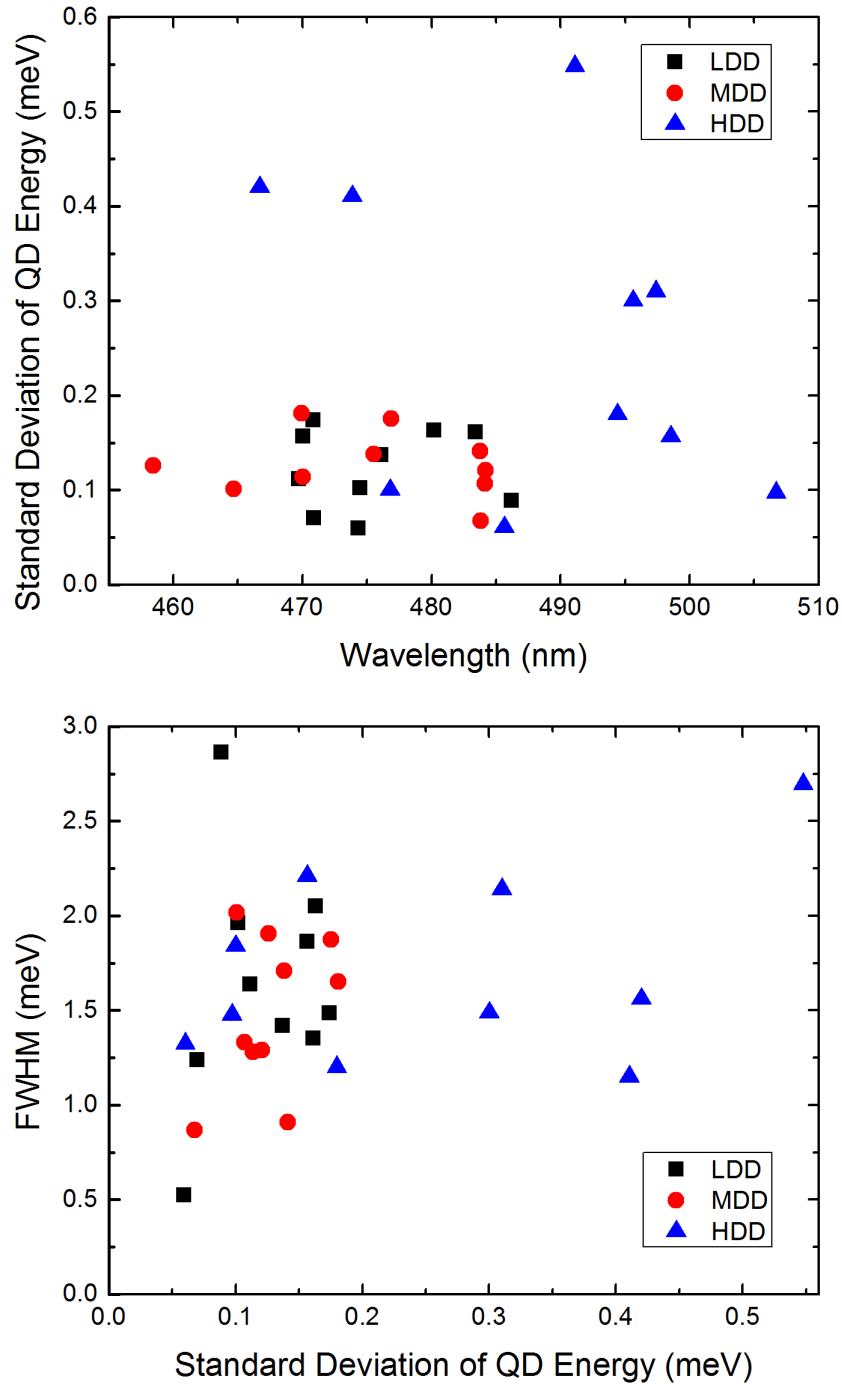


Figure 5.5: Top: Standard deviation of QD energy plotted against wavelength for 30 quantum dots, 10 from each of the low, medium and high dislocation density samples. No correlation is apparent between wavelength and standard deviation, but the HDD sample seems more likely to suffer from high standard deviations. Bottom: Full width at half maximum of Lorentzian fit of quantum dot emission line for each of the 30 quantum dots. The HDD samples exhibiting high values of the standard deviation appear to have randomly distributed linewidths. For the rest of the quantum dots, the linewidth correlates linearly with the standard deviation.

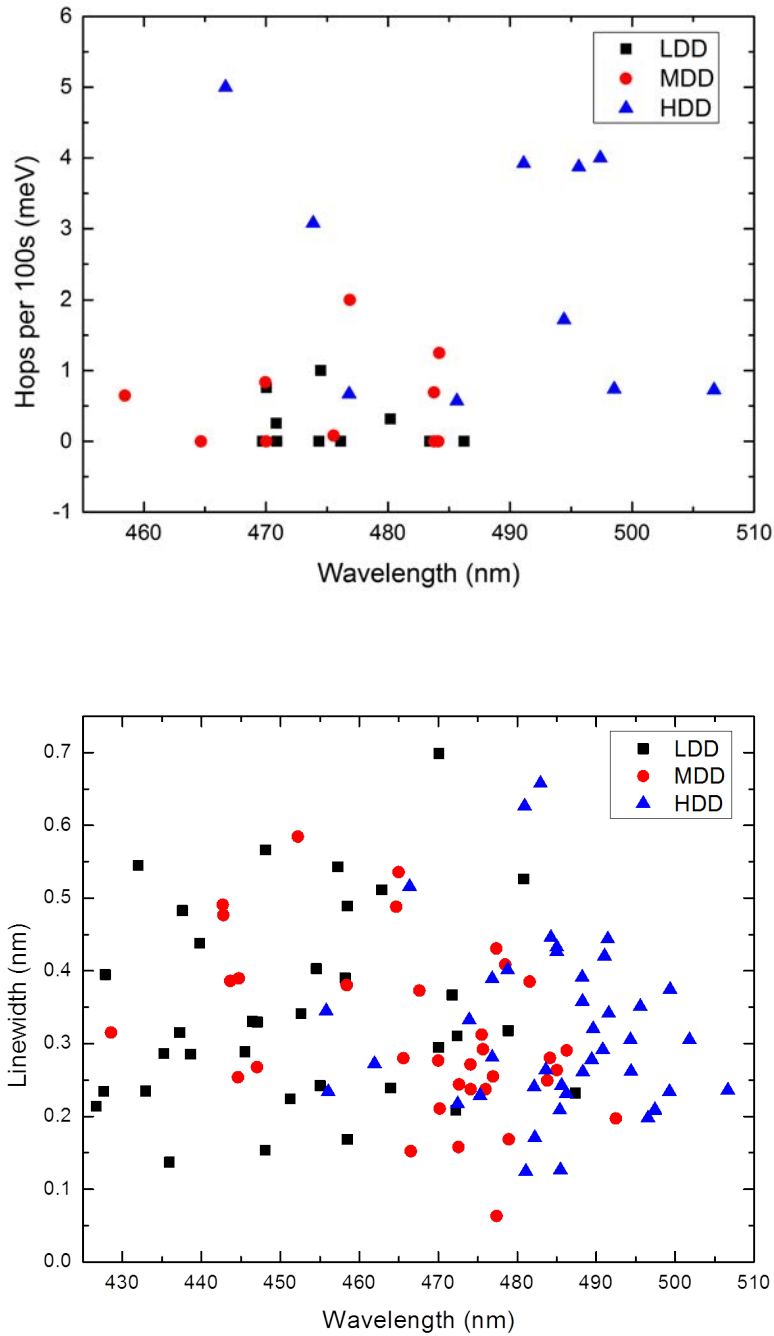


Figure 5.6: Top: “Hops” metric against wavelength for each of the 10 quantum dots in each sample, no correlation between the “hop” metric and wavelength is apparent, but the HDD sample clearly has more instances of a high number of “hops” in QD energy. Bottom: Linewidth (measured as full width at half maxima of QD emission fitted to a Lorentzian) against wavelength for 30 quantum dots for each of the LDD, MDD and HDD samples. No correlation between linewidth and wavelength, or linewidth and dislocation density exists.

HDD sample, we can conclude that the second mechanism gives rise to a smaller magnitude of spectral diffusion than the dislocation-mediated spectral diffusion. Figure 5.6 shows linewidths for 30 quantum dots in each of the LDD, MDD and HDD samples. The linewidth is measured as full width at half maximum of the quantum dot emission line fitted to a Lorentzian. No correlation between linewidth and wavelength, or linewidth and dislocation density can be seen, providing further support for a second mechanism of spectral diffusion. Since this mechanism not only changes the energy of the quantum dot emission, but also increases its linewidth, the time-scale for this mechanism must be much faster than the accumulation time of 1 – 5 s.

So far, two mechanisms for spectral diffusion have been proposed: The first takes place on slow time-scales \sim seconds, and is linked to charge carriers trapped at threading dislocation sites; The second, which is independent of threading dislocation density, takes place at time-scales much faster than 1 s, and can therefore not only induce changes in the quantum dot emission energy but also the linewidth as observed over 1 – 5 s accumulation times. These mechanisms for spectral diffusion are described in more detail below.

5.4.1 Fast time-scale spectral diffusion

I attribute spectral diffusion on time-scales much faster than the accumulation time to both itinerant charge carriers in the underlying quantum well layer, and charge carriers trapped in weakly-localised states in the quantum well formed by spatial fluctuation of the quantum well potential level. A charge carrier itinerant or trapped in the quantum well in the vicinity of the quantum dot will cause a point charge electric field, which adds vectorially to the internal electric field in the quantum dot. This change in the total electric field through the quantum dot will cause a change in the quantum confined Stark effect as given by equation 2.6. Since these changes in energy can take place much faster than the accumulation time used to measure quantum dot spectra, this fast time-scale spectral diffusion also increases the observed linewidth of the quantum dot. On rare occasions linewidths below the resolution limit of our μ -PL setup can be observed, as shown for a quantum dot from a multilayer quantum dot sample in figure 5.7. Here the quantum dot linewidth is less than the resolution limit of $\sim 380 \mu\text{eV}$ at $\sim 480 \text{ nm}$. Similarly, we can

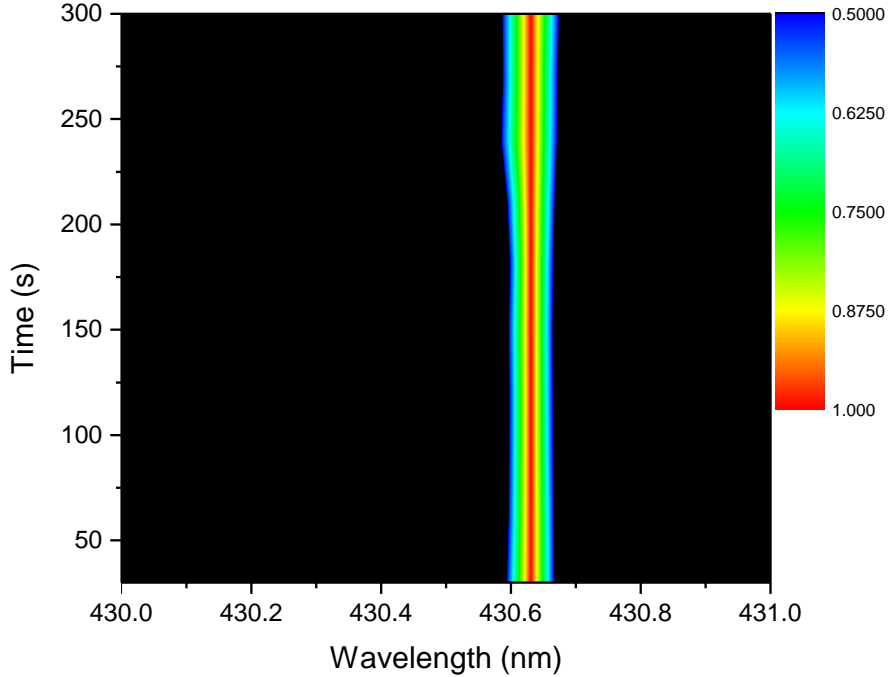


Figure 5.7: Time evolution of a resolution limited quantum dot emission line with wavelength over 300s, with intensity shown in colour. Any spectral diffusion taking place causes shifts less than the resolution limit ($380 \mu\text{eV}$).

conclude that any spectral diffusion taking place is also on an energy scale $< 380 \mu\text{eV}$. However, a typical linewidth for an InGaN quantum dot is $\sim 1 \text{ meV}$, an order of magnitude higher than that observed for InAs quantum dots [138]. We can attribute this difference to fast time-scale spectral diffusion.

5.4.2 Slow time-scale spectral diffusion

For the slow time-scale spectral diffusion, this can be attributed to charge carriers trapped at threading dislocation sites. These carriers will also modify the quantum confined Stark shift by the same mechanism as any itinerant or trapped carriers in the quantum well. A typical trapping time-scale for a carrier at a dislocation site τ can be expressed as:

$$\tau = \tau_{\text{ph}} \exp\left(\frac{E_{\text{trap}}}{k_B T}\right), \quad (5.1)$$

where τ_{ph} is the phonon scattering time and E_{trap} is the depth of the trap potential. For dislocation traps, this corresponds to time-scales of \sim seconds [128], consistent with my results. So far, we have concluded that reducing dislocation density is an important step towards optoelectronic applications of InGaN quantum dots, since it should reduce (but not eliminate due to the second fast time-scale mechanism mediated by the quantum well) the spectral diffusion. We have also observed that multilayers of quantum dots as grown in [136] are a practical way to realise applications requiring a high quantum dot density. However, the simple mechanism of a carrier trapped at a dislocation site proposed for slow time-scale spectral diffusion suggest other forms of defects could cause spectral diffusion by a similar mechanism. For this reason, samples incorporating deliberate silicon doping were grown at the University of Cambridge. By introducing Si doping into a layer adjacent to the the quantum dot layer, we aimed to asses the effect of an electrically active impurity (i.e. dopant) on spectral diffusion.

5.4.3 Effect of electrically active impurities on spectral diffusion

Two samples with Si doping levels of $\sim 1 \times 10^{18} \text{ cm}^{-3}$ and $\sim 5 \times 10^{17} \text{ cm}^{-3}$ and a third unintentionally doped sample were grown at the University of Cambridge by a modified droplet epitaxy scheme. LDD GaN pseudo substrates were overgrown with Si doped GaN, before growth of the InGaN epilayer. The N_2 anneal and capping layer growth steps were the same as described in section 5.2.1. All samples were masked according to the same scheme described in section 5.3.

A typical result from the undoped sample is presented in figure 5.8. The observed magnitudes of spectral diffusion are very similar to those of the previously studied LDD sample. The presented QD spectra has a narrow linewidth ($\sim 800\mu\text{eV}$) but this is not limited by the spectral resolution of our setup, and the typical linewidths of $\sim 1 \text{ meV}$ again indicate the presence of fast time-scale spectral diffusion from the quantum well.

The sample with a Si doping level of $\sim 1 \times 10^{18} \text{ cm}^{-3}$ did not show any typical quantum dot $\mu\text{-PL}$, with only emission from the quantum well present. A typical result from the sample with a Si doping level of $\sim 5 \times 10^{17} \text{ cm}^{-3}$ is shown in figure 5.9. The most striking difference between this sample and those previously studied is the diminished ratio

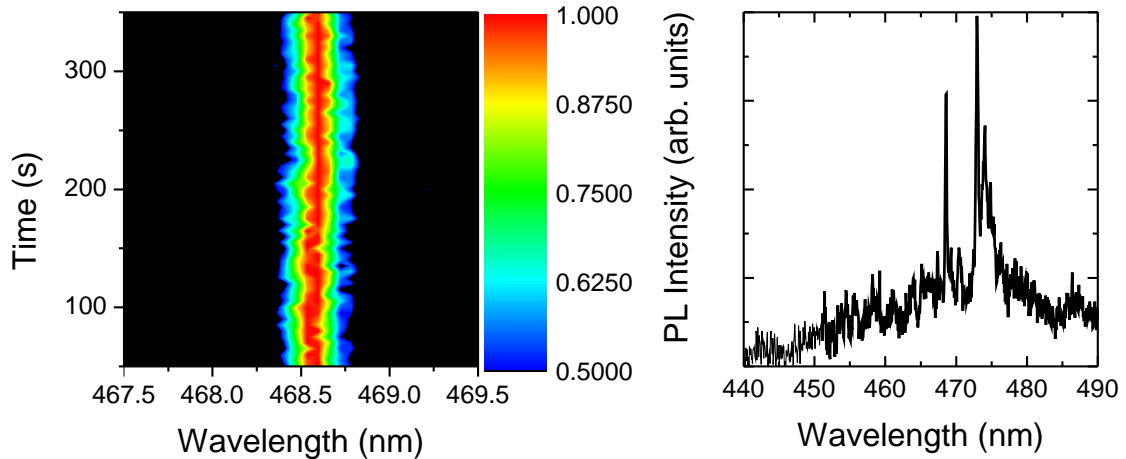


Figure 5.8: Time evolution of a resolution limited quantum dot emission line with wavelength over 300 s, with intensity shown in colour. Any spectral diffusion taking place causes shifts less than the resolution limit ($380 \mu\text{eV}$).

between QD and QW luminescence intensities. The small QD:QW luminescence intensity ratio made it difficult to perform a systematic studies on quantum dots in the Si-doped sample. However, all studied dots exhibited both magnitudes of spectral diffusion (as measured by the three metrics described above) and linewidths very similar to those in the LDD sample, suggesting the presence of an electrically active impurity layer adjacent to the quantum dot layer had not effect on spectral diffusion.

Since our excitation (whether a single blue photon or two near-IR photons) energy is below that of the GaN bandgap of 3.4 eV, the lack of influence of Si doping on spectral diffusion makes physical sense. Carriers are excited into and confined in both the quantum dots and the quantum well layer, but not the Si doped adjacent layer, thus no trapping can take place.

It should be highlighted that for spectral diffusion over time-scales of seconds, the dependence solely on dislocations is a result which goes further in elucidating spectral diffusion than previous studies in either InGaN [54], GaN[139] or InGaAs [135] quantum dots.

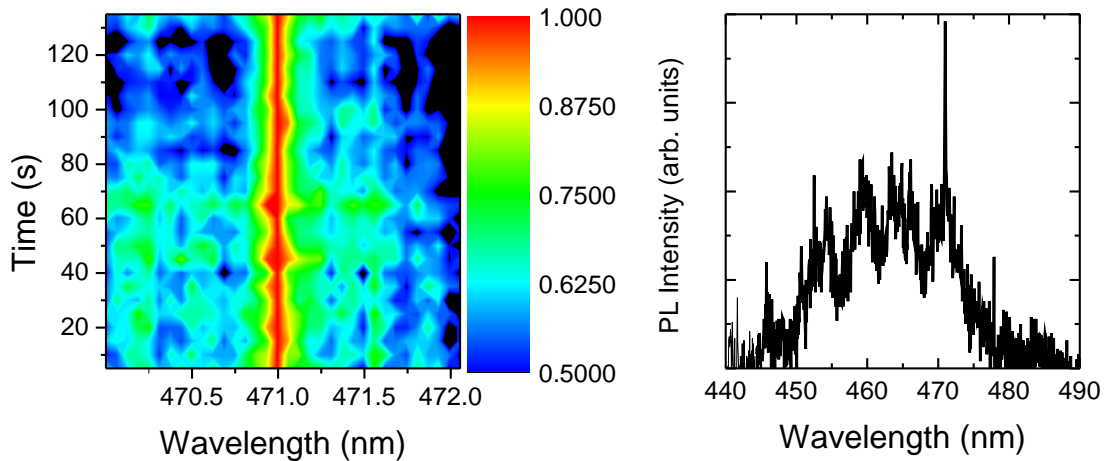


Figure 5.9: Left: Time evolution of a single quantum dot from the sample with Si doping $\sim 5 \times 10^{17} \text{ cm}^{-3}$ over a period of 130s. Normalised PL intensity is shown in colour. The behaviour of the quantum dot energy with time is very similar to that from quantum dots in the LDD undoped sample although the ratio of QD:QW luminescence is diminished in comparison with other undoped samples. Right: Time integrated PL spectra of the studied quantum dot with an accumulation time of 1 s.

5.5 Energy-linewidth relationship in spectral diffusion

Recall equation 2.6, which gave the expected quantum confined Stark shift ΔE expected for an internal field of magnitude F . In the previous section I have proposed that energy shifts of $0.25 - 0.4 \text{ meV}$ observed in the quantum dot emission can be explained by charge carriers trapped at nearby dislocation sites. We have seen in section 5.4.2 that the trapping time-scales for dislocations are of the order seconds, agreeing with the time-scale for dislocation-induced temporal fluctuations. Consider now a modification to the quantum confined Stark shift ($\Delta E \rightarrow \Delta E + \delta E$) caused by a change in internal field ($F \rightarrow F + \delta F$). For simplicity, we take the field induced by the carrier to be a scale δF which can be positive (reinforcing the internal field), or negative (acting against the internal field). Any trapped carrier will produce a radial field and so a component of this field will always act either against or with the internal field enabling us to use a simple scalar picture. Making the substitutions $\Delta E \rightarrow \Delta E + \delta E$ and $F \rightarrow F + \delta F$ in equation 2.6 we arrive at an equation for the modification of the Stark shift:

5.5. ENERGY-LINEWIDTH RELATIONSHIP IN SPECTRAL DIFFUSION

$$\delta E = \mu\delta F - \alpha\delta F^2 - 2\alpha F\delta F, \quad (5.2)$$

where the internal dipole moment μ and the polarisability α are defined as in equation 2.6. Values for the dipole moment ($\mu = 9.68 \text{ e\AA}$) and the polarisability $\alpha = 36 \text{ meV/MVcm}^{-1}$, as well as a typical internal field in an $\text{In}_{0.2}\text{Ga}_{0.8}\text{N}$ quantum dot ($F = 1.4 \text{ MVcm}^{-1}$) have been previously calculated [140]. Inserting these values into equation 5.2 we can estimate the required field δF for a single electron to cause a change δE in the total Stark shift of a certain magnitude. A field $\delta F = 50 \text{ kVcm}^{-1}$ would cause an energy shift $\delta E = 0.13 \text{ meV}$, while a field $\delta F = 100 \text{ kVcm}^{-1}$ would produce an energy shift $\delta E = 0.44 \text{ meV}$. Assuming a point charge field for an electron trapped at a dislocation this would mean the dislocation trap would need to be at least as close as 50 nm from the QD in the first case, and 35 nm in the second.

Using the numbers for dislocation densities measured in the LDD, MDD and HDD samples we can extract a typical length scale for distance between two dislocations of $\sim 140 \text{ nm}$, $\sim 400 \text{ nm}$, and $\sim 575 \text{ nm}$ for the HDD, MDD and LDD samples respectively. Assuming a random distribution of both dislocations and quantum dots, we could expect a typical QD-dislocation distance of half of those numbers, so 70 nm for HDD, 200 nm for MDD, and $\sim 290 \text{ nm}$ for the LDD sample. Our observation of large shifts in the QD luminescence only in the HDD sample is therefore plausible, as the typical QD-dislocation distance in this sample is much closer to our estimates of QD-charge distance required to induce shifts of 100s of μeV . The fact that some energy shifts are present in all the samples can be attributed to carriers trapped at quantum-well potential fluctuations. However, given we have seen that quantum dot density increases with dislocation density, it is possible that threading dislocations play a role in the quantum dot formation such that quantum dots will be formed closer to dislocation sites than would be expected randomly. It should also be pointed out that the dislocation density estimates here are performed by SEM and AFM as explained in [132]. While transmission electron microscopy (TEM) can provide a reliable method to identify all dislocation types, it's possible that the SEM/AFM method underestimates the dislocation density.

5.6. SPECTRAL DIFFUSION IN *A*-PLANE INGAN QUANTUM DOTS

Since the numbers estimated from equation 5.2 suggest that single electrons trapped at single dislocation sites are a plausible explanation for slow time-scale spectral diffusion, we can expect a relationship to exist between the quantum dot emission energy and its linewidth. If an electron trapped at a nearby dislocation provides an electric field which reinforces the internal field in the quantum dot, the quantum confined Stark effect will become stronger, causing a red shift of the emission line. If a trapped electron provides an electric field which acts against the internal field in the quantum dot, then the reduction in the quantum confined Stark effect should be accompanied by a blue shift in the emission line. Since both of these instances increase the field inhomogeneity in the quantum dot (due to the random direction of the electron field), we can expect these shifts to be accompanied by a broadening of the emission line [141]. We would therefore expect a correlation between the linewidth and quantum dot energy to be observed in a quantum dot exhibiting spectral diffusion, with a negative (positive) correlation indicating that the trapped charge field acts against (reinforces) the internal field in the quantum dot.

We show examples of such correlations in figure 5.10. Both positive and negative correlations have been observed in quantum dots exhibiting spectral diffusion. In figure 5.10, we see two examples. The first, taken from a quantum dot in the LDD sample shows a positive correlation between quantum dot energy and linewidth. The existence of positive correlations like this reinforces the earlier point that a charge carrier whose field acts against the internal field can still induce a broadening in the emission line. The second, taken from a quantum dot in the HDD sample shows no obvious overall correlation. However, separating the points into different time regions shows that correlations can exist for certain periods of time, for example the clear negative correlation present between 0s and 100s. The fact that this correlation is hidden when taking into account the data over the entire time frame suggests that there may be several dislocation sites and/or traps formed by quantum well potential fluctuations in the neighbourhood of the quantum dot.

5.6 Spectral diffusion in *a*-plane InGaN quantum dots

Figure 5.11 shows standard deviations for several quantum dots in both ELOG-grown and non ELOG-grown *a*-plane samples. An average standard deviation of $87 \mu\text{eV}$ (ELOG) and

5.6. SPECTRAL DIFFUSION IN *A*-PLANE INGAN QUANTUM DOTS

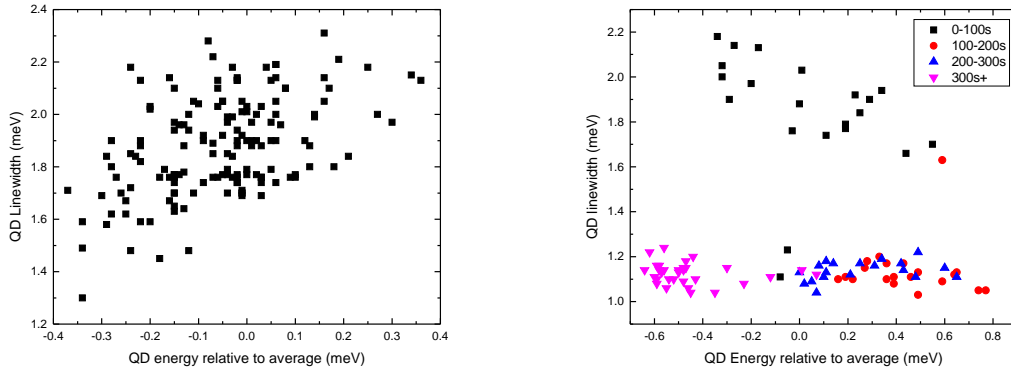


Figure 5.10: Left: Example of a positive correlation between quantum dot linewidth and energy taken from a quantum dot in the LDD sample. Right: Example of linewidth-energy relationship for a quantum dot in the HDD sample: Several competing processes seem to be at play, with varying correlations observable at different times.

88 μeV (non-ELOG) show a very low magnitude of spectral diffusion is typical in *a*-plane InGaN QDs. The correlation between QD linewidth and magnitude of spectral diffusion shown in figure 5.11 is similar to the case for the LDD and MDD *c*-plane quantum dot samples, suggest QW fluctuations and/or itinerant carriers in the QW are the dominant mechanism for spectral diffusion for the *a*-plane InGaN QDs as grown.

5.6.1 Lower bound for internal field in *a*-plane InGaN quantum dots

We have seen in chapter 4 that the *a*-plane InGaN quantum dots studied showed a significantly reduced exciton lifetime, indicating a reduction in the internal electric field present in the QDs. We have also seen in section 2.2.2 that the expected internal piezoelectric field in an *a*-plane quantum well should be zero, since no polarisation discontinuity exists along the *c*-direction. In the case of a quantum dot, there will exist side facets at some angle to the *c*-plane, meaning a polarisation discontinuity along the *c*-direction is possible, and thus the field will not necessarily be zero. We can make a crude test of the field size by considering the quantum confined stark shift $\delta E_{F=0}$ expected for a point charge field when no field exists in the quantum dot:

$$\delta E = \mu\delta F - \alpha\delta F^2. \quad (5.3)$$

5.6. SPECTRAL DIFFUSION IN *A*-PLANE INGAN QUANTUM DOTS

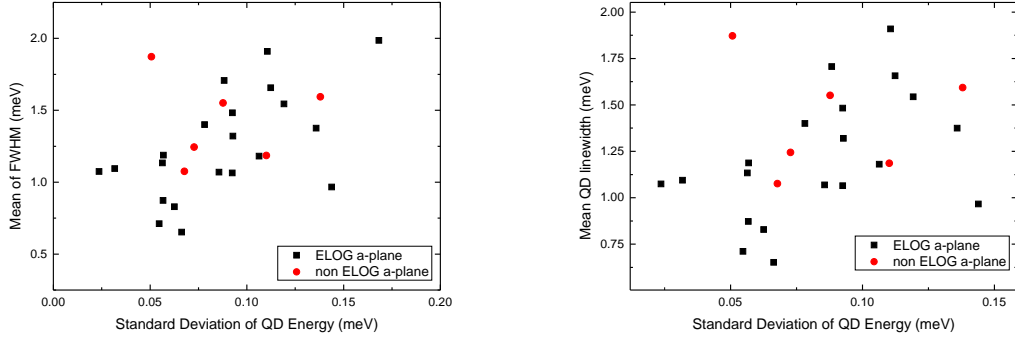


Figure 5.11: Left: Standard deviation of quantum dot energies plotted against emission energy for several *a*-plane quantum dots. As for the *c*-plane quantum dots, there is no observable correlation. Right: Standard deviation of quantum dot energies plotted against linewidth for several *a*-plane quantum dots. A positive correlation between linewidth and standard deviation can be seen.

Since the values of the vertical components of the permanent dipole μ and the polarisability α calculated in [140] for the *c*-plane case are not applicable here, we can turn to lateral field measurements on InGaN quantum dots [63] to estimate the components of the permanent dipole and polarisability which may exist in an *a*-plane quantum dot. While this may not be a very accurate approach, the values of μ and α calculated for both vertical and lateral directions for *c*-plane quantum dots predict that the values of the second term in equation 5.3 will be much larger than the first. We can conclude therefore that a point charge field will only ever induce a red-shift in the quantum dot emission for the case of zero-field. Looking back at equation 5.2, we can see that the third term $-2\alpha F\delta F$ can be negative in the case of F and δF being in the same direction, and positive in the opposite case, meaning both blue and red shifts of the quantum dot emission can be induced by a point charge. The condition for a blue shift to be observed is therefore that the $-2\alpha F\delta F$ term (which can be positive in the case of a point charge field acting against the internal field) outweighs the $-\alpha\delta F^2$ term (which is always negative). A blue shift induced by a point charge field can result in a positive correlation between energy and linewidth as seen in figure 5.12. Therefore, a necessary condition to observe such a positive correlation is:

$$-\alpha|\delta F|^2 + 2\alpha|F||\delta F| > 0, \quad (5.4)$$

5.6. SPECTRAL DIFFUSION IN *A*-PLANE INGAN QUANTUM DOTS

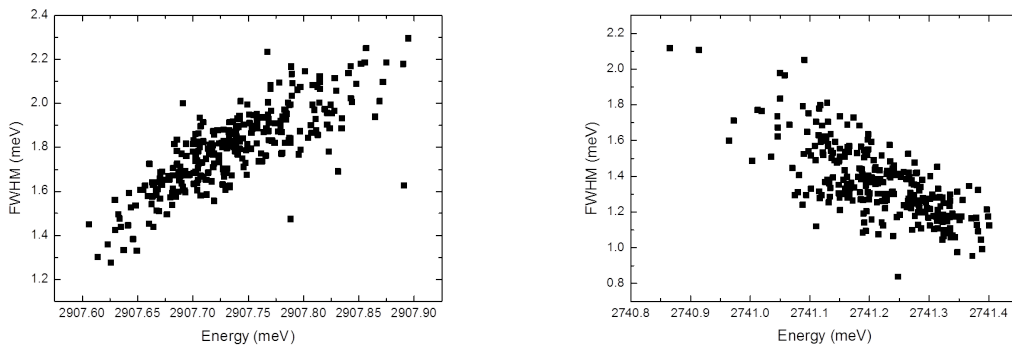


Figure 5.12: Left: Example of a positive correlation between quantum dot linewidth and energy taken from an *a*-plane quantum dot. Right: Example of a negative correlation between linewidth and energy for an *a*-plane quantum dot.

which simplifies to $|F| > \frac{1}{2}|\delta F|$. In figure 5.12 we can see examples of both positive and negative correlations between quantum dot energy and linewidth, meaning the internal field in the *a*-plane quantum dots is non-zero, and the condition $|F| > \frac{1}{2}|\delta F|$ applies. The measured average values for the standard deviation of quantum dot energy of $\sim 87 \mu\text{eV}$ suggest small fluctuations in the quantum confined Stark shift consistent with the scenario presented in section 5.5 of a point charge field of magnitude $\sim 50 \text{ kVcm}^{-1}$. The observed positive and negative correlations in figure 5.12 thus suggest a lower bound for the internal field in an *a*-plane quantum dot as $\sim 25 \text{ kVcm}^{-1}$. It should be noted that the lateral component of the polarisability has been measured to be ~ 40 times larger [63] than the vertical component in *c*-plane InGaN QDs, meaning a smaller point charge field could also induce the same shifts as seen in the spectral diffusion - which would also scale down our estimate of the lower bound for the internal field in *a*-plane InGaN QDs. I suggest these estimated values of the lower bound for the internal field in *a*-plane InGaN QDs must be close to the real value of the field given the order of magnitude reduction in lifetime from a *c*-plane InGaN quantum dot seen in chapter 4 - which indicate a field much smaller than the $\sim 1.4 \text{ MVcm}^{-1}$ typical calculated value for a *c*-plane InGaN quantum dot.

5.7 Effect of an external field on spectral diffusion

With both dislocations and fluctuations in the quantum well potential acting as traps for charge carriers, it is possible that applying an external field to an InGaN quantum dot could discharge the traps and help combat spectral diffusion. Application of external field has been shown to result in spectral tuning of the quantum dot luminescence energy [48] - such an effect combined with a decrease in the magnitude of spectral diffusion would significantly ease the challenge of achieving a spectral resonance between a quantum dot and a microcavity for quantum cavity electrodynamics. Here, initial results on the effect of the external field on the quantum dot linewidth are presented. Further work, in particular repeat spectra over a period of several minutes is required, but has not been achieved so far due to problems with shorting of p-i-n devices.

5.7.1 Sample growth

A p-i-n sample was grown at the University of Cambridge by Dr. Tongtong Zhu. A 10 period $\text{In}_{0.05}\text{Ga}_{0.95}\text{N}/\text{In}_{0.07}\text{Ga}_{0.93}$ superlattice (which could selectively etched to form mushroom shape optical microcavities) was grown on an n-type (Si doped) pseudosubstrate. This was followed by the growth of a 30 nm n-GaN layer. The doping level of the pseudosubstrate was chosen such that an electron density $\sim 2 \times 10^{18} \text{ cm}^{-3}$ is expected in the n-type layers. On top of the 30 nm n-GaN layer, a 20 nm unintentionally doped $\text{Al}_{0.3}\text{Ga}_{0.7}\text{N}$ electron blocking layer was grown, followed by 10 nm of unintentionally doped GaN. A *c*-plane InGaN quantum dot layer was grown on the unintentionally doped GaN via modified droplet epitaxy, and capped with 30 nm unintentionally doped GaN and finally a 30 nm Mg-doped p-GaN layer with an expected hole density $1 \times 10^{17} \text{ cm}^{-3}$.

5.7.2 Sample fabrication

Mesas were etched in order to reach the n-type GaN layer. “N-contacts” were formed by deposition of Ti/Au on the part of the surface of n-type GaN layer revealed by the etching procedure. “P-contacts” were formed by deposited Ti/Au contacts on an area of the sample adjacent to the mesa, on top of a SiN/SiO₂ layer to ensure electrical isolation of

5.7. EFFECT OF AN EXTERNAL FIELD ON SPECTRAL DIFFUSION

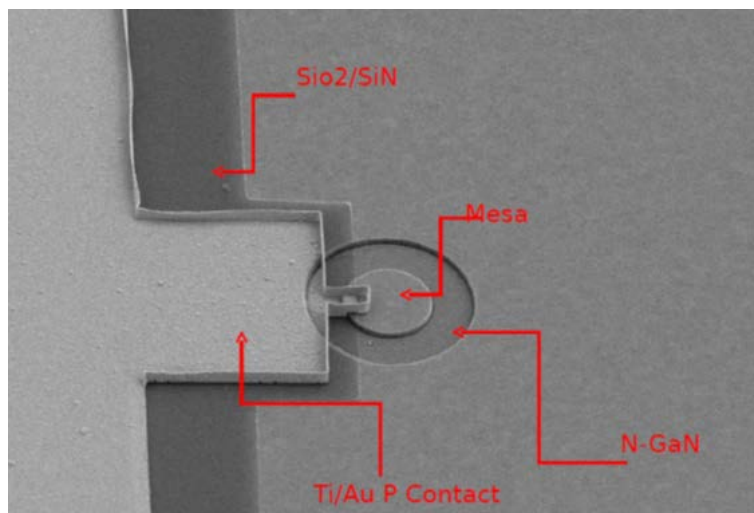


Figure 5.13: SEM image showing a Ti/Au P-contact of a p-i-n mesa. An insulating SiO₂/SiN layer is used to ensure electrical isolation of the P-contact from the non-mesa parts of the sample.

the “P-contact” from the rest of the sample. This is illustrated by an SEM image in figure 5.14. The fabrication of the mesas and contacts was done at the University of Harvard by Alex Woolf, Dr. Kasey Russell and Christine Zgrabik.

The contact pads were wire bonded and a specially modified cryostat used to connect the pads to a voltage source enabling application of bias at 4 K.

5.7.3 Spectral tuning and narrowing of linewidth of QD luminescence

Figure 5.14 shows successful partial compensation of the internal electric field in a single *c*-plane InGaN quantum dot by application of an external electric field. A blue shift of ~ 36 meV is observed due to the reduction in the quantum confined Stark effect. A narrowing of the linewidth of the quantum dot transition with applied reverse bias is shown for two separate quantum dots under reverse bias. This linewidth narrowing suggests reduced spectral diffusion on a time-scale much less than that of the accumulation time (here 1 s). It also lends credence to the explanation of fast time-scale spectral diffusion originating from carriers trapped at local potential maxima in the quantum well as it would appear an applied external field can discharge these traps. Given the observed correlation between linewidth and spectral diffusion over longer time-scales for samples with dislocation densities $< 10^9$ cm⁻², this narrowing of the transition linewidth could also

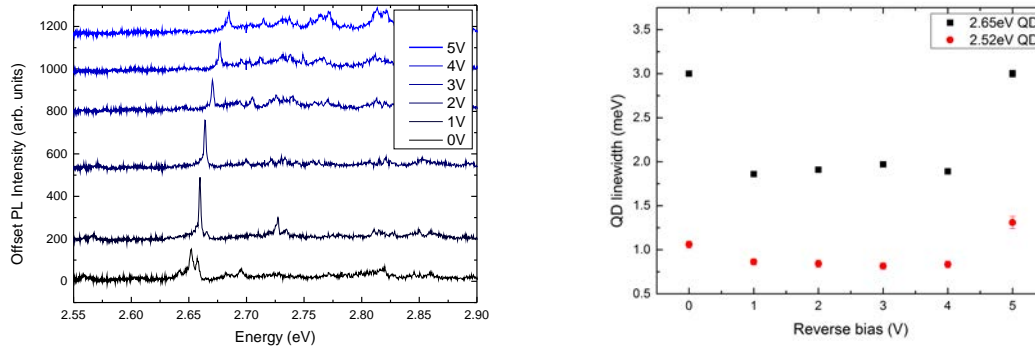


Figure 5.14: Left: Luminescence from a single InGaN quantum dot under reverse bias. As the bias voltage is increased, the internal electric field in the c -plane InGaN quantum dot is partially compensated for by the external electric field, resulting in a blue shift of ~ 36 meV in the quantum dot luminescence. At bias voltages up to 4 V, the quantum dot linewidth narrows when compared to the linewidth at a bias of 0 V, suggesting a reduction in spectral diffusion over time-scales faster than the integration time. Right: Linewidths for two quantum dots under reverse bias. Application of a reverse bias clearer reduces the linewidth. At a reverse bias of 5 V, the linewidth increases again.

represent a decrease in long time-scale spectral diffusion, although further investigation into the time-evolution of quantum dot emission line under applied bias is required. The observed minima in the quantum dot linewidth could be close to the resolution limit of the system in for both studied quantum dots as an increased slit width was used as the luminescence from this particular quantum dot sample was fairly dim.

5.8 Chapter summary

The origins of spectral diffusion in InGaN quantum dot luminescence have been investigated. Spectral diffusion is seen to occur over two distinct time-scales. Spectral diffusion over the slower of these time-scales, \sim seconds, is attributed to individual charge carriers trapped at threading dislocation sites in the neighbourhood of single InGaN quantum dots. Spectral diffusion over time-scales much faster than 1 s is attributed to charge carriers trapped at local potential maxima in the quantum well layer formed by indium fluctuations. This fast time-scale spectral diffusion can be reduced by applying an external electric field vertically against the built-in field in a c -plane InGaN quantum dot. Spectral

diffusion studies on *a*-plane quantum dots reveal these structures still exhibit an internal electric field, albeit reduced. The existence of this small internal field for *a*-plane InGaN quantum dots can be seen as an advantage, as spectral tuning techniques such as that demonstrated above for *c*-plane quantum dots could be possible still for *a*-plane InGaN quantum dots.

6

A coherent control scheme for excitons in a -plane InGaN QDs

A key requirement for the successful implementation of quantum information processing is the coherent control of qubits. Single qubit states need to be dynamically prepared, manipulated and detected. In conventional semiconductor-based computation, “bits” are incoherently controlled by external electric or optical fields. In the quantum case, the single qubit state has both an amplitude and a phase, and any control field needs to be able to navigate the Hilbert space of the quantum system whilst leaving in tact the quantum superposition. In this chapter, I present a coherent control scheme based on the excited exciton p -state $|1\rangle$ and the crystal ground state (no exciton) $|0\rangle$.

Coherent control has been shown by many different methods, such as nuclear magnetic resonance [142], electron-spin resonance in semiconductor quantum dots [143], and based on quantum dot excitons [144]. Figure 6.1 shows a simplified energy level diagram which illustrates the an excited state-exciton to crystal ground state coherent control scheme. A two photon picosecond pulse as described in section 3.3.1 excites the crystal ground state $|0\rangle$ (no exciton) to the excited state $|1\rangle$. This ($n = 2$)-state decays via a non-radiative relaxation to the s -state (exciton ground state) which radiatively recombines. The intensity of the emitted PL from the s -state recombination can be used to infer the population in the ($n = 2$)-state. Successful coherent control of the ($n = 2$)-state would be signified by *Rabi oscillations* between the ($n = 2$)-state and the ground state which

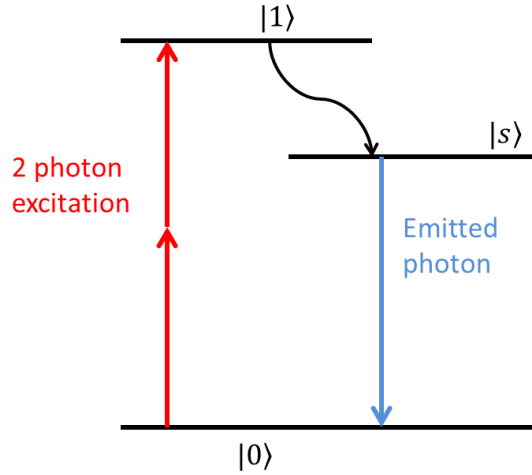


Figure 6.1: Simplified energy level diagram for a quantum dot showing a p-state to crystal ground state coherent control scheme. Coherent excitation into the excited state $|1\rangle$ drives a Rabi oscillation between this state and the crystal ground state $|0\rangle$ which can be observed as a power-dependent oscillation in the population of the $|s\rangle$ state which is observed by looking at the PL emitted in the radiative decay of this state.

manifest themselves as a period oscillation in the exciton ground-state PL intensity with increasing excitation power. The origin of these Rabi oscillations for the simple case of one photon excitation will be described in the next section.

6.1 Rabi Rotations

An ideal qubit is based on a two-level system. The system state described by a superposition $|\psi\rangle = \alpha|0\rangle + \beta|1\rangle$ of the two eigenstates of the system $|0\rangle$ and $|1\rangle$. The Hamiltonian for sure a system can be described by:

$$\hat{H} = \hbar\omega_1|1\rangle\langle 1|, \quad (6.1)$$

where ω_1 is the transition energy from state $|0\rangle$ to state $|1\rangle$. Rabi oscillations are a semi-classical effect that occur when such a system is subject to an optical field, causing a perturbation to the Hamiltonian H_{int} given by:

$$H_{\text{int}} = \mu E(t)|0\rangle\langle 1| + \mu E^*(t)|1\rangle\langle 0|, \quad (6.2)$$

where in the case of a quantum dot μ is the electric dipole of the transition $|0\rangle \rightarrow |1\rangle$, and $E(t)$ is the electric field amplitude of a driving field with frequency ω . Since a two-level system is a pseudospin, it is useful to write the full Hamiltonian in terms of the Pauli spin matrices $\hat{\sigma}_j$ which are given by:

$$\hat{\sigma}_j = \begin{pmatrix} \delta_{j,3} & \delta_{j,1} - i\delta_{j,2} \\ \delta_{j,1} + i\delta_{j,2} & -\delta_{j,3} \end{pmatrix}, \quad (6.3)$$

where $\delta_{i,j}$ is the Kronecker delta. The full Hamiltonian \hat{H}_{tot} for the 2 level system interacting with an external optical field is then expressed as:

$$\hat{H}_{\text{tot}} = \hbar\omega_1\hat{\sigma}_3 + \hbar\Omega_R\hat{\sigma}_1. \quad (6.4)$$

For a large number of photons in the optical field the effect of the quantum correlations between the Pauli spin operators (that they satisfy the commutation relations $[\hat{\sigma}_1, \hat{\sigma}_2] = 2i\hat{\sigma}_3$) becomes washed out and a good representation of the state of the system is the Bloch vector \vec{s} composed of the expectation values of the Pauli spin operators such that $\vec{s} = (\langle\hat{\sigma}_1\rangle, \langle\hat{\sigma}_2\rangle, \langle\hat{\sigma}_3\rangle)$. From Ehrenfest's theorem we obtain a set of differential equations governing the time evolution of the state \vec{s} :

$$\frac{d}{dt}\vec{s}(t) = \vec{\Omega}^F \times \vec{s}(t), \quad (6.5)$$

where we imagine the pseudospin \vec{s} acted on by a torque and the pseudospin rotates around the vector $\vec{\Omega}^F = (\mu E(t), 0, \omega_1)$. Defining a third Hamiltonian $\hat{H}_1 = \hbar\omega\hat{\sigma}_3$ where ω is the frequency of the optical field, we can make a unitary transformation $H_c = \exp(\frac{i\hat{H}_1 t}{\hbar})(\hat{H}_{\text{tot}} - \hat{H}_1) \exp(\frac{-i\hat{H}_1 t}{\hbar})$ to the rotating frame of the laser. In this frame we can make the ‘‘rotating wave approximation’’ [145] which neglects terms oscillating at twice the frequency of the optical field. It should be noted that this is equivalent to neglecting the simultaneous absorption of two photons from the laser field when one photon is at resonance with the exciton transition. Whilst in our case we use two photon absorption, similar reasoning

still applies as the two photon absorption becomes the resonant term in the equations 6.5 and terms oscillating at other frequencies can be neglected.

At this point we can introduce the Rabi energy $\hbar\Omega_R = 2\mu\epsilon(t)$. We can go further for the case of a -plane InGaN QDs and treat Ω_R , the Rabi frequency as a real number since for a linearly polarised quantum dot state the transition is spin-conserving and the phases of states $|0\rangle$ and $|1\rangle$ can be set so that Ω_R is real without loss of generality. After application of the rotating wave approximation the total Hamiltonian, which we will term the control Hamiltonian \hat{H}_c becomes:

$$\hat{H}_c = \frac{1}{2}\hbar\Omega_R\hat{\sigma}_1 + \frac{1}{2}\hbar\Delta\hat{\sigma}_z, \quad (6.6)$$

where $\Delta = \omega_1 - \omega$ represents the detuning of the laser from the optical transition $|0\rangle \rightarrow |1\rangle$. Equation 6.5 now reduces to:

$$\frac{d}{dt}s_1(t) = \Delta s_2 - \Gamma_2 s_1, \quad (6.7)$$

$$\frac{d}{dt}s_2(t) = -\Delta s_1 - \Gamma_2 s_2 + \Omega_R s_3, \quad (6.8)$$

$$\frac{d}{dt}s_3(t) = -\Gamma_1(s_3 + 1) - \Omega_R s_2, \quad (6.9)$$

where we have included Γ_1 as the radiative recombination decay rate for state $|1\rangle$ and Γ_2 as the dephasing rate of the state $|\psi\rangle$ due to phonon scattering and other environmental effects. These equations are termed the *optical Bloch equations*. The state vector \vec{s} can be represented as a point of the *Bloch sphere*, depicted in figure 6.2.

The z -axis of the Bloch sphere represents the population inversion between the states $|0\rangle$ and $|1\rangle$ while the x - and y -axes represent the population inversions between the states $\frac{1}{\sqrt{2}}(|0\rangle \pm |1\rangle)$ and $\frac{1}{\sqrt{2}}(|0\rangle \pm i|1\rangle)$ respectively. The relative phase between the two states $|0\rangle$ and $|1\rangle$ is given by the azimuthal angle ϕ which in the case of a linear polarised transition can be chosen to be zero.

In the perfect case of a laser on resonance and no decay of the states $\Gamma_1 = \Gamma_2 = 0$, the optical Bloch equations reduce to:

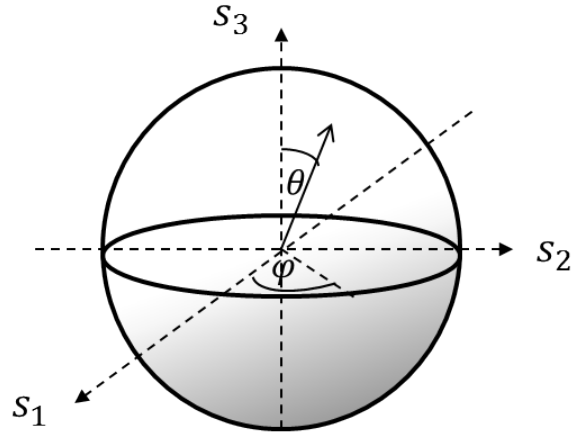


Figure 6.2: The Bloch sphere. The state of a two level system can be represented by the Bloch vector \vec{s} composed of the expectation values of the Pauli spin operators. The s_3 component represents the coherence - it is a measure of the population of the states $|0\rangle$ and $|1\rangle$, while the s_1 and s_2 axes represent the real and imaginary parts of the optical dipole.

$$\frac{d}{dt}s_1(t) = 0 \quad (6.10)$$

$$\frac{d}{dt}s_2(t) = \Omega_R s_3 \quad (6.11)$$

$$\frac{d}{dt}s_3(t) = -\Omega_R s_2. \quad (6.12)$$

The solutions to the above are easily calculated and for the case of a linear polarised transition $\phi = 0$ they are:

$$s_1(t) = \text{constant} \quad (6.13)$$

$$s_2(t) = s_3(0) \sin(\theta(t)) + s_2(0) \cos(\theta(t)) \quad (6.14)$$

$$s_3(t) = -s_2(0) \sin(\theta(t)) + s_3(0) \cos(\theta(t)), \quad (6.15)$$

where θ is a measure of the laser pulse area defined by:

$$\theta(t) = \frac{1}{\hbar} \int_0^t \mu E(t') dt'. \quad (6.16)$$

From the equations 6.15 we can see that a pulse area $\theta(t) = \pi$ results in an inversion of the state vector on the Bloch sphere, while a pulse area $\theta(t) = 2\pi$ returns the Bloch

vector back to its initial position. These results are the well-known Rabi oscillations which occur between the states $|0\rangle$ and $|1\rangle$ of a two-level system under a driving optical field $E(t)$. We term them Rabi rotations to make clear that not only the population inversion between $|0\rangle$ and $|1\rangle$ is changing, but rotations can happen about all axes of the Bloch sphere. Translating back into a Dirac-state picture, a qubit in initial state $|0\rangle$ will exhibit a post-pulse population of the state $|1\rangle$ which varies as $\sin^2(\frac{\theta}{2})$. A “ π -pulse” so named for a laser pulse area $\theta(t) = \pi$ is equivalent to a controlled NOT (CNOT) quantum gate. Observation of these oscillations between $|0\rangle$ and $|1\rangle$ would present a clear sign of successful manipulation of a qubit state.

Measurement of Rabi rotations on quantum dots in the III-Arsenides are common [146, 147, 148, 149, 150, 151], but to date there are no reports of successful Rabi rotations on InGaN quantum dots. The potential for room temperature operation of devices in the III-Nitrides [51, 52] provide a strong motivation to attempt the observation of Rabi rotations in the Nitrides. For InGaN specifically, the blue emission corresponds to the best commercially available single photon detectors providing another motivation to study this system in particular.

As described in section 2.4 of this thesis, the electric field intensity $|E(t)|^2$ varies linearly with power for a one photon excitation process, and as the square of the power for a two photon process. Since the pulse area $\theta(t)$ depends on the electric field amplitude $E(t)$ it should therefore depend on the square root of the excitation power for a one photon excitation, and linearly on the power for a two photon excitation. In the case of two photon excitation of InGaN quantum dots, we can therefore look for a Rabi oscillation that is periodic in the excitation power, so a particular power should correspond to a “ π -pulse” and twice that power should correspond to a “ 2π -pulse”. Such a scheme has been successfully adopted to measure Rabi oscillations between the excited exciton ($n = 2$)-state and the crystal ground state by several groups working on III-As quantum dots [152, 153, 154, 155, 156, 157]. In the III-As systems, this approach has fallen out of favour since the energetic separation between the p -state and wetting layer continuum states is small [158] leading to a hybridization of the wetting layer continuum states and the quantum dot excited states which acts as a source of dephasing for the oscillation. In

contrast, as will be described in section 6.2 the ($n = 2$)-state to quantum well continuum separation in a -plane InGaN quantum dots seems to be relatively large.

6.2 Photoluminescence Excitation spectroscopy on a -plane InGaN quantum dots

Before any attempt at coherent control can be made, a mapping out of the energy levels of a quantum dot is essential. The observation of a -plane InGaN quantum dot population at wavelengths as low as 420nm, as well as an observed higher brightness due to the increased oscillator strength outlined in chapter 4, meant this mapping was easily performed using two-photon excitation. Determination of the excited state positions is achieved by photoluminescence excitation spectroscopy, as described in section 3.5.2.

Using an a -plane InGaN QD sample masked as described in section 3.5.1, a suitable aperture was chosen to perform PLE studies. A μ -PL spectrum from the chosen aperture is shown in figure 6.3.

The aperture was selected to attempt to isolate a single bright quantum dot. In fact, three QD-like emission lines are present centred at 433.98 nm, 436.97 nm and 437.98 nm respectively. The splittings between these lines would be consistent with the A, B and C exciton splittings in an InGaN quantum well - (~ 6 meV for A-B, and ~ 25 meV for A-C, c.f 6 meV A-B and 43 meV A-C for GaN [71] and 3 meV A-B and 17 meV A-C for InN [159]). These splittings, coupled with results from the PLE discussed below identify these 3 lines as excitons formed from s -like electrons inherited from the conduction band, and p -like holes inherited from the A, B, and C valence bands. While these state may not straight forwardly correspond to A, B, and C excitons as in the bulk c -plane case, I will henceforth refer to these as A, B and C excitons for ease of labelling.

Figure 6.4 shows a high resolution PLE measurement performed on the QD studied for coherent control. There are 3 quantum dot lines (A, B and C) in the emission, the intensity of which is dependent on the excitation energy. Here, we use the second harmonic of the Ti:Sapphire laser as a convenient guide to the total excitation energy (wavelength) of the two excitation photons. A broad peak in the PLE intensity is seen at around ~ 400 nm due

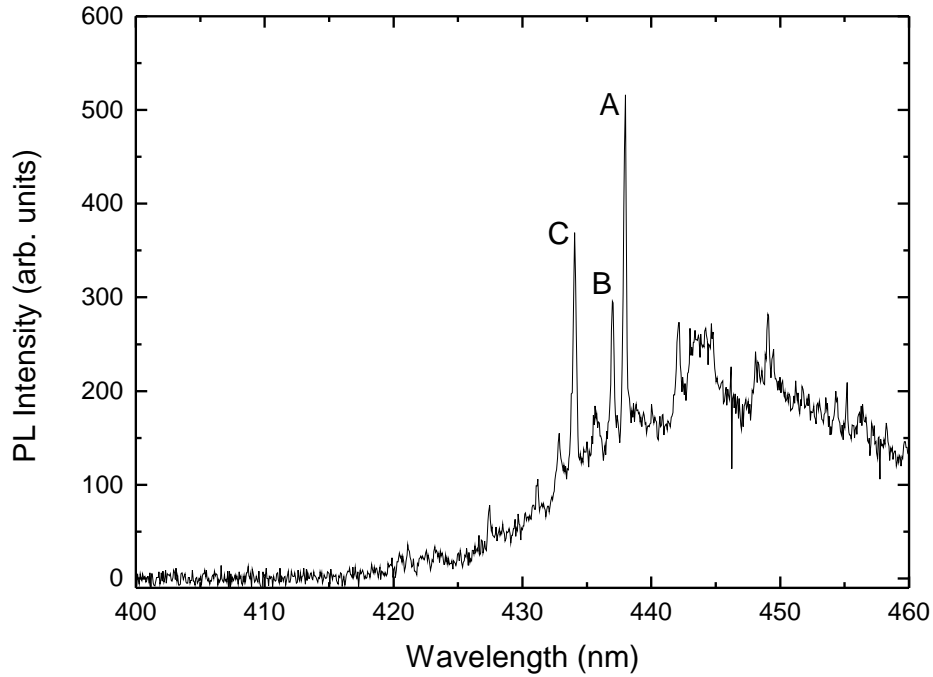


Figure 6.3: PL spectrum taken in aperture selected for PLE measurement. Three quantum dot emissions can be seen at $\sim 434\text{nm}$, $\sim 437\text{nm}$ and $\sim 438\text{nm}$. The splittings between each state would be consistent with excitons formed from the 1st electron state and the hole states equivalent to the A (438nm), B(437nm), and C(434nm) valence bands in the bulk case.

to the absorption into quantum well continuum states. We can see there is a corresponding emission from the quantum well in the PL spectra. There exist several resonances in the PLE intensity at energies lower than the broad band due to the continuum states, these are attributed to excited states. To focus in on these resonances, I have plotted the variation with excitation energy of the three quantum dot lines visible at $\sim 438\text{ nm}$ (A), $\sim 437\text{ nm}$ (B) and $\sim 434\text{ nm}$ (C) in figure 6.5.

The PLE spectra for the three quantum dot lines show good agreement - all three share a similar pattern of continuum states at around $\sim 400\text{ nm}$ and the same excited state resonances are visible for each of the three lines. The first few electron energy levels have been labelled according to the electron energy level (s, p etc. in analogy with atomic physics) and the hole character (A, B, C in analogy with the bulk valence band structure). Both the A (437.98 nm) and B (436.97 nm) excitons share a common resonance when the

laser second harmonic wavelength matches the C-exciton peak (434.05 nm). For this reason we attribute this resonance to the $((n = 1),C)$ energy level with a splitting of ~ 25 meV from the A-exciton that sits between the published bulk crystal field splittings for GaN (42 meV) and InN (17 meV) as would be expected for an InGaN quantum dot. The next three resonances in the PLE are labelled as the $((n = 2),A)$, $((n = 2),B)$, and $((n = 2),C)$ energy levels of the quantum dot - with similar splittings to those observed for the $(n = 1)$ -level. The next two resonances at 418.93 nm and 417.41 nm could reasonably be attributed to $(n = 3)$ energy levels. The higher energy resonances observed (412.77 nm, 411.19 nm, 410.30 nm, 406.42 nm, 404.58 nm, and 402.93 nm) are all clearly above the continuum state absorption (which tails off between 400 nm and 415 nm) but their proximity to the continuum states would suggest a probable hybridization of QD states with continuum states [158] which would not only detract from the possibility of these resonances showing Rabi oscillations [160], but also complicate the situation beyond the reach of the simple labelling system used thus far in identifying the states. It should be noted that while the PLE intensity at lower energies between the resonances is low, it is not zero and so continuum state absorption can still take place at these energies.

The PLE data show many possible excited state resonances which would be suitable candidates for a coherent control scheme. A successful coherent control not only requires a resonant excitation into a single quantum dot transition, (and therefore precise matching of the absorption to the excitation wavelength) but also that the total interaction time is shorter than the coherence time of the system. Given the lifetimes of 200 – 500 ps observed in chapter 4, and the typical relaxation timescale of just a few ps [79], I assume many of the resonances would meet the timescale criteria. The selection of candidate transitions is then best guided by energetic proximity to other observed transitions, and to the quantum well continuum states.

6.3 Observation of Rabi Oscillations

With high resolution PLE spectra performed on the chosen quantum dot, it was possible to attempt to observe Rabi oscillations between an excited state and the crystal ground state via observing changes photoluminescence intensity of the $((n = 1),A)$ state with changes

6.3. OBSERVATION OF RABI OSCILLATIONS

in the excitation power. Since our experimental setup can be subject to vibration-induced stage drift, a method to distinguish any Rabi oscillations in the PL intensity from those induce by a slight drift away from the quantum dot was required. Firstly, since the sample in question was masked with $\sim 1 \mu\text{m}$ apertures, i.e. the same size as the full width at half-maximum of the spatial profile of the laser (see section ??), any drift in the laser spot position relative to the sample will affect the excitation power density provided by the laser - i.e the effective excitation power will be reduced if the spot only partially overlaps with the aperture. Therefore, we can expect that any sample drift will affect both the quantum dot and quantum well luminescence (albeit to a smaller extent). Previous studies on the magnitude of the drift in our setup suggest a positional change in the laser spot of up to 2 nm per minute [161]. In my own studies I have observed a periodic drift of the laser spot over a period of ~ 10 minutes, with ~ 5 minutes a typical timescale over which the measured PL intensity from a quantum dot can be expected to be stable. Bearing this in mind, the second harmonic of the laser was used to determine the pulse area ($\propto \theta$) as the laser excitation power was varied using a neutral density filter. With this method, each power dependent series of spectra took under 1 minute to complete, (the exact time depending on the number of spectra taken, each with a 1 s accumulation time). Using this method we can be sure that no significant positional drift of the laser spot takes place.

In order to put into context later results, a power-dependent series of spectra where the PL intensity of the A exciton at 437.98 nm is tracked when excited off-resonantly in the quantum well continuum states are presented in figure 6.6. While we expect the QD intensity to increase as the square of the excitation power for two-photon excitation, as per section 2.4, since the laser second harmonic is also a two photon process we should expect a linear correlation between the second harmonic pulse area and the quantum dot intensity. The waterfall plot in figure 6.6 shows this expected behaviour complete with a saturation of the quantum dot intensity at high powers since the number of exciton recombinations per second is limited by the oscillator strength of the transition. In order to investigate this behaviour more closely, the intensity of the A-exciton line was calculated by fitting the relevant wavelength regions of the observed spectra to a Lorentzian, while a Lorentzian fit of the laser second harmonic was used to determine the pulse area. The results of

6.3. OBSERVATION OF RABI OSCILLATIONS

these fits are presented in figure 6.6 and show more clearly the expected behaviour of a linear intensity increase followed by a saturation of the intensity at higher powers. Note that this saturation does not occur for the quantum well luminescence since the quantum well can accommodate many excitons at once. The bright quantum well luminescence at higher powers increases the fit errors for the quantum dot intensity as it becomes more difficult to distinguish the quantum dot luminescence from the underlying quantum well luminescence.

To investigate the possibility of observing Rabi oscillations, I obtained power dependent series of spectra for several resonances observed in the PLE. In figure 6.7 I present results for excitation into the resonance at ~ 424 nm in the PLE, which I have assigned to the $((n = 2), C)$ level. That this resonance is both narrow and sufficiently energetically separated from both the quantum well continuum states and other PLE resonances suggests it would be the best chance to observe Rabi oscillations. The results are presented in figure 6.7.

The emitted PL intensity of the $((n = 1), A)$ shows a clear rise, fall then rise again - the signature of Rabi oscillations. At high excitation powers, the bright quantum well luminescence obscures the picture somewhat. However, the linear increase of quantum well luminescence intensity with the second harmonic pulse area is a confirmation that the results cannot be put down to stage drift. It should be noted also that a periodic stage drift over a time-scale of ~ 40 seconds (i.e. of a kind never observed in our setup) would be required to produce a rise, fall and then rise again of the quantum dot intensity.

As for the off-resonant case, a more useful representation of the relationship between second harmonic pulse area and quantum dot intensity can be obtained though fitting quantum dot and second harmonic spectra to Lorentzian lineshapes. The results (shown beneath the waterfall plot) show a clear Rabi oscillation in the $((n = 1), A)$ exciton intensity up to a pulse area of 4π . The first oscillation ($0 \rightarrow 2\pi$) indicates a population transfer of $\sim 56\%$ by application of a π pulse. This is certainly a promising result, and offers possibilities such as triggering a single photon source using a π pulse [162] already explored for III-As based quantum dot systems. A second oscillation ($2\pi \rightarrow 4\pi$) can also be seen, with a slightly longer period in the pulse area when compared to the first oscillation. This phenomenon of

an extended second oscillation has been reported previously for GaAs quantum dots [163]. Both the non-zero ($\sim 44\%$) excited state population observed after a 2π -pulse and the extension of the second Rabi oscillation are due to dephasing induced by the deviations of this system from a perfect two level system. Possible sources of dephasing are discussed further in the next section.

6.4 Decoherence and the damping of exciton Rabi oscillations

Since the studied a -plane InGaN quantum dots are a solid-state system, any carriers confined within a quantum dot will always be influenced by the environment of the QD, as we have seen via spectral diffusion in chapter 5. As well as spectral diffusion, crystal lattice vibrations, the effect of valence band mixing as well as continuum state mixing [158] would all be expected to be sources of decoherence for a quantum dot. From the perspective of quantum information, the coherence time must be long enough to perform sufficient logical operations to correct for any errors. This means the ratio between the coherence time and the slowest gate time, which represents the number of possible operations [164] should be maximised. At low temperature, we can immediately give an upper limit to the coherence time of the radiative recombination lifetime [165] of the quantum dot, so ~ 300 ps in our case. The successful observation of Rabi rotations gives a lower limit to the coherence time of the laser interaction time of 1 ps.

For the exciton Rabi rotations we have observed, one possible source of decoherence would be the simultaneous excitation of biexciton states during by the resonant laser pulse [166]. This is unlikely to affect the observed Rabi rotations here though, since we have measured in chapter 4 a typical biexciton binding energy to be ~ 36 meV which compares favourably with our laser spectral resolution of 1.3 meV (see section 3.2.1). Coupling to the continuum states as observed in [158, 167, 168] (or alternatively incoherent population of the quantum dot via relaxation from continuum states) gives rise to an intensity damping proportional to the laser power for single photon excitation on an InAs quantum dot [169] and could well be a source of intensity damping in our observed Rabi oscillation. However, since

the observed resonance is quite well energetically removed from the continuum states observed in the PLE, this effect can be expected to be small. Another source of dephasing frequently cited in studies on III-As quantum dots is excitation of more than one state due to the small fine structure splittings observed for InAs QDs [170]. This is also unlikely to be a problem for *a*-plane InGaN quantum dots since the A-exciton transition has been observed to be $\sim 100\%$ linearly polarised (see chapter 4), so the symmetry of the quantum dot inherently selects just one transition.

The observed damping of the Rabi oscillation most likely originates from spectral diffusion - the averaging of temporal fluctuations in the optical dipole observed as damping in the Rabi rotations. While the ELOG-grown *a*-plane InGaN QD sample studied here contained regions with very low densities of threading dislocations, spectral diffusion mediated by either itinerant carriers in the quantum well, or local fluctuations in the quantum well piezoelectric potential acting as traps to charges would be expected to contribute to the observed damping of the Rabi oscillations. This is especially true at high excitation power [134] where the quantum well will be populated with more carriers and so spectral shifts in the $((n = 1), A)$ exciton energy would become more frequent. Another source of exciton dephasing is interaction with acoustic phonons, as demonstrated for $(n = 1)$ excitons in InAs quantum dots [171, 172]. Here, the significantly reduced internal field in *a*-plane InGaN quantum dots should reduce acoustic phonon-induced dephasing. We can expect this based on the temperature dependent results presented in chapter 4, and theoretical studies performed on GaN quantum dots showing piezoelectric coupling of phonons has a significant contribution to phonon-broadening [107].

The elongated period of the second Rabi oscillation ($2\pi \rightarrow 4\pi$) also has its origin in dephasing. In a high-driving field regime we would expect local heating of the sample to occur. The exciton can interact with crystal lattice vibrations via the deformation potential (the change in energy levels in the quantum dot induced by strain). Thus, any Rabi rotation will be accompanied by a modulation of the crystal via the deformation potential. It has been shown [173] that a high driving field gives rise to a phonon-induced renormalisation of the Rabi energy which is a phonon-analogy of the Lamb shift [174] in atomic physics. It could be expected that this phonon-induced renormalisation in the

Rabi energy might be accompanied by a slight red shift of the quantum dot emission due to temperature induced renormalisation of the band gap [175] but I observe no measurable shift that could be distinguish from a spectral diffusion induced shift of the quantum dot energy at higher pulse areas.

6.5 Chapter Summary

We have seen that quantum dots prove good candidates for coherent control schemes required for any realisation of quantum information processing. The signature of successful coherent control is the observation of Rabi rotations between two states $|0\rangle$ and $|1\rangle$. I performed photoluminescence excitation spectroscopy on a single InGaN quantum dot and identified several resonances attributed to excited states. A narrow resonance without close proximity to any other resonances or to the observed quantum well continuum states was selected to attempt a demonstration of coherent control between this excited state ($|1\rangle$) and the crystal ground state ($|0\rangle$) via observation of the μ -PL intensity of the quantum dot ground state $|s\rangle$. Rabi rotations were observed with a pulse area varying from 0 to 4π , between π and 2π a population transfer of $\sim 56\%$ was observed. I attribute the observed intensity damping of the Rabi rotations mainly to spectral diffusion induced by carriers in the quantum well. The second Rabi oscillation $2\pi \rightarrow 4\pi$ had a longer period than the first, indicating local sample heating due to the high excitation power density of the excitation laser pulse.

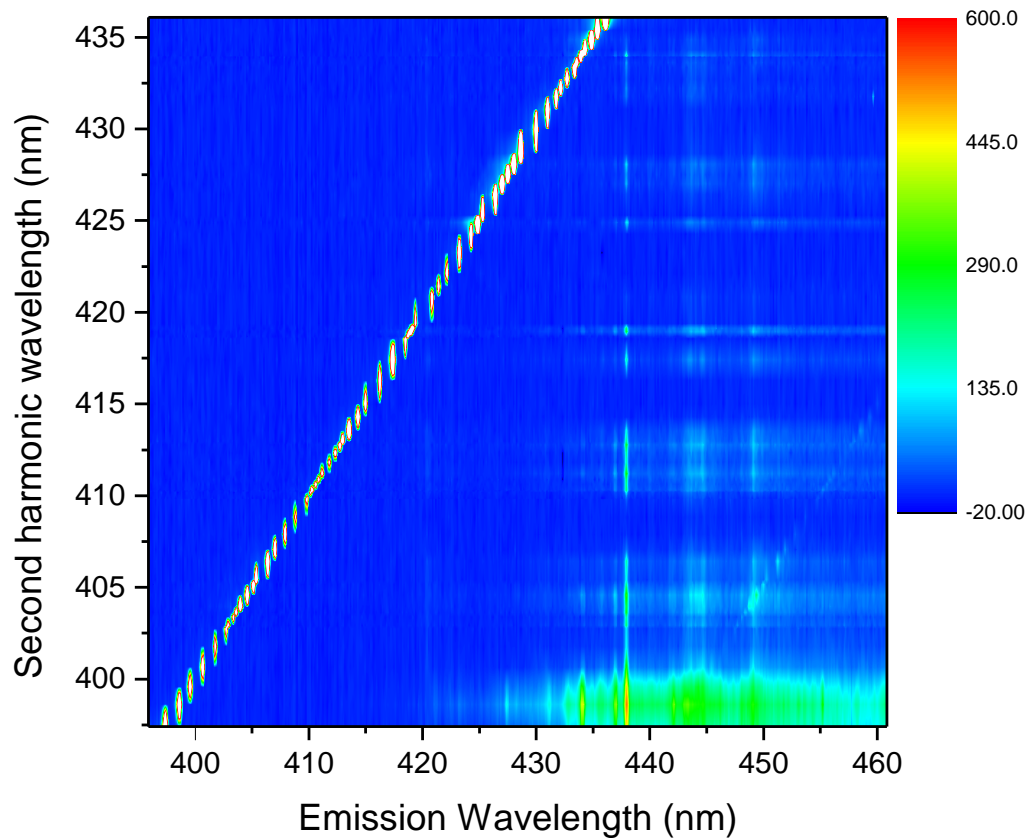


Figure 6.4: PLE spectra taken from *a*-plane InGaN quantum dot studied for coherent control. The second harmonic of the laser provides a convenient measure of the effective excitation energy (i.e. total energy of both excitation photons). There is a fairly broad PL spectrum due to the underlying quantum well layer with 3 clear quantum dot resonances at ~ 434 nm, ~ 437 nm and ~ 438 nm. The intensity is heavily dependent upon the excitation energy, a broad peak in the PLE can be seen around ~ 400 nm which corresponds to absorption into the quantum well continuum states. Other PLE resonances can be seen and are attributed to excited states.

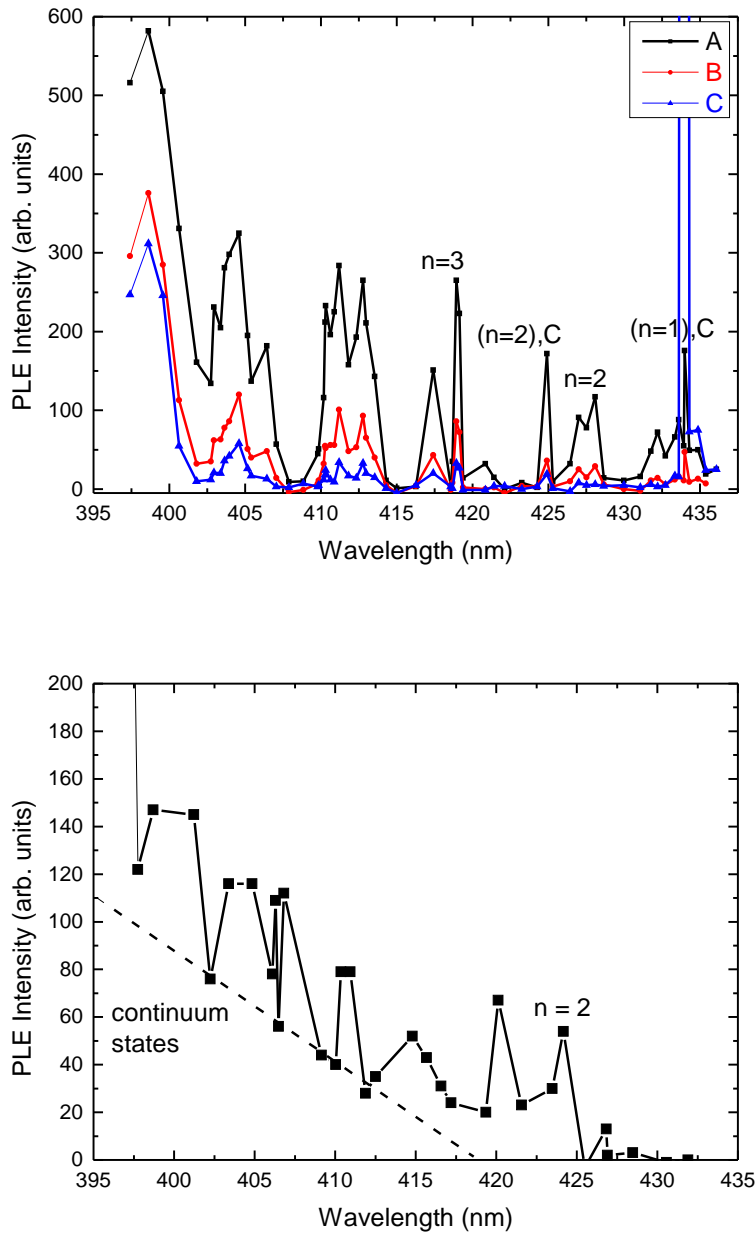


Figure 6.5: Top: PLE spectra of the three observed quantum dot lines in the selected aperture. The continuum state absorption can clearly be seen at 395 – 400 nm but by 415 nm this form of absorption has tailed off. The first few excited states of the quantum dot are labelled according to the electron energy level ($n = 1, n = 2, n = 3$, etc. named in analogy with atomic physics) and the associated hole character A, B (spin orbit splitting) and C (crystal field splitting). Bottom: PLE spectrum of another quantum dot in a different aperture, emitting at 433.5 nm. The effect of the quantum well continuum states is clearly visible. The energies associated with the continuum states here appear to extend further towards the quantum dot energy than was the case for the quantum dot studied for coherent control. A similar pattern of lines are identified as the ($n = 2$) states, and any higher energy states strongly influenced by mixing with continuum states.

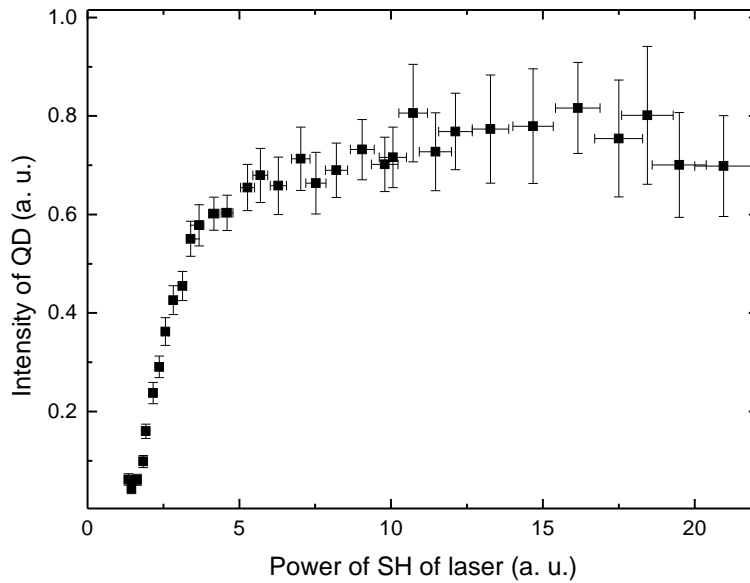
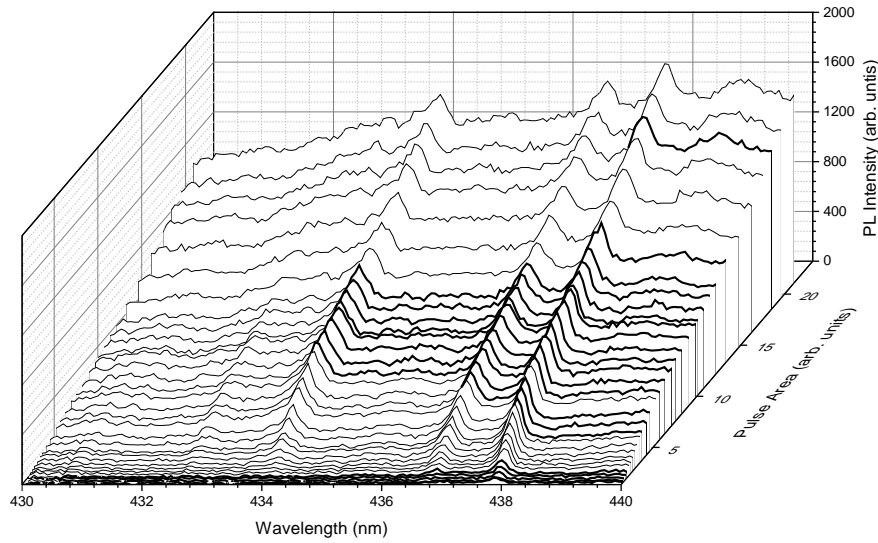


Figure 6.6: Top: Waterfall plot showing the PL intensity of the A, B and C exciton lines with increasing excitation power as measured by the pulse area of the laser second harmonic. The quantum dot emission intensity scales linearly with the second harmonic pulse area for all three lines until some saturation occurs at higher power. The background quantum well luminescence intensity increases linearly without any saturation. Bottom: The total A-exciton PL intensity plotted against the pulse area of the second harmonic. Both the A-exciton intensity and the second harmonic pulse area were determined by fitting the relevant spectra to Lorentzian lineshapes. The behaviour of a linear increase in PL intensity for the quantum dot followed by a saturation is confirmed more precisely using this method.

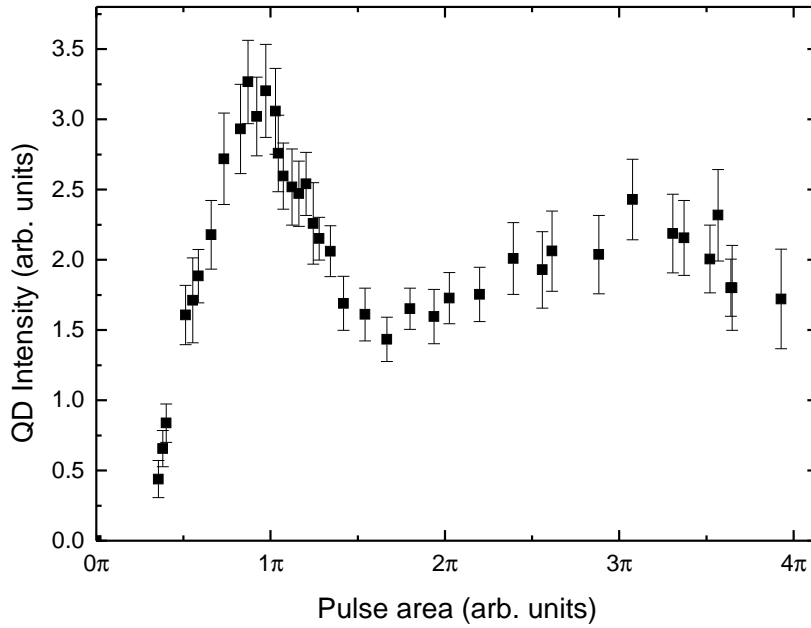
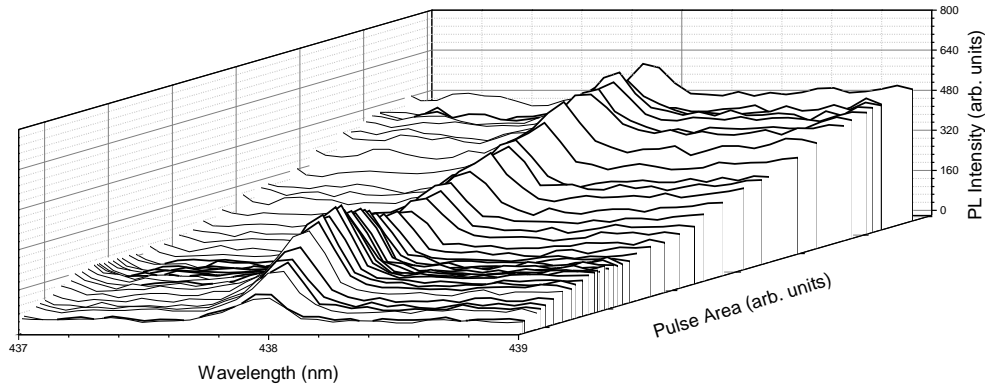


Figure 6.7: Top: Waterfall plot of $((n = 1), A)$ exciton PL as a function of second harmonic pulse area when excited at the $((n = 2), C)$ PLE resonance at ~ 424 nm. The QD intensity clearly rises then dips before rising again - the behaviour expected for a two-level system undergoing Rabi rotations. Bottom: When Lorentzian fits are performed to determine the second harmonic pulse area and the $((n = 1), A)$ exciton intensity, we can see a clear indication of Rabi oscillations up to a pulse area of 4π . The second ($2\pi \rightarrow 4\pi$) oscillations appears extended compared with the first ($0 \rightarrow 2\pi$).

7

Conclusion

Experimental studies of the optical properties of InGaN/GaN quantum dots have been undertaken. Time-integrated and time-resolved microphotoluminescence, photoluminescence excitation, and polarisation-resolved spectroscopy of single InGaN quantum dots provides information about their suitability for applications in both quantum cryptography and quantum computing.

InGaN/GaN quantum dots grown on the non-polar a -plane of the GaN crystal pseudo-substrate have been studied by microphotoluminescence under non-linear excitation by a pulsed laser. Time-integrated photoluminescence indicates the presence of narrow optical transitions associated with both biexcitons and excitons confirming the successful formation of quantum dots. Time-resolved studies reveal an order of magnitude increase in the oscillator strength of the exciton transition when compared to c -plane InGaN quantum dots, suggesting a significantly reduced internal electric field in non-polar InGaN quantum dots. The increased oscillator strength demonstrates potential for single photon source applications in the blue spectral region, as the time-jitter of emission would be significantly reduced in comparison to polar InGaN quantum dots.

Large surface pits formed during the growth of non-polar InGaN quantum dots exhibit a spatial correlation with quantum dot emission as measured by cathodoluminescence. This provides potential for accurate spatial localisation of an InGaN quantum dot, which is essential in order to achieve a spatial resonance with an optical microcavity.

Polarisation resolved spectroscopy of non-polar InGaN quantum dots reveals many quantum dot emission lines are 100% linearly polarised. Such emission could be used to experimentally demonstrate some proposed quantum cryptography schemes. For quantum dot emissions with a polarisation degree less than unity, a fine structure splitting between two orthogonal polarisation axes can be resolved in an optical setup with a simple top-down excitation geometry. This is due to strain along the in-plane c -direction causing an elongation in the quantum dot along this direction. The associated asymmetry in quantum dot shape ensures linearly polarised light is emitted with a polarisation axis corresponding to an in-plane crystal direction. Thus, top-down excitation is sufficient to resolve two orthogonal polarisations and reveal the fine structure splitting. This is in contrast to the c -plane case, where the polarisation axis for a particular quantum dot will not necessarily point in the plane as the asymmetry of the quantum dot is governed by the distribution of indium atoms in the dot.

A statistical investigation into the origins of spectral diffusion in polar InGaN quantum dots is presented, and spectral diffusion is seen to occur over two distinct timescales. Spectral diffusion on the slower of these timescales (\sim seconds) is attributed to a modification to the quantum confined Stark shift caused by charge carriers trapped at threading dislocation sites in the neighbourhood of individual quantum dots. Spectral diffusion on the faster timescale is attributed to both itinerant carriers in the underlying quantum well layer which forms during the growth procedure, and carriers trapped at local maxima in the quantum well potential due to fluctuations in the indium content. Electrically active impurities in a layer adjacent to the quantum dot layer are shown to have little to no effect on the spectral diffusion. The understanding of the origins of spectral diffusion, and the potential to reduce it's magnitude by discharging these carrier traps using a reverse bias applied across the intrinsic region of p-i-n structure containing InGaN quantum dots is an important step towards the control required to achieve spectral resonance between a quantum dot and an optical microcavity.

Spectral diffusion studies on a -plane InGaN quantum dots can be used to argue that the internal field, while reduced compared to that in the c -plane case, still remains non-zero and thus using a reverse biased p-i-n structure for spectral tuning and reduction

of spectral diffusion is a possibility for a -plane quantum dots as well. This potential to achieve a spectral resonance between cavity and emitter, coupled with the potential for spatial resonance by accurate spatial localisation of a -plane quantum dots, suggests that cavity quantum electrodynamics may be more easily achieved for a -plane InGaN quantum dots than for their c -plane counterparts.

An experimental demonstration of a coherent control scheme for an excited state exciton in an InGaN quantum dot has been presented. Rabi rotations between the excited exciton state and the crystal ground state are observed by monitoring the excited exciton state population using the decay of the exciton ground state. It is possible that the asymmetry of the quantum dot confinement potential due to the strain-induced elongation of the quantum dot increases the energy separation between excited states associated with different hole characters compared to the c -plane case, meaning narrow resonances that correspond to a single excited state can be probed. The observed high degree of linear polarisation could also be a factor in the successful demonstration of Rabi rotation, as the suppression of the emission of the fine structure split state further reinforces the two-level nature of the system. The observed Rabi oscillation exhibits significant dephasing which is attributed to both acoustic phonon coupling and spectral diffusion. Inclusion of the quantum dot in an optical microcavity could help to reduce this dephasing.

Bibliography

- [1] C. Kittel, *Quantum theory of Solids* (John Wiley, New York, 1963). 9
- [2] R. Dingle, W. Wiegmann, and C. H. Henry, *Phys. Rev. Lett.* **33**, 827 (1974). 9
- [3] D. Gershoni *et al.*, *Phys. Rev. Lett.* **65**, 1631 (1990). 9
- [4] A. S. Plaut *et al.*, *Phys. Rev. Lett.* **67**, 1642 (1991). 9
- [5] L. Birotheau *et al.*, *Applied Physics Letters* **61**, 3023 (1992). 9
- [6] J. Cibert *et al.*, *Applied Physics Letters* **49**, 1275 (1986). 9
- [7] C. Sikorski and U. Merkt, *Phys. Rev. Lett.* **62**, 2164 (1989). 9
- [8] K. Brunner *et al.*, *Phys. Rev. Lett.* **69**, 3216 (1992). 9
- [9] P. Michler *et al.*, *Science* **290**, 2282 (2000). 9
- [10] Z. Yuan *et al.*, *Science* **295**, 102 (2002). 9
- [11] V. Zwiller, T. Aichele, and O. Benson, *New Journal of Physics* **6**, 96 (2004). 9
- [12] B. Lounis and M. Orrit, *Reports on Progress in Physics* **68**, 1129 (2005). 9
- [13] M. Oxborrow and A. G. Sinclair, *Contemporary Physics* **46**, 173 (2005). 9
- [14] E. Knill, R. Laflamme, and G. J. Milburn, *Nature* **409**, 46 (2001), 10.1038/35051009.
9
- [15] M. Pelton *et al.*, *Phys. Rev. Lett.* **89**, 233602 (2002). 10
- [16] S. Laurent *et al.*, *Applied Physics Letters* **87**, 163107 (2005). 10

- [17] D. Englund *et al.*, Nature **450**, 857 (2007). 10
- [18] J. P. Reithmaier *et al.*, Nature **432**, 197 (2004), 10.1038/nature02969. 10
- [19] T. Yoshie *et al.*, Nature **432**, 200 (2004). 10
- [20] H. Walther, B. T. H. Varcoe, B.-G. Englert, and T. Becker, Reports on Progress in Physics **69**, 1325 (2006). 10
- [21] K. Hennessy *et al.*, Nature **445**, 896 (2007). 10
- [22] D. Englund *et al.*, Phys. Rev. Lett. **104**, 073904 (2010). 10
- [23] R. J. Thompson, G. Rempe, and H. J. Kimble, Phys. Rev. Lett. **68**, 1132 (1992). 10
- [24] A. Boca *et al.*, Phys. Rev. Lett. **93**, 233603 (2004). 10
- [25] P. Michler *et al.*, Applied Physics Letters **77**, 184 (2000). 10
- [26] L. Zhang and E. Hu, Applied Physics Letters **82**, 319 (2003). 10
- [27] S. Strauf *et al.*, Phys. Rev. Lett. **96**, 127404 (2006). 10
- [28] T. Jennewein *et al.*, Phys. Rev. Lett. **84**, 4729 (2000). 10, 48
- [29] N. Akopian *et al.*, Phys. Rev. Lett. **96**, 130501 (2006). 10
- [30] R. M. Stevenson *et al.*, Nature **439**, 179 (2006). 10
- [31] R. Hafenbrak *et al.*, New Journal of Physics **9**, 315 (2007). 10
- [32] A. Muller, W. Fang, J. Lawall, and G. S. Solomon, Phys. Rev. Lett. **103**, 217402 (2009). 10
- [33] C. L. Salter *et al.*, Nature **465**, 594 (2010). 10
- [34] A. Dousse *et al.*, Nature **466**, 217 (2010). 10
- [35] S. Nakamura, T. Mukai, and M. Senoh, Applied Physics Letters **64**, 1687 (1994). 10
- [36] S. Nakamura *et al.*, Japanese Journal of Applied Physics **35**, L74 (1996). 10
- [37] V. Y. Davydov *et al.*, physica status solidi (b) **229**, r1 (2002). 10

- [38] S. Z. Wang, S. F. Yoon, Y. X. Xia, and S. W. Xie, *Journal of Applied Physics* **95**, 7998 (2004). 10
- [39] R. S. Q. Fareed *et al.*, *Applied Physics Letters* **84**, 1892 (2004). 10
- [40] M. F. Wu *et al.*, *Journal of Vacuum Science & Technology A: Vacuum, Surfaces, and Films* **24**, 275 (2006). 10
- [41] H. P. Maruska and J. J. Tietjen, *Applied Physics Letters* **15**, 327 (1969). 10
- [42] J. Li *et al.*, *Applied Physics Letters* **83**, 5163 (2003). 10
- [43] Z. Z. Bandić, T. C. McGill, and Z. Ikonić, *Phys. Rev. B* **56**, 3564 (1997). 11
- [44] D. Gerthsen *et al.*, *Applied Physics Letters* **79**, 2552 (2001). 11
- [45] S. Amloy *et al.*, *Applied Physics Letters* **101**, 061910 (2012). 11, 45
- [46] R. A. Oliver *et al.*, *Applied Physics Letters* **83**, 755 (2003). 11, 25
- [47] A. F. Jarjour *et al.*, *Applied Physics Letters* **91**, 052101 (2007). 11, 53
- [48] A. F. Jarjour *et al.*, *Phys. Rev. Lett.* **99**, 197403 (2007). 11, 12, 13, 18, 19, 60, 76
- [49] S. De Rinaldis, I. D'Amico, and F. Rossi, *Phys. Rev. B* **69**, 235316 (2004). 11
- [50] T. Deguchi *et al.*, *Japanese Journal of Applied Physics* **38**, L914 (1999). 11
- [51] S. Kako *et al.*, *Nat Mater* **5**, 887 (2006). 11, 85
- [52] S. Deshpande, A. Das, and P. Bhattacharya, *Applied Physics Letters* **102**, 161114 (2013). 11, 53, 85
- [53] T. Zhu *et al.*, *Applied Physics Letters* **102**, 251905 (2013). 12, 41
- [54] J. H. Rice *et al.*, *Applied Physics Letters* **84**, 4110 (2004). 13, 57, 63, 69
- [55] C.-Y. Yeh, Z. W. Lu, S. Froyen, and A. Zunger, *Phys. Rev. B* **46**, 10086 (1992). 15
- [56] A. R. Denton and N. W. Ashcroft, *Phys. Rev. A* **43**, 3161 (1991). 16
- [57] V. Darakchieva, B. Monemar, and A. Usui, *Applied Physics Letters* **91**, 031911 (2007). 17

- [58] A. G. Bhuiyan, A. Hashimoto, and A. Yamamoto, *Journal of Applied Physics* **94**, 2779 (2003). 17
- [59] A. E. Romanov *et al.*, *Journal of Applied Physics* **100**, 023522 (2006). 17, 18
- [60] F. Bernardini, V. Fiorentini, and D. Vanderbilt, *Phys. Rev. B* **56**, R10024 (1997). 17, 18
- [61] D. P. Williams, A. D. Andreev, E. P. O'Reilly, and D. A. Faux, *Phys. Rev. B* **72**, 235318 (2005). 18, 21
- [62] I. A. Ostapenko *et al.*, *Applied Physics Letters* **97**, 063103 (2010). 19
- [63] J. W. Robinson *et al.*, *Applied Physics Letters* **86**, 213103 (2005). 19, 74, 75
- [64] K. Lee *et al.*, in *Numerical Simulation of Optoelectronic Devices, 2005. NUSOD '05.* (IEEE, Berlin, 2005), pp. 5–6. 19
- [65] S. Birner *et al.*, *Electron Devices, IEEE Transactions on* **54**, 2137 (2007). 19
- [66] K. Xing, Y. Gong, J. Bai, and T. Wang, *Applied Physics Letters* **99**, 181907 (2011). 21
- [67] F. Bernardini and V. Fiorentini, *Applied Physics Letters* **80**, 4145 (2002). 21
- [68] S. Muensit, E. M. Goldys, and I. L. Guy, *Applied Physics Letters* **75**, 3965 (1999). 21
- [69] G. Bu *et al.*, *Applied Physics Letters* **84**, 4611 (2004). 21
- [70] S. Schulz, A. Berube, and E. P. O'Reilly, *Phys. Rev. B* **79**, 081401 (2009). 21
- [71] G. D. Chen *et al.*, *Applied Physics Letters* **68**, 2784 (1996). 22, 86
- [72] S. Amloy *et al.*, *Phys. Rev. B* **83**, 201307 (2011). 23, 39, 44, 54
- [73] S. Amloy, K. F. Karlsson, T. G. Andersson, and P. O. Holtz, *Applied Physics Letters* **100**, 021901 (2012). 24, 53
- [74] Y. Arakawa, T. Someya, and K. Tachibana, *physica status solidi (b)* **224**, 1 (2001). 25

- [75] I. N. Stranski and L. Krastanow, Sitzungsberichte d. Akad. d. Wissenschaften in Wien, Abt IIb, Band **146**, 797 (1937). 25
- [76] A. F. Jarjour *et al.*, Physica E: Low-dimensional Systems and Nanostructures **32**, 119 (2006). 26, 35
- [77] R. A. Oliver *et al.*, Journal of Materials Science: Materials in Electronics **19**, 208 (2008). 27, 58
- [78] S. H. G. Pankove J. I., Bloom, RCA Rev. **36**, 163 (1975). 27
- [79] B. Ohnesorge *et al.*, Phys. Rev. B **54**, 11532 (1996). 28, 88
- [80] J. W. Robinson *et al.*, Applied Physics Letters **83**, 2674 (2003). 28
- [81] P. M. W. French, Reports on Progress in Physics **58**, 169 (1995). 29
- [82] M. Jansen *et al.*, Opt. Express **4**, 3 (1999). 29
- [83] D. E. Spence, P. N. Kean, and W. Sibbett, Opt. Lett. **16**, 42 (1991). 30
- [84] P. D. Maker, R. W. Terhune, and C. M. Savage, Phys. Rev. Lett. **12**, 507 (1964). 30
- [85] A. Major *et al.*, Opt. Lett. **29**, 602 (2004). 30
- [86] F. Brossard *et al.*, Opt. Express **21**, 16934 (2013). 34
- [87] C. J. Sansonetti, M. L. Salit, and J. Reader, Appl. Opt. **35**, 74 (1996). 34
- [88] R. J. Becker, MRS Proceedings **597**, (1999). 35
- [89] J. P. Moreno and M. G. Kuzyk, The Journal of Chemical Physics **123**, 194101 (2005). 35
- [90] G. L. Dakovski and J. Shan, Journal of Applied Physics **114**, 014301 (2013). 35
- [91] A. F. Jarjour *et al.*, physica status solidi (c) **2**, 3843 (2005). 35
- [92] D. Collins *et al.*, Nanotechnology **20**, 245702 (2009). 35
- [93] A. V. Fedorov, A. V. Baranov, and K. Inoue, Phys. Rev. B **54**, 8627 (1996). 39

- [94] K. I. Kang *et al.*, Phys. Rev. B **45**, 3465 (1992). 39
- [95] X. Yang, M. Arita, S. Kako, and Y. Arakawa, Applied Physics Letters **99**, 061914 (2011). 41
- [96] S. Founta *et al.*, Applied Physics Letters **86**, 171901 (2005). 41
- [97] M. Häberlen *et al.*, Journal of Applied Physics **108**, 033523 (2010). 42
- [98] S. Nakamura, Science **281**, 956 (1998). 42
- [99] C. Johnston *et al.*, Journal of Crystal Growth **311**, 3295 (2009). 42
- [100] L. Z.-Y. Liu *et al.*, Journal of Physics: Conference Series **209**, 012012 (2010). 42
- [101] R. Seguin *et al.*, Applied Physics Letters **84**, 4023 (2004). 44, 48
- [102] R. Bardoux *et al.*, Phys. Rev. B **79**, 155307 (2009). 45
- [103] K. Sebald, J. Kalden, H. Lohmeyer, and J. Gutowski, physica status solidi (b) **248**, 1777 (2011). 45
- [104] J. H. Rice *et al.*, Nanotechnology **16**, 1477 (2005). 45
- [105] M. Winkelkemper *et al.*, physica status solidi (b) **245**, 2766 (2008). 45
- [106] G. Bacher *et al.*, Phys. Rev. Lett. **83**, 4417 (1999). 45
- [107] I. A. Ostapenko *et al.*, Phys. Rev. B **85**, 081303 (2012). 48, 92
- [108] K. Sebald *et al.*, physica status solidi (b) **243**, 1661 (2006). 48
- [109] J. Kalden *et al.*, Nanotechnology **21**, 015204 (2010). 48
- [110] A. Muller, J. Breguet, and N. Gisin, EPL (Europhysics Letters) **23**, 383 (1993). 48
- [111] L. Schade *et al.*, physica status solidi (b) **248**, 638 (2011). 48
- [112] K. Domen, K. Horino, A. Kuramata, and T. Tanahashi, Applied Physics Letters **70**, 987 (1997). 52
- [113] H. Masui *et al.*, Journal of Physics D: Applied Physics **41**, 225104 (2008). 52

- [114] Ren-Chun *et al.*, Chinese Physics B **18**, 2603 (2009). 52
- [115] S. Ghosh *et al.*, Applied Physics Letters **80**, 413 (2002). 52
- [116] N. F. Gardner *et al.*, Applied Physics Letters **86**, 111101 (2005). 52
- [117] Q. Yan, P. Rinke, M. Scheffler, and C. G. V. de Walle, Applied Physics Letters **97**, 181102 (2010). 52
- [118] S. Schulz *et al.*, Phys. Rev. B **82**, 125318 (2010). 52
- [119] T. J. Badcock *et al.*, Journal of Applied Physics **105**, 123112 (2009). 52
- [120] C. Wu *et al.*, physica status solidi (c) **7**, 2073 (2010). 52
- [121] R. Bardoux *et al.*, Phys. Rev. B **77**, 235315 (2008). 53
- [122] R. H. Brown and R. Q. Twiss, Nature **177**, 27 (1956). 53
- [123] C.-W. Hsu *et al.*, Nano Letters **11**, 2415 (2011). 53
- [124] K. F. Karlsson *et al.*, Physica B: Condensed Matter **407**, 1553 (2012). 54
- [125] P. P. Paskov, T. Paskova, P. O. Holtz, and B. Monemar, Phys. Rev. B **64**, 115201 (2001). 54
- [126] B. Monemar *et al.*, physica status solidi (b) **245**, 1723 (2008). 54
- [127] T. Takagahara, Phys. Rev. B **47**, 4569 (1993). 54
- [128] J. Seufert *et al.*, Applied Physics Letters **76**, 1872 (2000). 57, 68
- [129] N. Panev *et al.*, Journal of Applied Physics **92**, 7086 (2002). 57
- [130] B. Pietka *et al.*, Phys. Rev. B **87**, 035310 (2013). 57
- [131] B. P. L. Reid *et al.*, Japanese Journal of Applied Physics **52**, 08JE01 (2013). 57
- [132] R. A. Oliver *et al.*, Journal of Crystal Growth **289**, 506 (2006). 58, 71
- [133] R. Datta *et al.*, Superlattices and Microstructures **36**, 393 (2004). 58
- [134] R. Bardoux *et al.*, Phys. Rev. B **74**, 195319 (2006). 60, 92

- [135] W. Bak *et al.*, Applied Physics Letters **100**, 022105 (2012). 60, 63, 69
- [136] T. Zhu *et al.*, Journal of Crystal Growth **338**, 262 (2012). 63, 68
- [137] I. Aharonovich *et al.*, Applied Physics Letters **103**, 021112 (2013). 63
- [138] C. Kammerer *et al.*, Applied Physics Letters **81**, 2737 (2002). 67
- [139] T. Bretagnon *et al.*, Phys. Rev. B **73**, 113304 (2006). 69
- [140] A. F. Jarjour *et al.*, Superlattices and Microstructures **43**, 431 (2008). 71, 74
- [141] D. A. B. Miller *et al.*, Phys. Rev. Lett. **53**, 2173 (1984). 72
- [142] D. Gammon *et al.*, Science **277**, 85 (1997). 80
- [143] K. C. Nowack, F. H. L. Koppens, Y. V. Nazarov, and L. M. K. Vandersypen, Science **318**, 1430 (2007). 80
- [144] N. H. Bonadeo *et al.*, Science **282**, 1473 (1998). 80
- [145] P. Kok and B. W. Lovett, *Introduction to Optical Quantum Information Processing* (Cambridge University Press, Cambridge, 2010). 82
- [146] T. Guenther *et al.*, Phys. Rev. Lett. **89**, 057401 (2002). 85
- [147] A. Zrenner *et al.*, Nature **418**, 612 (2002). 85
- [148] A. J. Ramsay *et al.*, Phys. Rev. B **75**, 113302 (2007). 85
- [149] A. J. Ramsay *et al.*, Phys. Rev. Lett. **100**, 197401 (2008). 85
- [150] H. Takagi *et al.*, Opt. Express **16**, 13949 (2008). 85
- [151] R. Melet *et al.*, Phys. Rev. B **78**, 073301 (2008). 85
- [152] Y. Toda, T. Sugimoto, M. Nishioka, and Y. Arakawa, Applied Physics Letters **76**, 3887 (2000). 85
- [153] H. Htoon *et al.*, Phys. Rev. B **63**, 241303 (2001). 85
- [154] H. Kamada *et al.*, Phys. Rev. Lett. **87**, 246401 (2001). 85

- [155] H. Htoon *et al.*, Phys. Rev. Lett. **88**, 087401 (2002). 85
- [156] L. Besombes, J. J. Baumberg, and J. Motohisa, Phys. Rev. Lett. **90**, 257402 (2003).
85
- [157] Q. Q. Wang *et al.*, Phys. Rev. Lett. **95**, 187404 (2005). 85
- [158] A. Vasanelli, R. Ferreira, and G. Bastard, Phys. Rev. Lett. **89**, 216804 (2002). 85,
88, 91
- [159] B. K. Meyer, in *New Data and Updates for I-VII, III-V, III-VI and IV-VI Compounds*, Vol. 44A of *Landolt-Brnstein - Group III Condensed Matter*, edited by U. Roessler (Springer, Berlin, 2009), Chap. 125, pp. 271–271. 86
- [160] Q. Q. Wang *et al.*, Phys. Rev. B **72**, 035306 (2005). 88
- [161] K. H. Lee *et al.*, Applied Physics Letters **88**, 193106 (2006). 89
- [162] P. Ester *et al.*, Applied Physics Letters **91**, 111110 (2007). 90
- [163] C. Wolpert *et al.*, physica status solidi (b) **249**, 721 (2012). 91
- [164] D. P. DiVincenzo, Science **270**, 255 (1995). 91
- [165] P. Borri *et al.*, Phys. Rev. Lett. **87**, 157401 (2001). 91
- [166] B. Patton, U. Woggon, and W. Langbein, Phys. Rev. Lett. **95**, 266401 (2005). 91
- [167] Q. Q. Wang *et al.*, Applied Physics Letters **87**, 031904 (2005). 91
- [168] H. J. Zhou *et al.*, Opt. Lett. **30**, 3213 (2005). 91
- [169] J. M. Villas-Bôas, S. E. Ulloa, and A. O. Govorov, Phys. Rev. Lett. **94**, 057404
(2005). 91
- [170] K. F. Karlsson *et al.*, Phys. Rev. B **81**, 161307 (2010). 92
- [171] J. Förstner, C. Weber, J. Danckwerts, and A. Knorr, Phys. Rev. Lett. **91**, 127401
(2003). 92
- [172] A. J. Ramsay *et al.*, Phys. Rev. Lett. **105**, 177402 (2010). 92

- [173] A. J. Ramsay *et al.*, Phys. Rev. Lett. **104**, 017402 (2010). 92
- [174] W. E. Lamb and R. C. Retherford, Phys. Rev. **72**, 241 (1947). 92
- [175] Z. Gavcević *et al.*, Journal of Applied Physics **109**, 103501 (2011). 93